Technical Physics Letters, Vol. 30, No. 4, 2004, pp. 259–261. Translated from Pis'ma v Zhurnal Tekhnicheskoĭ Fiziki, Vol. 30, No. 7, 2004, pp. 1–6.

Peculiarities of the Oxidation of Porous Silicon during Aqueous After-Etching

B. M. Kostishko*, S. V. Appolonov, S. Ya. Salomatin, and A. E. Kostishko

Ul'yanovsk State University, Ul'yanovsk, Russia

** e-mail: kost@sv.uven.ru*

Received August 25, 2003

Abstract—The process of oxidation of the surface of porous silicon in the course of aqueous after-etching has been studied by monitoring the change in the shape of the inverse self-convolution of a Si $L_{23}VV$ peak in the Auger electron spectrum. It was found that the formation of SiO_x in the surface layer of samples proceeds in several stages. In the first stage, silicon suboxides composed of SiO_nSi_{4-n} tetrahedra (n = 1–3) are formed on the surface of silicon quantum filaments. The formation of a SiO_2 phase stable with respect to external factors begins only upon 20-h aqueous after-etching and is completed within seven days. © *2004 MAIK "Nauka/Interperiodica".*

The process of oxidation of porous silicon (por-Si) has been extensively studied since 1956 [1], primarily because this material was employed as a high-ohmic insulator in the active elements of integrated circuits. Then, since Canham [2] discovered the photoluminescence of por-Si in the visible spectral range, oxidation of the surface of silicon quantum filaments was used as a means of creating radiative centers in por-Si and stabilizing its light-emitting properties [3]. The main experimental method employed for studying the oxidation kinetics is IR spectroscopy. However, a significant disadvantage of this technique is that it provides only data on the total oxygen content in the entire por-Si layer, which is usually evaluated using the IR absorption bands related to Si–O–Si (1100 cm^{-1}) and SiO_x (453 and 800 cm^{-1}) vibrations [4]. However, there are cases (e.g., rapid high-temperature oxidation [5] and oxidation in normal and heavy water [6] or in a chlorine-containing electrolyte [7]) when it is very important to obtain information not only about variation of the total amount of oxygen bonds but on the stoichiometry of silicon oxide as well.

It was recently demonstrated [8, 9] that the process of aqueous after-etching of por-Si is accompanied by electrochemical dissolution of silicon at the sharp pore apices, that is, in the region of boundaries between pores and single crystal silicon. Although both the thickness and stoichiometry of SiO_x films formed in the course of aqueous after-etching are important factors determining the optical and light-emitting properties of por-Si, no data on the kinetics and peculiarities of this process have been reported so far.

In this context, we have used Auger electron spectroscopy (AES) for studying changes in the electron structure of the surface layer of por-Si in the course of aqueous after-etching. Based on these data, we have determined peculiarities in the growth of SiO_x on the surface of silicon quantum filaments.

The experiments were performed with samples prepared from phosphorus-doped (111)-oriented single crystal silicon wafers with a resistivity of 32 Ω cm, in which a por-Si layer was formed using a standard procedure of electrochemical etching in a mixed HF–C_2H_5OH (1 : 1) electrolyte. The etching was carried out for 30 min at a current density of 20 mA/cm^2 under illumination with a halogen lamp. The thickness of the porous layer determined on cleaved samples was about 20 μm. The process of aqueous after-etching was studied in a large interval of times ranging from 10 min to 168 h, whereby the porous layer thickness increased up to 180–200 μm. Immediately after this treatment, the samples were placed into the analytical chamber of an Auger electron spectrometer (09IOS-10-005 type), and their surfaces were analyzed by AES at a residual pressure of $p = 10^{-7}$ Pa, a modulation voltage of U_m = 2 V, and $\nu\tau = 0.6$.

It should be noted that the total time of exposure of the por-Si samples to air did not exceed 10 min. This limitation was related to the rapid (with a characteristic time on the order of 30 min) leak of the positive charge localized at the pore apices, which resulted in termination of the aqueous after-etching process. In addition, experiments showed that the aqueous after-etching process is followed by quite rapid and effective additional oxidation of silicon quantum filaments in air, whereby the stoichiometric index of SiO_x can change from 0.7 to 2 within three days.

The change in the SiO_x stoichiometry in the porous layer in the course of aqueous after-etching was determined using a database on the variation of the inverse self-convolution of a Si $L_{23}VV$ peak in the Auger elec-

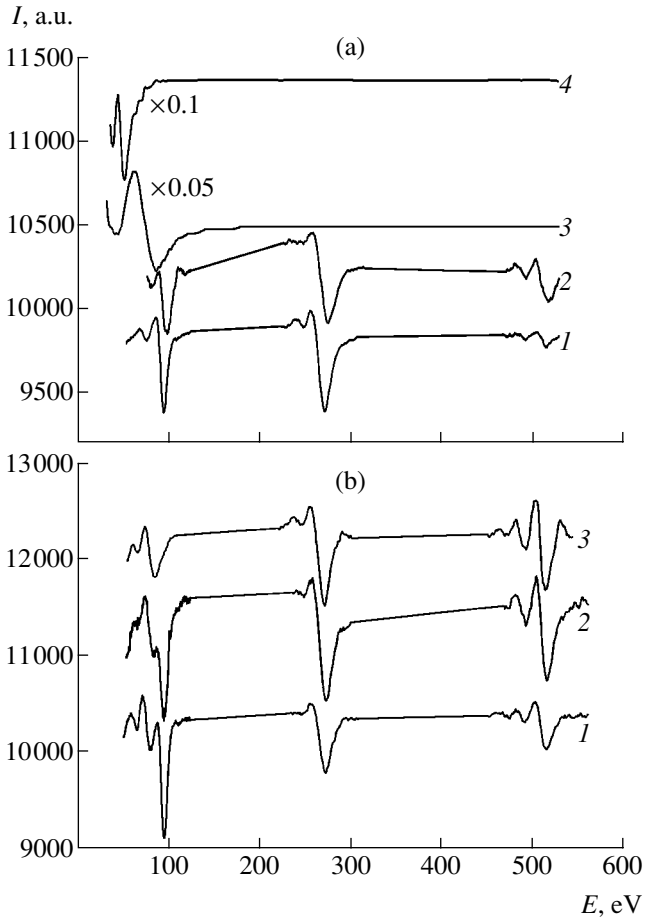

Fig. 1. Auger electron spectra of por-Si upon aqueous after-etching for various periods of time: (a) 10 min (*1*), 15 min (*2*), 30 min (*3*), 60 min (*4*); (b) 24 h (*1*), 72 h (*2*), 168 h (*3*).

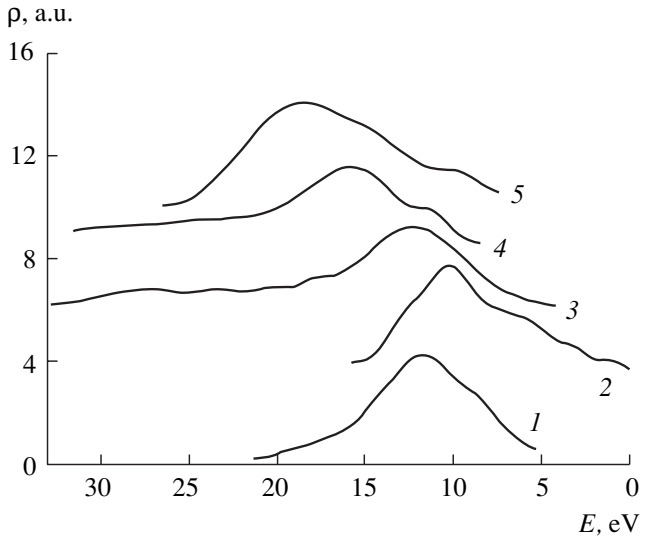

Fig. 2. Inverse self-convolution of the Si $L_{23}VV$ peak in the Auger electron spectrum of por-Si samples upon aqueous after-etching for various periods of time: (*1*) 10 min; (*2*) 15 min; (*3*) 24 h; (*4*) 72 h; and (*5*) 168 h.

tron spectrum. This method, described in detail elsewhere [10, 11], employs information on the electron structure (i.e., the position of the valence band top and the density of electron states on this level) in order to exclude the influence of adsorbed oxygen-containing species and determine the stoichiometric index of SiO_x with an error not exceeding ±0.05.

Figure 1 shows the Auger electron spectra of por-Si upon aqueous after-etching for various periods of time. An analysis of changes of the sample surface composition and the shape of the inverse self-convolution of the density of states (Fig. 2) leads to the following conclusions.

A short aqueous after-etching (10–15 min) leads to an increase in intensity of the AES signal of oxygen. Note that oxidized silicon is not detected (see spectra *1* and *2* in Fig. 1a) and, hence, the amount of oxygen increases due to adsorption and the growth of suboxides (unsaturated oxides) composed of SiO_nSi_{4-n} tetrahedra (n = 1–3). The peaks of the density of states related to $SiOSi_3$, SiO_2Si_2, and SiO_3Si virtually do not contribute to the Si $L_{23}VV$ peak [12]. After a 15-min treatment, the peak of elemental silicon shifts by 3 eV toward higher energies and the width of the ρ(E) spectrum increases (Fig. 2, curve *2*), which is explained by the accumulation of inhomogeneously distributed negative charge on the sample surface [13].

A 30-min aqueous after-etching makes the surface charging evident (see spectra *3* and *4* in Fig. 1a), since the Si $L_{23}VV$ line acquires a shape analogous to that observed for a por-Si surface upon thermal annealing in vacuum [14]. A shift of the AES peak of silicon to lower energies suggests that a 30- to 60-min aqueous after-etching leads to positive charging of the sample surface. As a rule, this phenomenon takes place due to the absence of charge transfer channels and the lack of compensation for the formation of doubly charged positive surface ions as a result of the Auger process.

The AES signal of oxidized silicon appears upon aqueous after-etching for a sufficiently long time. After a 24-h treatment, the stoichiometric index of silicon oxide is $x = 0.7 \pm 0.1$ (spectrum *1* in Fig. 1b; curve *3* in Fig. 2), and a 72-h after-etching increases this value to $x = 1.3 \pm 0.1$ (spectrum *2* in Fig. 1b; curve *4* in Fig. 2). A nearly stoichiometric silicon dioxide on the surface of silicon quantum filaments in por-Si is observed only after a 168-h treatment (spectrum *3* in Fig. 1b; curve *5* in Fig. 2).

Thus, we have established that the aqueous after-etching of por-Si proceeds through the adsorption of oxygen atoms and the formation of suboxides. For a period of time within 20 h, this process leads to the appearance of a high-ohmic surface layer effectively charged in the course of electron irradiation. As the after-etching time increases, a SiO_2 phase begins to form, but a nearly stoichiometric silicon dioxide on the surface of silicon quantum filaments appears only after a sufficiently long time (about seven days).

REFERENCES

1. A. Uhlir, Bell Syst. Tech. J. **35**, 333 (1956).
2. L. T. Canham, Appl. Phys. Lett. **57**, 1046 (1990).
3. Y. Xiao, M. J. Heben, J. M. McCullough, *et al.*, Appl. Phys. Lett. **62**, 1152 (1993).
4. E. A. Petrova, K. N. Bogoslovskaya, L. A. Balagurov, *et al.*, Mater. Sci. Eng., B **69–70**, 152 (2000).
5. H. Mimura, T. Futagi, T. Matsumoto, *et al.*, Jpn. J. Appl. Phys. **33**, 586 (1994).
6. D. N. Goryachev, G. Polisskiĭ, and O. M. Sreseli, Fiz. Tekh. Poluprovodn. (St. Petersburg) **32**, 1016 (1998) [Semiconductors **32**, 910 (1998)].
7. S. A. Gavrilov, A. I. Belogorokhov, and L. I. Belogorokhova, Fiz. Tekh. Poluprovodn. (St. Petersburg) **36**, 104 (2002) [Semiconductors **36**, 98 (2002)].
8. M. E. Kompan and I. Yu. Shabanov, Fiz. Tekh. Poluprovodn. (St. Petersburg) **29**, 1250 (1995) [Semiconductors **29**, 971 (1995)].
9. B. M. Kostishko and Yu. S. Nagornov, Zh. Tekh. Fiz. **71** (7), 60 (2001) [Tech. Phys. **46**, 847 (2001)].
10. B. M. Kostishko, S. V. Appolonov, A. E. Kostishko, *et al.*, Izv. Vyssh. Uchebn. Zaved., Mater. Élektron. Tekh., No. 1, 38 (2001).
11. B. M. Kostishko and S. V. Appolonov, in *Proceedings of the 2nd All-Russia Scientific–Engineering Computer-Aided Conference on Measurement Methods and Instruments, Nizhni Novgorod, 2000*, Part 1, p. 36.
12. S. S. Chao, J. E. Tyler, V. Takaji, *et al.*, J. Vac. Sci. Technol. A **4**, 1574 (1986).
13. *Electron and Ion Spectroscopy of Solids*, Ed. by L. Fiermans, J. Vennik, and W. Dekeyser (Plenum, New York, 1978; Mir, Moscow, 1981), pp. 256–257.
14. B. M. Kostishko, Yu. S. Nagornov, and S. V. Appolonov, Izv. Vyssh. Uchebn. Zaved., Élektronika, No. 4, 12 (2001).

Translated by P. Pozdeev

Technical Physics Letters, Vol. 30, No. 4, 2004, pp. 262–264. Translated from Pis'ma v Zhurnal Tekhnicheskoĭ Fiziki, Vol. 30, No. 7, 2004, pp. 7–13.

Effective Fiber-Optic Polarization Modulator

O. I. Kotov, A. V. Khlybov, S. I. Markov, and A. V. Kudryashov

St. Petersburg State Technical University, St. Petersburg, 195251 Russia

Received October 2, 2003

Abstract—A fiber-optic polarization modulator based on a piezoelectric ceramic transducer is considered. The device employs the phenomenon of photoelasticity, whereby the polarization of light in the fiber is modulated due to the birefringence variations induced by oscillating transverse pressure applied to the fiber. An analytical expression for the modulation efficiency is obtained. A high efficiency of the proposed modulator is confirmed by experimental data. © *2004 MAIK "Nauka/Interperiodica".*

Using piezoelectric ceramic oscillators, it is possible to create inexpensive and effective polarization modulators for the radiation propagating in a single-mode fiber. These devices employ the phenomenon of induced linear birefringence, which is usually described in terms of orthogonal linearly polarized modes. Such modulators can be used in *Q*-switched optical cavities, amplitude modulators, and polarimetric gauges [1, 2]. In many cases, it is required that a modulator change the phase difference between eigenmodes while keeping their amplitudes constant.

In the piezoelectric ceramic–optical fiber system, the electric voltage applied to the transducer electrodes can produce modulation of the phase difference between polarized modes both via a change in the fiber length and via the phenomenon of photoelasticity, whereby induced internal mechanical stresses lead to modulation of the fiber birefringence. The efficiency of fiber-optic polarization modulators based on piezoelectric ceramic oscillators can be characterized by the quantity

$$K = \frac{\delta\varphi}{\delta l L}[\text{rad}/(\mu\text{m m})], \quad (1)$$

where $\delta\varphi$ is the amplitude of the phase difference between polarized modes in the fiber, δl is the amplitude of oscillations of the ceramic transducer, and L is the fiber length in the modulator. Being virtually independent of the amplitude-frequency properties of the ceramic material, this efficiency characteristic is especially convenient for modulators of the type under consideration.

We have analyzed different variants of piezoelectric polarization modulators and selected the most effective design employing modulation of the induced birefringence by variations of the transverse pressure applied to the fiber. According to calculations [3], the induced birefringence as a function of the applied transverse pressure is described with good accuracy by the formula

$$\beta = \frac{4C_S P}{\pi r E_1}, \quad (2)$$

where C_S is a coefficient characterizing the photoelastic properties of the fiber ($C_S = 2.7 \times 10^6$ rad/m at a wavelength of 0.633 μm), P is the applied compressive load (force per unit length), E_1 is the Young modulus of the fiber, and r is the fiber radius. Figure 1 shows the results of experimental verification of the validity of formula (2) describing $\beta(P)$.

According to formula (2), a change in the phase difference between polarized modes in the proposed modulator is given by the expression

$$\delta\varphi = \delta\beta L = \frac{4C_S \delta P}{\pi r E_1} L, \quad (3)$$

where a small phase change related to the fiber length variation is ignored. The main difficulty encountered in

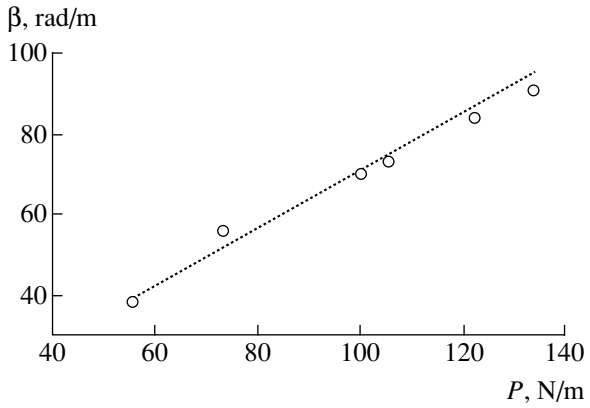

Fig. 1. A plot of the induced birefringence β versus pressing force P per unit length. Dotted line shows the results of calculation using formula (2); open circles present the experimental data.

1063-7850/04/3004-0262$26.00 © 2004 MAIK "Nauka/Interperiodica"

the determination of the efficiency of a modulator employing the transverse pressure is related to the fact that only the transducer oscillation amplitude δl is usually known and it is necessary to find the relationship between this value and the applied force variation δP.

In order to establish such a relationship, we have studied the following model problem of the theory of elasticity. Consider a cylindrical body (fiber) of length L confined between two plane-parallel plates and compressed by a static force P applied to these plates. As can be seen from Fig. 2, the total displacement l of this mechanical system is a sum of displacements of the fiber (ν_1) and the plates (ν_2),

$$l = 2\nu_1 + 2\nu_2. \quad (4)$$

Using methods of the theory of elasticity developed for the contact of cylindrical bodies [4], we obtained the following expressions for the total displacement components,

$$\nu_1 = \frac{2(1-\mu_1^2)P}{\pi E_1}\left\{\ln\left(\frac{r}{a}\right) + \ln 2 + \frac{1}{2} - \frac{1}{2(1-\mu_1)}\right\}, \quad (5)$$

$$\nu_2 = \frac{2(1-\mu_2^2)P}{\pi E_2}\left\{\ln\left(\frac{r}{a}\right) + \ln 2 + \frac{1}{2} - \frac{1}{2(1-\mu_2)}\right\}, \quad (6)$$

where μ_1, μ_2 and E_1, E_2 are the Poisson ratios and the Young moduli of the cylinder and plates, respectively, and a is the halfwidth of the contact area between cylinder and plate:

$$a = \sqrt{\frac{4Pr}{\pi}\left(\frac{1-\mu_1^2}{E_1} + \frac{1-\mu_2^2}{E_2}\right)}. \quad (7)$$

Expressions (5) and (6) have been derived assuming that a is small compared to the cylinder radius r.

Differentiating $l(P)$, we obtain the following expression for the efficiency of a modulator employing the transverse pressure:

$$K = \frac{2C_S}{r}\frac{1}{A(P)}. \quad (8)$$

Here, $A(P)$ is a dimensionless coefficient of proportionality between δl and δP:

$$\delta l = \delta P \frac{2}{\pi E_1} A(P),$$

$$A(P) = \left(1 - \mu_1^2 + \frac{E_1}{E_2}(1-\mu_2^2)\right) \times \ln\left[\frac{\pi r E_1 E_2}{P(E_1 + E_2 - \mu_1^2 E_1 - \mu_2^2 E_2)}\right] - \left[1 + \mu_1 + \frac{E_1}{E_2}(1+\mu_2)\right]. \quad (9)$$

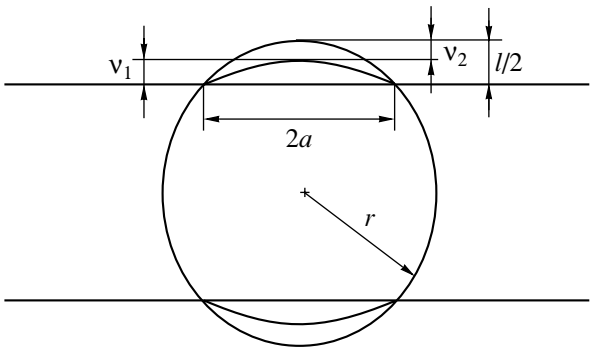

Fig. 2. Schematic diagram illustrating the straining of glass plates and optical fiber in the proposed modulator (see the text for explanations).

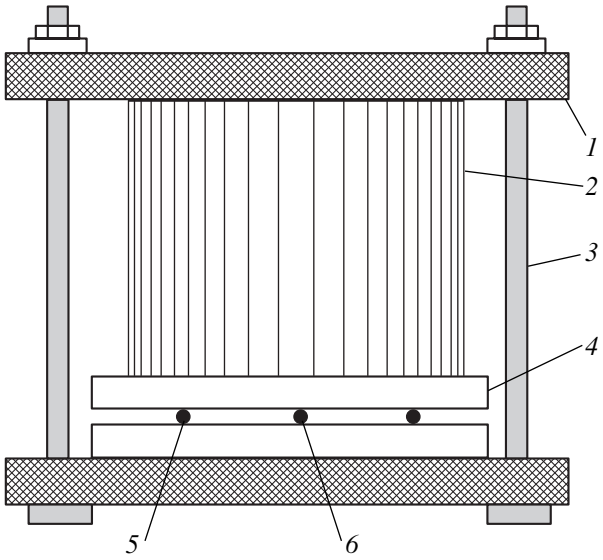

Fig. 3. Schematic diagram of the polarization modulator: (*1*) metal plates; (*2*) piezoelectric ceramic cylinder; (*3*) tightening rods; (*4*) glass plates; (*5*) fiber sections without protective jacket; (*6*) optical fiber.

The above expression indicates that the modulation efficiency K grows when the fiber stiffness decreases and the plate stiffness increases. It can also be seen that operation of the modulator requires a certain initial pressure P, but the pressure dependence $K(P)$ is rather weak (logarithmic).

We have studied a prototype of the modulator employing the transverse pressure mechanism (Fig. 3). In this mechanical system, a hollow piezoelectric ceramic cylinder with a length of 5 cm, a radius of 3.7 cm, and a wall thickness of 0.4 cm acted upon a fiber with removed protective jacket. The static pressing load could be controlled. The interaction length was $L = 8$ cm. Oscillations of the ceramic cylinder with an amplitude of δl were transmitted via glass plates and produced compression of the fiber. We have evaluated the efficiency of this modulator using formula (9) with

The modulation efficiency $K = \delta\varphi/(\delta l L)$ of various polarization modulators based on piezoelectric ceramic oscillators

Modulation mechanism	Variant	Fiber length L, m	Efficiency K, rad/(μm m)
Bending with stretching	[1]	4.6	8×10^{-4}
	[5]	0.84	0.0367
Stretching of anisotropic fiber	[6]	0.045	1.48
	[7]	0.125	0.67
Transverse pressure	This study	0.08	2000

the following parameters of the modulator: $r = 62.5$ μm; $E_1 = 7.7 \times 10^{10}$ N/m^2; $E_2 \approx 6 \times 10^{10}$ N/m^2; $\mu_1 = 0.17$; $\mu_2 = 0.25$; $P \approx 100$ N/m. Numerical calculations yielded $K = 4600$ rad/(μm m).

The results of experiments confirmed the high efficiency of the proposed polarization modulator. The experiments were performed with an isotropic fiber (not requiring orientation in the modulator). The index of modulation of the phase difference $\delta\varphi$ between polarized modes was measured using an oscillograph. The amplitude of oscillations of the ceramic transducer was measured using a Michelson interferometer with one arm incorporating the modulator with a mirror fixed on the top glass plate.

The modulation efficiency of the prototype studied in a broad frequency range was about 2000 rad/(μm m), with a modulation index of 5π rad and even higher reached for some frequencies. In addition, experiments confirmed the weak dependence of the modulation index $\delta\varphi$ on the constant component of the pressure P.

Comparative experimental values of the modulation efficiencies of devices employing various principles of the polarization modulation in optical fibers are presented in the table. The data taken from various sources were reduced to the common form $K = \delta\varphi/(\delta l L)$. As can be seen, the proposed modulator is much more effective than other devices employing piezoelectric ceramic oscillators.

Using the transverse pressure, it is also possible to increase the efficiency of modulators with fibers wound onto the external surface of the piezoelectric ceramic cylinder. This can be achieved, for example, with the aid of a metal shell squeezing the fiber. In this case, the axes of birefringence induced by bending with stretching of the fiber wound onto the cylinder coincide with the axes of birefringence induced by the transverse pressure. In the experiments with optical fibers in protective jackets, the modulation efficiency increased by a factor of 15 for piezoelectric ceramic cylinders with a radius of 1.6 cm. It should be emphasized that, in the case of winding a fiber possessing intrinsic birefringence, the orientation of its axes should be matched with the direction of induced birefringence in order to avoid undesired mode coupling [8].

REFERENCES

1. A. R. Boyain, L. Martinez-Leon, J. L. Cruz, *et al.*, Appl. Opt. **38**, 6278 (1999).
2. O. I. Kotov, L. B. Liokumovich, S. I. Markov, *et al.*, Pis'ma Zh. Tekh. Fiz. **26** (10), 28 (2000) [Tech. Phys. Lett. **26**, 415 (2000)].
3. J.-I. Sakai and T. Kimura, IEEE J. Quantum Electron. **17**, 1041 (1981).
4. A. M. Kats, *The Theory of Elasticity* (Lan', St. Petersburg, 2002) [in Russian].
5. S. C. Rashleigh, Opt. Lett. **5**, 392 (1980).
6. S. C. Rashleigh, in *Proceedings of the 1st International Conference on Optical Fiber Sensors, London, 1983*, pp. 210–213.
7. Y. Verbandt, G. van Vinckenroy, and M. R. H. Voet, in *Proceedings of the 11th International Conference on Optical Fiber Sensors, Sapporo, 1996*, pp. 340–342.
8. S. C. Rashleigh, Opt. Lett. **6**, 19 (1981).

Translated by P. Pozdeev

Technical Physics Letters, Vol. 30, No. 4, 2004, pp. 265–269. Translated from Pis'ma v Zhurnal Tekhnicheskoĭ Fiziki, Vol. 30, No. 7, 2004, pp. 14–24.

The Townsend Coefficient and Electron Runaway Characteristics in Nitrogen

A. N. Tkachev and S. I. Yakovlenko

Institute of General Physics, Russian Academy of Sciences, Moscow, 117924 Russia

Received September 22, 2003

Abstract—The results of analytical description and numerical simulation show that the Townsend ionization mechanism (characterized by a constant mean electron drift velocity and energy and by exponential growth in the number of electrons) is operative even in rather strong electric fields, for which the ionization drag of electrons can be ignored. The universal function $U_{cr}(pd)$ calculated for nitrogen establishes the relationship between the critical interelectrode voltage (separating the regions of effective multiplication and significant runaway of electrons) and the product pd of the gas pressure and interelectrode gap width. The $U_{cr}(pd)$ curve has two branches—the upper, characterizing the runaway of electrons, and the lower, describing their loss by drift. A minimum pd value on the $U_{cr}(pd)$ curve corresponds to the maximum Townsend coefficient as a function of E/p. Using the $U_{cr}(pd)$ function, an analog of the well-known Paschen curve characterizing self-sustained discharge in nitrogen has been constructed. © *2004 MAIK "Nauka/Interperiodica".*

Introduction

The Townsend ionization mechanism is characterized by exponential growth in the number of electrons as a function of the distance from the cathode, at a constant mean electron drift velocity and energy. Previously [1, 2], it was demonstrated that Townsend multiplication takes place even in rather strong fields for which the ionization drag of electrons in the gas phase can be ignored and a local criterion for significant electron runaway (according to the traditional notions [3–5]) is valid. Based on the results of numerical simulation of the process of electron multiplication in helium [1, 2] and xenon [2], we suggested a nonlocal criterion of the electron runaway.

Further analysis of the mechanism of electron runaway in a gas is presently of importance with a view to obtaining electron beams of subnanosecond duration and a record current amplitude (up to ~70 A in air and ~200 A in helium [6, 7]) at atmospheric pressure. In this paper, based on simple considerations, we elucidate the reasons for which the Townsend multiplication mechanism is still valid in strong electric fields. We will also present the results of calculations for nitrogen, analogous to those previously reported for the other gases [1, 2].

Local Criterion of Electron Runaway

Traditional approach. Let us briefly consider the main factors involved in the local criterion of electron runaway (for more detail see, e.g., [3, p. 53; 4, p. 71; 5, p. 74]). It is assumed that a steady-state electron flux from cathode to anode is nearly monoenergetic [5]. The energies ε of electrons occurring in the electric field E obey the balance equation [3–5]

$$\frac{d\varepsilon}{dx} = eE - F(\varepsilon), \tag{1}$$

where x is the distance to cathode and $F(\varepsilon)$ is the force of friction (drag) caused by the collisions of electrons with atoms in the gas phase. In the nonrelativistic case, the drag is frequently described using a simple expression obtained in the Bethe approximation,

$$F(\varepsilon) = \frac{2\pi e^4 ZN}{\varepsilon}\ln\left(\frac{2\varepsilon}{I}\right), \tag{2}$$

where Z is the number of electrons in the neutral gas species (atoms or molecules), N is the number density of these neutral particles in the gas, and I is the mean inelastic loss energy. Expression (2), despite the rough character of this approximation, shows (like more precise calculations) the presence of a maximum in the value of F as a function of the electron energy, $F_{max} = F(\varepsilon_{max})$. The maximum of function (2) occurs at $\varepsilon_{max} = 2.72I/2$. In particular, for helium $I = 44$ eV and $\varepsilon_{max} = 2.72I/2 = 60$ eV, while a more exact calculation yields $\varepsilon_{max} \approx 100$ eV. For nitrogen, $I = 80$ eV and $\varepsilon_{max} = 2.72I/2 = 109$ eV, while a more exact calculation yields $\varepsilon_{max} \approx 103$ eV.

According to the traditional approach [3–5], the condition of electron runaway from a gas consists in that the electric field has to be sufficiently strong, $E > E_{cr1}$, where the critical field strength E_{cr1} is determined by the maximum drag as $E_{cr1} = F_{max}/e$. In particular,

proceeding from formula (2), we eventually obtain an expression for the critical field [4],

$$E_{\mathrm{cr1}} = 4\pi e^3 ZN/(2.72I), \text{ or}$$
$$E_{\mathrm{cr1}/p} = 3\times 10^3 Z/(\mathrm{I/eV})\ \mathrm{V/(cm/Torr)}, \quad (3)$$

where p is the gas pressure at 300 K. For example, $E_{\mathrm{cr1}}/p \approx 140$ V/(cm Torr) in helium and $E_{\mathrm{cr1}}/p \approx 590$ V/(cm Torr) in nitrogen. The criterion $E > E_{\mathrm{cr1}}$ is local, which means that the critical field E_{cr1} is determined only by the properties of neutral gas particles and the gas density at a given point of the system.

Now we will demonstrate that, in contrast to the commonly accepted notions, the through flight regime with continuous acceleration of the main fraction of electrons in gases is not realized even for $E \gg E_{\mathrm{cr1}}$, provided that the distance to cathode is sufficiently large.

Average electron energy limited by multiplication. It is necessary to emphasize one important circumstance: even for $E > E_{\mathrm{cr1}}$, the mean energy of electrons will not infinitely grow with the distance x. The traditional approach outlined above does not take into account the multiplication of electrons. In fact, the mean electron energy ε^* has to be determined proceeding from an equation taking into account the change in the number of electrons, rather than from Eq. (1).

In the simplest form, the law of energy conservation within the approximation corresponding to Eq. (1) can be written as

$$\frac{d(N_e\varepsilon^*)}{dx} = eEN_e - F(\varepsilon^*)N_e, \quad (4)$$

where $N_e(x)$ is the electron density at a point with the coordinate x. Taking into account that $dN_e/dx = \alpha_i N_e$, where α_i is the Townsend multiplication coefficient, and using Eq. (4), we obtain

$$\frac{d\varepsilon^*}{dx} = eE - F(\varepsilon^*) - \alpha_i\varepsilon^*. \quad (5)$$

This relation, in contrast to the balance equation (1), contains the negative term $(-\alpha_i\varepsilon^*)$ showing that the energy supplied by the field is "smeared" over all electrons, including the newborn ones. Therefore, even with complete neglect of the drag in the gas (for $F(\varepsilon) = 0$), the mean electron energy is limited from above as $e^* < \varepsilon^*_{\max} = eE/\alpha_i$. Accordingly, Eq. (1) cannot be considered as determining the mean electron energy, and the electron energy distribution cannot be treated as monoenergetic. Only when there is no ionization in the system ($\alpha_i = 0$), as, for example, in fully ionized plasma, does the traditional approach based on Eq. (1) become valid.

The above considerations imply that, for the main fraction of electrons, the Townsend multiplication regime (for which the fraction of permanently accelerated electrons is small) is realized even in supercritical fields ($E > E_{\mathrm{cr1}}$), where, according to the conventional notions, all electrons are continuously accelerated. Of course, there is a certain fraction of fast electrons exhibiting continuous acceleration; moreover, these electrons can even play a significant role in preionization of the gas. However, the fraction of such electrons at a certain distance from the cathode will become small relative to the total number of electrons, since the mean electron energy at this distance ceases to grow. In this context, let us consider the results of numerical simulation.

Electron Multiplication and Runaway in Nitrogen

Description of the model. We have calculated the ionization characteristics of nitrogen within the framework of the model described in [1, 2, 8, 9]. According to this model, electrons were generated on a cathode with randomly directed initial velocities and the Poisson energy distribution with a mean value of $\varepsilon_0 = 0.2$ eV. The equations of motion for all electrons were solved within small time steps, and the elastic and inelastic collisions were played with the probabilities determined by cross sections of the corresponding elementary events. The cross section and inelastic energy losses as functions of the initial electron energy are depicted in Fig. 1. The total cross section of the interaction of an electron with a nitrogen molecule was determined using data from [10–13] and the ionization cross sections were determined using data from [14–17]. We took into account the excitation of the ten lowest electron states of a nitrogen molecule (using the data from [18, 19]) and considered the eight lowest vibrational levels (by data from [20–22]). The results presented below refer to the case of plane electrodes spaced by the distance d and biased by the voltage U. For a passage to the case of coaxial cylinders, see [9].

The Townsend ionization regime. The results of our calculations showed that the Townsend ionization actually takes place, while the runaway electrons are absent, at all values of the reduced field strength E/p in the range from 10 to 10^5 V/(Torr cm) and a sufficiently large spacing d between the electrodes. This character of ionization is confirmed by the fact that the number of excitation and electron generation events exponentially increases with the distance x from the cathode, while certain constant mean velocity and energy of electrons are established at a sufficiently large distance from the cathode. In this range, both the mean electron energy (ε^*) and the mean velocity projection onto the x axis (u_x) cease to depend on the distance x. The maximum of the energy distribution for electrons reaching the anode occurs in the region of small energies $\varepsilon^* \ll eU$.

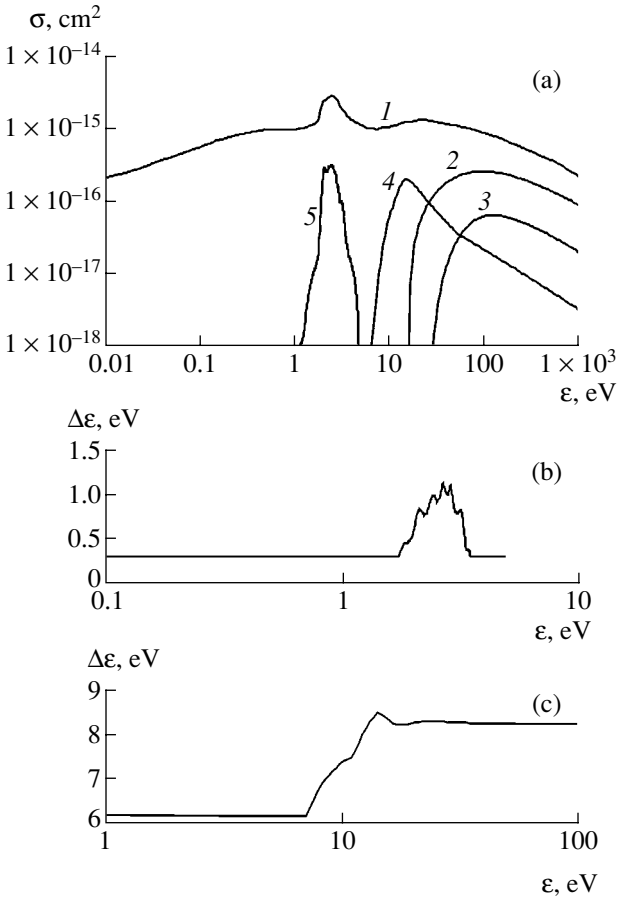

Fig. 1. Plots of (a) the cross sections σ of interactions of an electron with a nitrogen molecule (*1*, total; *2*, ionization; *3*, dissociative ionization; *4*, excitation of electron states; *5*, excitation of vibrational states) and (b, c) the energy losses Δε for the excitation of vibrational and electron states, respectively, versus the electron energy ε (by data of [10–21]).

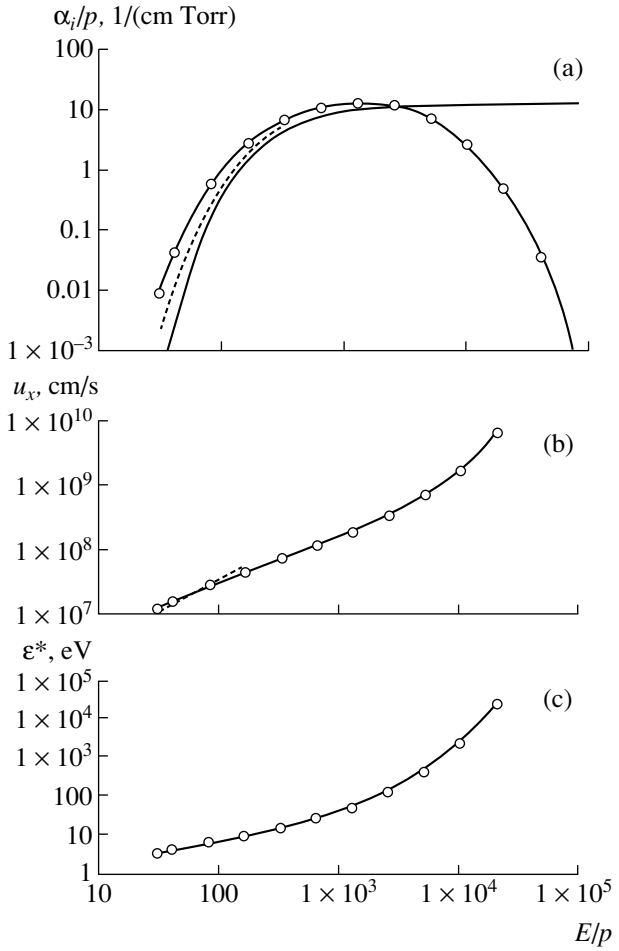

Fig. 2. Plots of the normalized ionization and drift characteristics versus reduced electron energy E/p for nitrogen: (a) Townsend coefficient α_i/p; (b) mean electron velocity projection u_x; (c) mean electron energy ε*. Open circles show the results of simulation obtained in this study for various field strengths at $p = 100$ Torr ($N = 3.22 \times 10^{18}$ cm^{-3}); thick solid curve in (a) shows the approximation according to Eq. (6); dashed curves represent the results of simulations reported in [18].

The Townsend multiplication coefficient α_i is determined by the slope of a plot of the logarithm of the number of ionization events versus current. The α_i value has proved to be proportional to the gas density (pressure) and can be written in the form $\alpha_i(E, p) = p\xi(E/p)$. For nitrogen, the function $\xi(E/p)$ obeys the experimentally established approximation [5]

$$\xi(E/p) = A\exp\left(-B\left(\frac{p}{E}\right)\right), \qquad (6)$$

where $A = 12$ (cm Torr)$^{-1}$ and $B = 342$ V/(cm Torr) for $E/p = 100$–600 V/(cm Torr) and $A = 8.8$ (cm Torr)$^{-1}$ and $B = 275$ V/(cm Torr) for $E/p = 27$–200 V/(cm Torr).

However, our calculations showed (Fig. 2) that this approximation for nitrogen is valid only for relatively small reduced field strengths $E/p < (E/p)_{max} = 1500$ V/(cm Torr). As the E/p value increases above the critical level, the multiplication coefficient α_i begins to decrease.

It should be noted that the peak field strength E_{max} is about 2.5 times the above estimates for E_{cr1} ($E_{cr1}/p = 590$ V/(cm Torr)), but it should be recalled that formula (2) was obtained in a very rough approximation. In fact, E_{cr1} determines the condition of a drop in the Townsend multiplication coefficient for $E > E_{cr1}$ rather than the condition of continuous acceleration of the main fraction of electrons with increasing distance x. In this sense, the values of E_{max} presented here and in [1, 2] are merely the refined values of E_{cr1}.

Nonlocal Criterion of Electron Runaway

Critical voltage. The results of our calculations showed that the Townsend ionization regime is established at a certain distance from the cathode $x \sim \alpha_i^{-1}$,

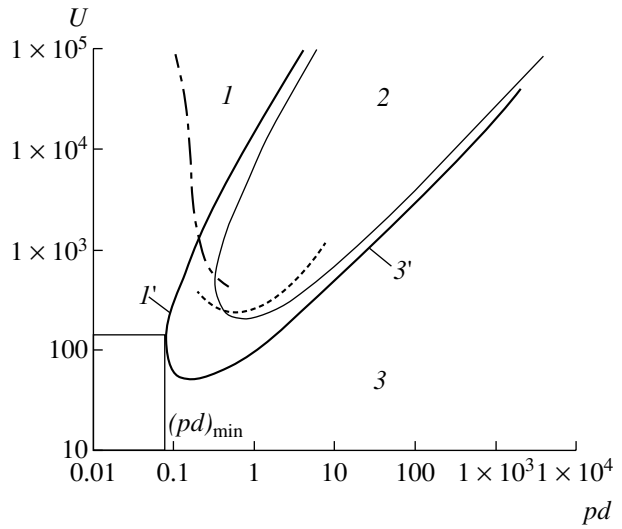

Fig. 3. Criteria of the electron runaway, $U_{cr}(pd)$ (thick solid curve), and the self-sustained discharge initiation, $U_{br}(pd)$ for $L = \ln(1 + 1/\gamma) = 4.0$ (thin solid curve), in nitrogen: (*1*) electron runaway region; (*1*') runaway curve; (*2*) region of electron multiplication and self-sustained discharge; (*3*) electron drift region; (*3*') drift curve. Dash and dash–dot curves show the experimental data from [5] and [22], respectively.

which corresponds to the characteristic multiplication length. For sufficiently small interelectrode distances, $d < \alpha_i^{-1}$, the pattern of electron multiplication substantially differs from that in the Townsend regime. A significant fraction of electrons are continuously accelerated with increasing distance from the cathode, so that both the mean velocity projection u_x and the mean energy ε^* increase with x. The peak of the energy distribution function for electrons reaching the anode corresponds to the maximum energy $E = eEd$ acquired by the particle upon the flight from cathode to anode.

Recently, we proposed [6, 7], in contrast to the commonly accepted notions [3–5], to consider the electron runaway as predominating when the interelectrode spacing d is comparable with the characteristic multiplication length, that is, with the inverse Townsend coefficient α_i^{-1}: when $\alpha_i d < 1$, the runaway electrons dominate in the spectrum of electrons reaching the anode. Accordingly, the electron runaway criterion determining the critical electric field strength E_{cr} is as follows:

$$\alpha_i(E_{cr}, p)d = 1. \quad (7)$$

For plane electrodes ($E_{cr} = U_{cr}/d$), we obtain

$$pd\xi(E_{cr}/p) = 1 \text{ or } pd\xi(U_{cr}/pd) = 1. \quad (8)$$

This formula implicitly takes into account the dependence of the critical voltage U_{cr} (corresponding to the onset of a significant electron runaway) on the product pd of the gas pressure and the interelectrode spacing (Fig. 3). The $U_{cr}(pd)$ curve separates the region of effective electron multiplication from that of effective runaway, where electrons can leave the discharge gap before being involved in the multiplication process. This curve is universal for the given gas.

Upper and lower branches of the electron loss curve. The $U_{cr}(pd)$ curve, describing the loss of electrons from the system, can be divided into lower and upper branches (Fig. 3). The turning point, corresponding to the minimum product $pd = (pd)_{min}$, will be considered as the boundary between the two branches. It can be shown that this point corresponds to the maximum of the $\xi(x)$ function. Indeed, consider pd as a function of U_{cr}. For the condition $\frac{d(pd)}{dU_{cr}} = 0$, relations (8) imply that $\xi'(x) = 0$, which is just the condition of maximum for $\xi(x)$. Thus, the boundary point determined by the minimum value of pd on the runaway curve $U_{cr}(pd)$ corresponds to the value of the reduced electric field strength, $E/p = (E/p)_{max}$, for which the reduced Townsend coefficient $\alpha_i/p = \xi(E/p)$ reaches a maximum.

The region above the upper branch of the $U_{cr}(pd)$ curve represents the situation when electrons acquire large energies while traveling over the mean free path and leave the discharge gap without participating in multiplication because of a drop in the ionization cross section with increasing energy. For this reason, the region above this branch may be called electron runaway (through flight) region, and this branch is naturally referred to as the runaway curve.

In the region under the lower branch of the electron loss curve, electrons traveling over the mean free path length acquire relatively small energies, which fall within the increasing branch of the ionization cross section as a function of the electron energy. In this region, electrons drift from cathode to anode without gaining energies sufficient for the effective multiplication. Therefore, the region below the lower branch of the electron loss curve may be called the electron drift region, and this branch is naturally referred to as the drift curve.

Upper branch of the curve of self-sustained discharge initiation. The curve determining the criterion of discharge initiation is usually constructed based on the condition that each electron must generate a number of ions sufficiently large to provide that the secondary emission will ensure the production of another electron on the cathode. Accordingly, the discharge initiation (gas breakdown) potential $U_{br}(pd)$ is determined by the condition (see, e.g., [5])

$$\alpha_i(E, p)d = \ln(1 + 1/\gamma) \quad \text{or} \quad pd\xi(U_{br}/pd) = L, \quad (9)$$

where $L = \ln(1 + 1/\gamma)$ and γ is the secondary electron emission coefficient. Comparing the criteria of discharge initiation and electron runaway, we obtain the relation $U_{br}(pd) = LU_{cr}(pd/L)$.

It should be noted, however, that the character of the discharge initiation curve $U_{br}(pd)$ is not as general as that of the electron loss curve $U_{cr}(pd)$. The latter curve is the universal characteristic of a given gas, whereas the $U_{br}(pd)$ curve depends on the model used to describe the initiation of discharge. In particular, the left branch of the Paschen curve depends on the properties of electrodes.

Conclusions

Based on a simple equation taking into account the multiplication of electrons, it was demonstrated that a constant mean electron drift velocity is established at a certain distance from the cathode even when the electric field strength E is large so that the ionization drag of electrons can be ignored. This implies that the local criterion of electron runaway (through flight) fails to be valid under the conditions of electron multiplication.

These conclusions are confirmed by the results of numerical simulation of the process of electron multiplication and transport in nitrogen. A universal function characterizing the conditions of electron runaway in nitrogen has been determined.

Acknowledgments. The authors are grateful to V.F. Tarasenko for stimulating discussions.

This study was supported by the International Scientific-Technological Center, grant no. 1270.

REFERENCES

1. A. N. Tkachev and S. I. Yakovlenko, Pis'ma Zh. Éksp. Teor. Fiz. **77**, 264 (2003) [JETP Lett. **77**, 221 (2003)].
2. A. N. Tkachev and S. I. Yakovlenko, Pis'ma Zh. Tekh. Fiz. **29** (16), 54 (2003) [Tech. Phys. Lett. **29**, 683 (2003)].
3. L. P. Babich, T. V. Loĭko, and V. A. Tsukerman, Usp. Fiz. Nauk **160** (7), 49 (1990) [Sov. Phys. Usp. **33**, 521 (1990)].
4. Yu. D. Korolev and G. A. Mesyats, *The Physics of Pulse Breakdown in Gases* (Nauka, Moscow, 1991).
5. Yu. P. Raizer, *Gas Discharge Physics* (Nauka, Moscow, 1992; Springer-Verlag, Berlin, 1991), Fig. 3.3.
6. V. F. Tarasenko, S. I. Yakovlenko, V. M. Orlovskiĭ, *et al.*, Pis'ma Zh. Éksp. Teor. Fiz. **77**, 737 (2003) [JETP Lett. **77**, 611 (2003)].
7. S. B. Alekseev, V. M. Orlovskiĭ, V. F. Tarasenko, *et al.*, Pis'ma Zh. Tekh. Fiz. **29** (16), 45 (2003) [Tech. Phys. Lett. **29**, 679 (2003)].
8. A. N. Tkachev and S. I. Yakovlenko, Proc. SPIE **4747**, 271 (2002).
9. A. N. Tkachev and S. I. Yakovlenko, Laser Phys. **12**, 1022 (2002).
10. A. G. Engelhardt, A. V. Phelps, and C. G. Risk, Phys. Rev. **135**, A1566 (1964).
11. D. E. Golden, Phys. Rev. Lett. **17**, 847 (1966).
12. H. J. Blaauw, R. W. Wagenaar, D. H. Barends, and F. J. de Heer, J. Phys. B **13**, 359 (1980).
13. G. Dalba, P. Fornasini, R. Grisenti, *et al.*, J. Phys. B **13**, 4695 (1980).
14. E. Krishnakumar and S. K. Srivastava, J. Phys. B **23**, 1893 (1990).
15. C. Tian and C. R. Vidal, J. Phys. B **31**, 5369 (1998).
16. D. Rapp, P. Englander-Golden, and D. P. Briglia, J. Chem. Phys. **42**, 4081 (1965).
17. B. L. Schram, F. J. de Heer, M. J. van der Wiel, and J. Kistemaker, Physica **31**, 94 (1965).
18. L. Campbell, M. J. Brunger, A. M. Nolan, *et al.*, J. Phys. B **34**, 1185 (2001).
19. D. C. Cartwright, A. Chutjian, S. Trajmar, and W. Williams, Phys. Rev. A **16**, 1041 (1977).
20. G. J. Schulz, Rev. Mod. Phys. **45**, 423 (1973).
21. M. Vicic, G. Poparic, and D. S. Belic, J. Phys. B **29**, 1273 (1996).
22. V. I. Babanin and A. Ya. Ender, Zh. Tekh. Fiz. **44**, 102 (1974) [Sov. Phys. Tech. Phys. **19**, 60 (1974)].

Translated by P. Pozdeev

Technical Physics Letters, Vol. 30, No. 4, 2004, pp. 270–271. Translated from Pis'ma v Zhurnal Tekhnicheskoĭ Fiziki, Vol. 30, No. 7, 2004, pp. 25–29.

The Effect of Hydrogen on the Shear Modulus of Quasibinary Alloys of the TiNi–TiCu System

N. E. Skryabina[a], L. V. Spivak[a,*], and A. V. Shelyakov[b]

[a] *Perm State University, Perm, Russia*

[b] *Moscow Physical Engineering Institute (State Technical University), Moscow, Russia*

* *e-mail: levspivak@permonline.ru*

Received October 14, 2003

Abstract—Hydrogen saturation of amorphous quasibinary alloys of the TiNi–TiCu system is accompanied by a catastrophic decrease in their shear moduli. The effect is not related to the formation of new phases or structural components during hydrogenation. *© 2004 MAIK "Nauka/Interperiodica".*

Introduction. Previously [1–3], we observed an unusual phenomenon in iron-based amorphous alloys oversaturated with hydrogen or deuterium, whereby the samples reversibly lost strength and passed to the so-called "quasi-liquid" state. A special feature of this state is that a material, while showing a quite significant resistance to normal stresses, exhibits a catastrophic decrease in the resistance to shear. However, direct measurements of the shear moduli of the alloys immediately in the course of hydrogenation encountered difficulties, the main of which was related to a rapid elimination of hydrogen from the samples after termination of the saturation process.

Nickel titanium alloys, in particular–amorphous quasibinary alloys of the TiNi–TiCu system, are characterized by a rather high coefficient of hydrogen diffusion at 300 K (~10^{-11} m^2/s) and a large hydrogen sorption capacity (much greater compared to that of iron-based amorphous alloys). Moreover, NiTi alloys are capable of retaining hydrogen for a sufficiently long time at 300 K, while complete elimination of hydrogen from these alloys is observed only on heating above 700–800 K [4]. In this respect, such alloys offer a convenient model system for the verification of hypotheses explaining the nature of the "quasi-liquid" state observed in hydrogenated amorphous metals.

Experimental. The experiments were performed with samples of rapidly quenched $Ti_{50}Ni_{25}Cu_{25}$ alloy ribbons with a thickness of 40–60 μm obtained by methods of melt spinning or planar casting at a cooling rate of 10^4–10^6 K/s. The results of X-ray diffraction investigations [5–7] showed that the samples cooled at a rate of 10^4 K possessed a crystalline structure. Cooling at a rate of 10^6 K/s resulted in complete amorphization, while the samples obtained at an intermediate cooling rate about 10^5 K/s possessed a mixed amorphous-crystalline structure.

The shear modulus was determined using the method of torsional oscillations at a frequency on the order of 1 Hz. The period of oscillations was measured to within 0.01% using a system of photodiodes and the corresponding electronics. The samples were hydrogenated as cathodes in a temperature-controlled electrochemical cell with a platinum wire anode. The cell was mounted immediately in the system measuring the period of oscillations. The process was conducted in an H_2SO_4 based electrolyte at a cathode current density varied in the interval from 50 to 800 A/m^2.

Results and discussion. The influence of saturation with hydrogen for various times on the shear moduli of samples occurring in various structural states (crystalline, amorphous-crystalline, and amorphous) is illustrated in Fig. 1. The hydrogen-induced increase in the shear modulus of a crystalline sample (Fig. 1a) was previously observed in a NiTi alloy [4], where the effect was much less pronounced. It was established that this phenomenon is related to the hydrogen-stimulated phase transitions accompanied by the formation of a high-modulus phase.

Hydrogenation of a sample in the amorphous state (Fig. 1c) was accompanied by a significant decrease in the shear modulus in the very first minutes of the initial saturation stage. An analysis of the X-ray diffraction patterns showed neither the formation of new phases nor the transition from amorphous to crystalline state. Thus, the observed decrease in the shear modulus can be related only to the presence of excess hydrogen (above the equilibrium solubility level) resulting from the electrochemical saturation process at a cathode current density in the indicated range.

The samples occurring in a mixed amorphous-crystalline state exhibited a superposition of the effects of hydrogen on the crystalline and amorphous structural components (Fig. 1b). Therefore, the influence of hydrogen on the shear modulus of such samples is more

1063-7850/04/3004-0270$26.00

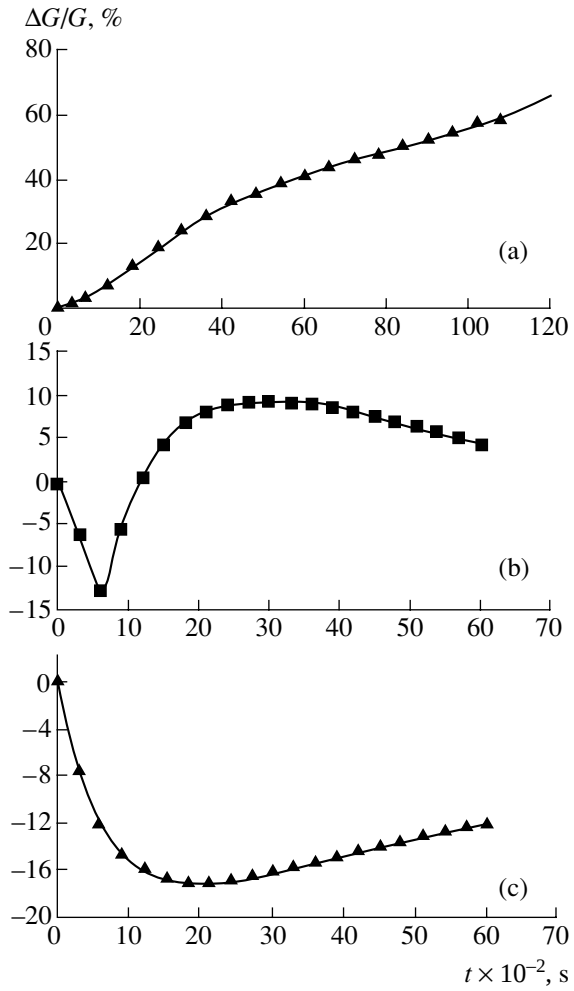

Fig. 1. The influence of the duration of hydrogen saturation at a cathode current density of 50 A/m^2 on the shear moduli of $Ti_{50}Ni_{25}Cu_{25}$ alloys in different structural states: (a) crystalline; (b) amorphous-crystalline; (c) amorphous.

pronounced in alloys with the structure occurring in a less equilibrium state.

Thus, we have observed for the first time a catastrophic decrease in the shear modulus of amorphous quasibinary alloys of the TiNi–TiCu system in the course of electrochemical saturation with hydrogen. On the one hand, this fact is the first experimental evidence in favor of the assumptions formulated previously [1–3] concerning the nature of the reversible loss of shape. On the other hand, our observations show evidence of a change of the interatomic interaction forces in the presence of a high concentration of hydrogen in materials with disordered structures. This is a quite substantial result, since virtually all theories describing the deformation and fracture of alloys in the presence of hydrogen (see, e.g., [8, 9]) admit a priori that the shear modulus (entering into many essential relations) remains constant. The results of our experiments show that such assumptions have to be seriously verified.

Acknowledgments. The authors gratefully acknowledge support from the Russian Foundation for Basic Research, project no. 03-02-16561.

REFERENCES

1. N. E. Skryabina, L. V. Spivak, V. P. Vylezhnev, *et al.*, Pis'ma Zh. Tekh. Fiz. **22** (23), 36 (1996) [Tech. Phys. Lett. **22**, 965 (1996)].
2. N. E. Skryabina, L. V. Spivak, M. A. Khominskiĭ, *et al.*, Fiz. Met. Metalloved. **83** (3), 139 (1997).
3. N. Ye. Skryabina and L. V. Spivak, Int. J. Hydrogen Energy **24**, 795 (1999).
4. L. V. Spivak, N. E. Skryabina, and V. N. Khachin, Fiz. Met. Metalloved. **79** (4), 138 (1995).
5. A. V. Shelyakov, N. M. Matveeva, and S. G. Larin, in *Shape Memory Alloys: Fundamentals, Modeling and Industrial Applications*, Ed. by F. Trochu and V. Brailovski (Canadian Inst. of Mining, Metallurgy and Petroleum, 1999), pp. 295–303.
6. H. Rösner, P. Schlossmacher, A. V. Shelyakov, *et al.*, Acta Mater. **49**, 1541 (2001).
7. P. L. Potapov, A. V. Shelyakov, and D. Schryvers, Scr. Mater. **44**, 1 (2001).
8. B. A. Kolachev, *The Hydrogen Brittleness of Metals* (Metallurgiya, Moscow, 1985) [in Russian].
9. T. Y. Zhang, W. Y. Chu, and C. M. Hsiao, Scr. Metall. **20**, 225 (1986).

Translated by P. Pozdeev

Technical Physics Letters, Vol. 30, No. 4, 2004, pp. 272–274. Translated from Pis'ma v Zhurnal Tekhnicheskoĭ Fiziki, Vol. 30, No. 7, 2004, pp. 30–35.

The Effect of Exposure to Arsenic Flow on the Optical Properties of Quantum Dot Arrays in the InAs/GaAs(100) System

V. G. Dubrovskii[a], N. V. Kryzhanovskaya[a], V. M. Ustinov[a], A. A. Tonkikh[b], V. A. Egorov[b], N. K. Polyakov[b], Yu. B. Samsonenko[b], and G. E. Cirlin[a]

[a] *Ioffe Physicotechnical Institute, Russian Academy of Sciences, St. Petersburg, 194021 Russia*

[b] *Institute of Analytical Instrument Building, Russian Academy of Sciences, St. Petersburg, Russia*

Received October 16, 2003

Abstract—The optical properties of quantum dot arrays in the MBE-grown InAs/GaAs(100) epitaxial system with an effective InAs layer thickness of 1.9 monolayers were studied in samples exposed to the beam of As_4 for various times after switching off the In beam. The results of photoluminescence measurements showed that the emission wavelength increased with the exposure time within certain limits. This behavior agrees with predictions of the kinetic model of the initial stage of quantum dot formation. © *2004 MAIK "Nauka/Interperiodica".*

In recent years, there has been rapid growth in the number of publications devoted to the influence of heteroepitaxial growth conditions on the structural and optical properties of quantum dot (QD) arrays. This is related to the need for developing methods for obtaining QD arrays with the properties required in particular applications. For example, the size of QDs in the heterostructures for optoelectronic devices has to correspond to the working wavelength, while the QD density must be sufficient to provide for the required laser gain [1]. It was demonstrated both experimentally [2, 3] and theoretically [4, 5] that the structural parameters of QR arrays can be controlled by selecting the appropriate growth conditions, such as the substrate temperature, growth rate, effective layer thickness, and the time of exposure to a molecular beam (e.g., of arsenic).

This study continues systematic quantitative investigation [3–5] of the effect of controllable technological parameters of epitaxial growth on the properties of QD arrays in the InAs/GaAs(100) system. We present the results of photoluminescence (PL) measurements for InAs quantum dots grown by molecular beam epitaxy (MBE) on single crystal GaAs(100) substrates. The effective thickness of deposited InAs, the growth temperature, and the rate of InAs deposition were fixed, while the time of the final exposure to the As_4 beam was varied.

According to the results of a theoretical analysis [5] based on the kinetic model of QD formation under the action of elastic stresses [4], the kinetics of the average lateral island size variation with time is described by the following equation in dimensionless variables:

$$\frac{t - t_c}{t_R} = \ln\left[\frac{(1 + l + l^2)^{1/2}}{1 - l}\right] - \sqrt{3}\arctan\left(\frac{2l + 1}{\sqrt{3}}\right) + \frac{\pi}{2\sqrt{3}} \equiv U(l). \quad (1)$$

Here, $t = t_0 + t_{exp}$; $t_0 = H_0/V$ is the time required for depositing H_0 monolayers (ML) of InAs at a given deposition rate V [ML/s]; $t_c = H_c/V$ is the time required for obtaining a wetting layer of the critical thickness H_c [1] (for the system under consideration, $H_c \sim 1.7$ ML); $l = L/L_R$; L is the average lateral size of the islands; and L_R is the quasi-stationary lateral size upon termination of the relaxation stage lasting for about $3t_R$, where t_R is the characteristic relaxation time. It should be noted that the values of L_R and t_R (determined by expressions derived in [5]) depend on the system energetics, lattice mismatch, island geometry, effective thickness H_0, substrate surface temperature T, and growth rate V. Assuming that the island shape in the initial growth stage remains unchanged and the parameters H_0, T, and V are maintained constant, the values of L_R and t_R can also be considered as constants determined by these parameters.

Since the right-hand part of Eq. (1) does not contain any model parameters, the dependence of l on $(t - t_c)/t_R$ (determined through inversion of Eq. (1)) has a universal form depicted in Fig. 1. For the given values of the effective thickness, temperature, and growth rate, the theory predicts a monotonic increase in the average island size with the exposure time. For large times

$t \sim t_c + 3t_R$, the island size exhibits saturation and approaches the quasi-stationary size $L = L_R$. In the quasi-stationary state, all substance present in the wetting layer in excess of the amount corresponding to the equilibrium layer thickness (determined by the balance of contact and elastic forces in accordance to the Müller–Kern criterion [6]) is distributed within the islands. The adopted theoretical model [4] also predicts that the relative dispersion of the distribution of islands with respect to the lateral size decreases with increasing exposure time.

The experiments were performed in an MBE setup of the EP1203 type using semi-insulating single crystal GaAs(100) substrates. In a series of four samples, the active region was formed by depositing an InAs layer with an effective thickness of 1.9 ML at a deposition rate of $V = 0.03$ ML/s, followed by exposure to the As_4 beam for $t_{exp} = 0$, 7.5, 15, and 22.5 s. The substrate temperature during QD layer formation, exposure to arsenic, and GaAs coating was $T = 485$°C (a 5-nm-thick GaAs layer was deposited in order to avoid indium loss by evaporation from QDs). The process of InAs QD deposition was monitored by reflection high-energy electron diffraction (RHEED). The observed RHEED patterns showed that a sharp transition from linear to point diffraction (characteristic of the three-dimensional island growth) in all cases took place after deposition of the InAs layer with a thickness of about 1.7 ML.

In order to eliminate the transport of nonequilibrium carriers into a near-surface region and into the substrate in the course of optical measurements, the active region was bounded from both sides by short-period superlattices $Al_{0.25}Ga_{0.75}As$/GaAs (5 pairs, 25 Å/25 Å). Finally, a 5-nm-thick protective GaAs layer was deposited. The buffer layer, superlattices, and the upper GaAs layer were deposited at a temperature of 600°C. The partial pressure of As_4 in the growth chamber did not exceed 1.5×10^{-6} Pa. The PL spectra were excited by an Ar^+ laser ($\lambda = 514.5$ nm; beam power density, ~100 W/cm^2). The emission was measured with a cooled Ge photodiode.

Figure 2 shows the room-temperature PL spectra of two samples, for which the exposures to arsenic after QD layer growth were $t_{exp} = 0$ and 7.5 s. The inset in Fig. 2 presents experimental data showing variation of the emission wavelength depending on the exposure time. As can be seen from the PL spectra, an increase in t_{exp} leads to narrowing (from ~80 to ~30 meV) of the emission band corresponding to radiative recombination via the ground state in QDs. This is evidence of a more homogeneous distribution of the QD size. Obtaining QD arrays with homogeneous QD dimensions is important in many applications. In particular, this is a necessary requirement for the formation of "quantum molecules" [7].

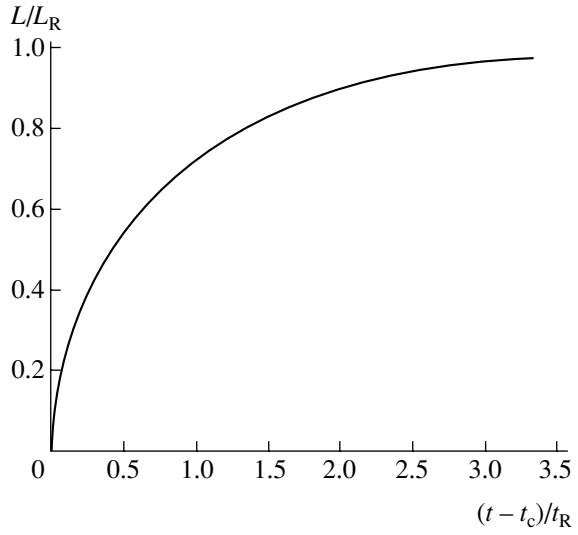

Fig. 1. Universal plot of the reduced average island size L/L_R versus dimesionless time $(t - t_c)/t_R$ in the stage of QD size relaxation.

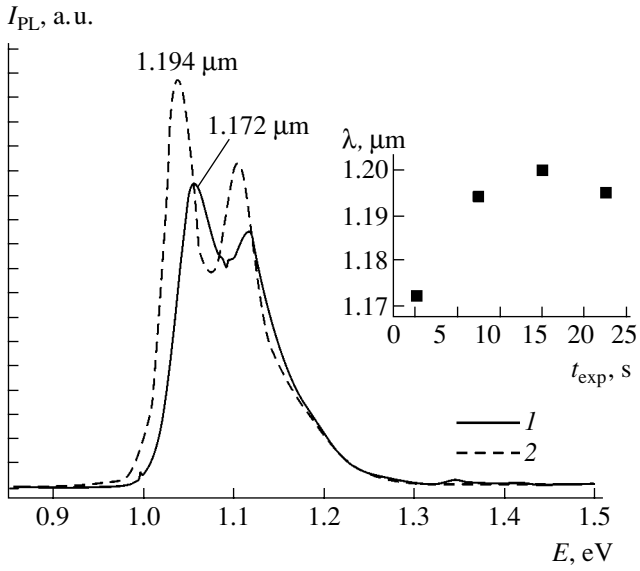

Fig. 2. Room-temperature PL spectra of an MBE-grown heterostructures with 1.9-ML InAs quantum dots exposed to arsenic beam for $t_{exp} = 0$ (*1*) and 7.5 s (*2*) after switching off the In beam. The inset shows the experimental plot of the wavelength of emission from QDs versus the exposure time.

As the exposure time increases to 15 s, the position of the PL band maximum on the wavelength scale shifts toward higher values, but further increase in t_{exp} leads to a shift to shorter wavelengths. The initial increase in the emission wavelength is explained by the QD size growing in the course of exposure to arsenic as a result of the absorption of substance from the wetting layer. Thus, the experimental data and theoretical predictions qualitatively agree for exposure times up to ~15 s. Then, since the amount of substance in the wetting layer is limited, the QD size and, hence, the emission wave-

length could be expected to exhibit an asymptotic behavior (Fig. 1).

However, an increase in the exposure time to t_{exp} = 22.5 s leads to a shift toward shorter wavelengths. This behavior can be explained as follows. Because of the initial scatter in the QD size, the QDs grow with different rates during the exposure to arsenic: the substance from the wetting layer is attached predominantly over a perimeter of each island. As a result, large QDs grow to such an extent that the accumulated elastic stresses induce a dislocation that makes the radiative recombination mechanism inoperative. This explanation is confirmed by the observed decrease in the integral intensity of emission. Our samples were grown at a relatively low deposition rate (~0.03 ML/s), which allows QDs of greater size to be obtained in the initial deposition stage [3] as compared to the size of QDs grown at a usual rate of 0.1 ML/s. The wavelength of emission from the wetting layer decreases with the time of exposure, which is evidence of a decrease in the layer thickness. In order to study the structure of such systems in more detail, we are planning to use transmission electron microscopy (including high-resolution measurements).

Thus, we have theoretically predicted and experimentally verified two tendencies in the formation of QDs by InAs deposition followed by exposure to the arsenic beam: (i) an increase in the QD size when the exposure time increases (in our experiments) to 15 s and (ii) an increase in the homogeneity of the QD size distribution. The latter circumstance can be used for the formation of structures in which the homogeneity of the QD size is a necessary requirement, as in the case of devices with "quantum molecules."

Acknowledgments. G.E.C. is grateful to the Alexander von Humboldt Foundation (Germany); V.M.U. gratefully acknowledges support from the Russian Science Support Foundation.

This study was supported in part by the INTAS Foundation, the Ministry of Science and Technology of the Russian Federation, and the Russian Foundation for Basic Research.

REFERENCES

1. D. Bimberg, M. Grundmann, and N. N. Ledentsov, *Quantum Dot Heterostructures* (Wiley, Chichester, 1999).
2. R. Songmuang, S. Kiravittaya, M. Sawadsaringkarn, *et al.*, J. Cryst. Growth **251**, 166 (2003).
3. V. G. Dubrovskii, V. A. Egorov, G. E. Cirlin, *et al.*, Fiz. Tekh. Poluprovodn. (St. Petersburg) **37**, 883 (2003) [Semiconductors **37**, 855 (2003)].
4. V. G. Dubrovskii, G. E. Cirlin, and V. M. Ustinov, Phys. Rev. B **68**, 075409 (2003).
5. V. G. Dubrovskii, Phys. Status Solidi B **238**, R1 (2003).
6. P. Müller and R. Kern, Appl. Surf. Sci. **102**, 6 (1996).
7. Z. R. Wasilevski, S. Fafard, and J. P. McCaffrey, J. Cryst. Growth **201**–**202**, 1131 (1999).

Translated by P. Pozdeev

Technical Physics Letters, Vol. 30, No. 4, 2004, pp. 275–277. Translated from Pis'ma v Zhurnal Tekhnicheskoĭ Fiziki, Vol. 30, No. 7, 2004, pp. 36–41.

A Particle Energy Analyzer of the Cylindrical Mirror Type

L. P. Ovsyannikova* and T. Ya. Fishkova

Ioffe Physicotechnical Institute, Russian Academy of Sciences, St. Petersburg, 194021 Russia

** e-mail: L.Ovsyannikova@pop.ioffe.rssi.ru*

Received September 23, 2003

Abstract—Analytical expressions for the electrostatic potential profile and the main parameters of a particle energy analyzer of a simple design with cylindrical electrodes are obtained. The regimes of analyzer operation with maximum energy dispersion in a wide range of the angular width of the field electrode are determined. The proposed energy analyzer can be successfully combined with the high-dispersion mass analyzer of the cylindrical mirror type developed previously and can be used for focusing a charged particle beam with respect to velocity. *© 2004 MAIK "Nauka/Interperiodica".*

We have analytically calculated the parameters of a two-electrode cylindrical electrostatic particle energy analyzer with the cross section schematically depicted in Fig. 1a. The beam of charged particles is injected and extracted via a slit in the grounded electrode. In a two-dimensional approximation, the electrostatic potential profile in this device is described by the function

$$\Phi(x) = \frac{V}{\pi}\left[\xi + \arctan\frac{(x-1)\sin\xi + y\cos\xi}{1-(x-1)\cos\xi + y\sin\xi} + \arctan\frac{(x-1)\sin\xi - y\cos\xi}{1-(x-1)\cos\xi - y\sin\xi}\right], \quad (1)$$

where V is the field electrode potential and ξ is the angular halfwidth of the field electrode (here and below, all coordinates and linear parameters are expressed in units of the cylinder radius r).

In the plane of dispersion of the analyzer ($x0z$), formula (1) simplifies to

$$\frac{\Phi(x)}{V} = \frac{2}{\pi}\arctan\left(\frac{x\tan(\xi/2)}{2-x}\right), \quad (2)$$

and expressions for the main parameters in the mirror regime of operation can be obtained in the form of integrals. In particular, a distance between the points of the particle entrance ($x = 0$) and exit from the field is

$$l = \frac{2\pi\sin(2\theta)}{\beta}\left\{\cot\frac{\xi}{2} - \int_0^{x_m} P(x)q(x)dx\right\}. \quad (3)$$

Here, $\beta = -V/\Phi_0$ is the analyzer gain, Φ_0 is the accelerating potential, θ is the entrance angle of the central trajectory, and x_m is the coordinate of the turning point of the trajectory. The latter coordinate is given by the formula

$$x_m = \frac{2}{1 + \cot\left(\frac{\pi\sin^2\theta}{2\beta}\right)\tan\frac{\xi}{2}}. \quad (4)$$

This expression indicates that the maximum beam injection angle (for which the trajectory touches the field electrode, so that $x_m = 2r$) is

$$\theta_m = \arcsin\sqrt{\beta} \quad (5)$$

irrespective of the angular width of this electrode.

Now, let us determine the shortest distances from the field boundary to the source (h) and detector (g) of charged particles, for which the first-order focusing with respect to the beam divergence angle α is provided in the dispersion plane (Fig. 1b). This condition can be

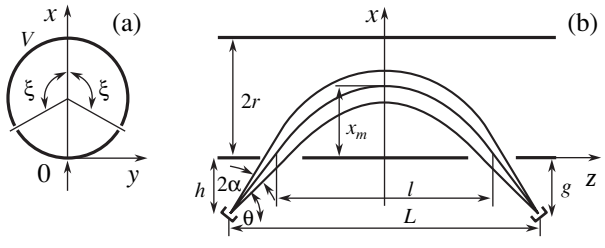

Fig. 1. Schematic diagrams of a particle energy analyzer with cylindrical electrodes: (a) cross section; (b) particle trajectories in the plane of dispersion (see the text for explanations).

1063-7850/04/3004-0275$26.00 © 2004 MAIK "Nauka/Interperiodica"

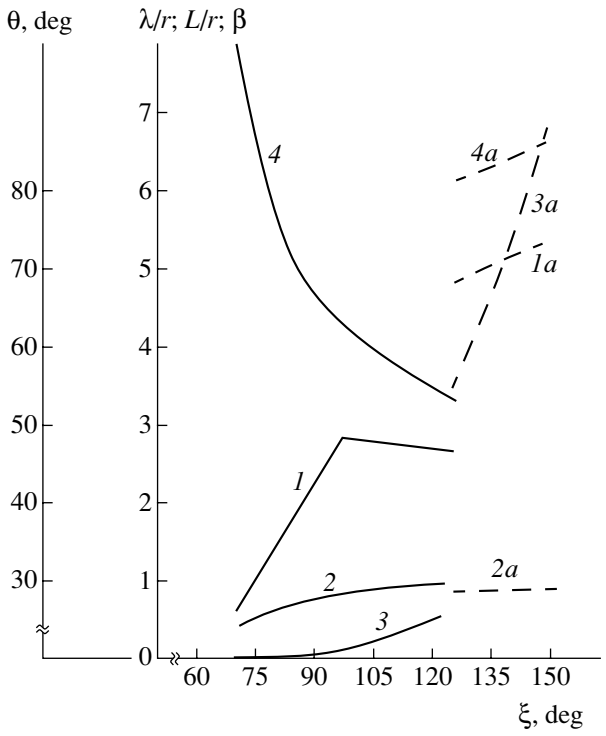

Fig. 2. Plots of the main parameters versus angular halfwidth of the field electrode for a cylindrical energy analyzer operating in the regime with maximum second-order focusing with respect to the beam divergence angle: (*1*, *1a*) central trajectory entrance angle θ; (*2*, *2a*) electrostatic field strength β; (*3*, *3a*) the sum of distances from the source and detector to the field boundary λ; (*4*, *4a*) analyzer base length *L*.

satisfied for a range of h and g values such that the sum $\lambda = h + g$ equals

$$\lambda = l\cos(2\theta)\tan\theta - \frac{2\pi\sin^2(2\theta)}{\beta} \times \int_0^{x_m} P(x)q(x)\left\{1 + \frac{\Phi(x)}{E_x q(x)\sin\xi} - \frac{\pi\Phi(x)q(x)}{V}\right\}dx, \quad (6)$$

where E_x is the electric field strength in the dispersion plane of the analyzer; the functions $P(x)$ and $q(x)$ are defined by the formulas

$$P(x) = \sqrt{1 + \frac{\Phi(x)}{\Phi_0\sin^2\theta}}, \quad q(x) = \frac{1 + \cos\xi - x}{\sin\xi}.$$

The energy analyzer base length (the distance between the source and the detector) is

$$L = l + \lambda\cot\theta. \quad (7)$$

For the first-order focusing, the main aberration term is determined by the second-order coefficient

$$C_2 = \frac{2}{\sin^2(2\theta)} \times \{l[2\cos^2\theta(1 - 8\cos^2\theta) - 1] + 2L(5\cos^2\theta - 1)\} + \frac{8\pi\cos^3\theta}{\beta\sin\theta}\int_0^{x_m} P(x)q(x)\left[2 - \frac{\pi\Phi^2(x)}{V^2}\left(\pi q^2(x) - \frac{4V}{E_x\sin\xi}\right)\right]dx. \quad (8)$$

For the analyzer under consideration (as well as for any mirror-type analyzer featuring the first-order focusing regime), the coefficient of linear dispersion with respect to the energy depends only on the base length and the entrance angle of the central trajectory [1]:

$$D = L/(2\cos^2\theta). \quad (9)$$

Using the above formulas, we have calculated the working parameters in the dispersion plane of a two-electrode cylindrical energy analyzer in a wide range of the angular width of the field electrode ($50° < \xi < 150°$). It is most interesting to determine operation regimes ensuring the second-order focusing with respect to the beam divergence angle. No such regimes exist for $\xi < 70°$.

Figure 2 presents a diagram of the main parameters of the energy analyzer operating in the regime with maximum possible energy dispersion. In the first branch ($\xi = 70°$–$125°$), each angle corresponds to a certain range of field strengths such that $C_2 = 0$. In this case, at a maximum possible analyzer gain, the entrance angle of the central trajectory is maximal, while the analyzer base length and the distances from the source and detector to the field boundary are minimal. Therefore, the linear dispersion with respect to the energy reaches a maximum. For these reasons, at any angular width of the field electrode, the regime of maximum analyzer gain in the first branch is optimum from the standpoint of maximum dispersion (Fig. 2, solid curves *1*–*4*). However, the absolute value of this dispersion is relatively small: $D = (4.8–3.5)r$. Moreover, in the region of small angular halfwidth ($\xi = 70°$–$80°$), the analyzer dimensions are large, $L = (8–6)r$, and the injection angles are small ($\theta = 25°$–$35°$). In addition, the beam focusing takes place at the field boundary, which is inconvenient from the standpoint of arrangement of the particle source and detector. Finally, the coefficient of the third-order spherical aberration determined from the slope of the $C_2 = f(\theta)$ curve at the point where $C_2 = 0$ is large: $C_3 = (65–20)r$. For these reasons, it is expedient to use analyzers with the angular halfwidths in the interval $\xi = 100°$–$120°$, where greater injection angles and shorter base length are combined with the residual aberrations reduced by two orders of magnitude: $C_3 = (0.76–0.13)r$.

In the second branch, corresponding to $\xi = 125°$–$150°$ (Fig. 2, dashed curves *1a*–*4a*), each angle also corresponds to a range of field strength in which $C_2 = 0$ and

the energy dispersion is maximum for a minimum analyzer gain. According to the universal formula (9), the energy dispersion is $D = (21.5–41.0)r$. However, the third-order aberrations are relatively large: $C_3 = (52–142)r$. Thus, in order to obtain a high energy resolution (characterized by the ratio D/C_3 for the point sources), it is most favorable to employ analyzers with $\xi = 100°–120°$.

It should be noted that the parameters calculated above for the analyzer under consideration are close to the analogous characteristics of a two-electrode analyzer with one electrode representing a part of a cylindrical surface and the other electrode being flat [2]. However, the analyzer with two cylindrical electrodes is favorably combined with the previously developed high-dispersion mass analyzer comprising a cylinder made of a magnetic material separated into four parts along the cylinder generatrix. Two opposite parts are the magnet poles with arbitrary angular widths, while the two others are screens occurring at a zero magnetic potential [3]. When a potential is applied to one of the screens (or simultaneously to the screen and the magnetic poles) and a beam is injected through the other screen, an electrostatic field of the type considered above is formed. This combined electromagnetic field can provide for the beam focusing with respect to velocity. In addition, the electrostatic component can be used to provide for a decrease (in the ideal case, full correction) of the second-order spherical aberration taking place in the case of a purely magnetic-field focusing.

REFERENCES

1. T. Ya. Fishkova, Zh. Tekh. Fiz. **57**, 1358 (1987) [Sov. Phys. Tech. Phys. **32**, 804 (1987)].
2. T. Ya. Fishkova and I. A. Korishch, Zh. Tekh. Fiz. **56**, 367 (1986) [Sov. Phys. Tech. Phys. **31**, 221 (1986)].
3. L. P. Ovsyannikova and T. Ya. Fishkova, Zh. Tekh. Fiz. **72** (10), 119 (2002) [Tech. Phys. **47**, 1321 (2002)].

Translated by P. Pozdeev

Technical Physics Letters, Vol. 30, No. 4, 2004, pp. 278–280. Translated from Pis'ma v Zhurnal Tekhnicheskoĭ Fiziki, Vol. 30, No. 7, 2004, pp. 42–47.

Multifractal Properties of Grain Structures in Sodium Niobate Based Binary Ceramics with Nonisostructural Components

V. V. Titov, L. A. Reznichenko, S. V. Titov, V. D. Komarov, and V. A. Akhnazarova

Institute of Physics, Rostov State University, Rostov-on-Don, Russia

e-mail: vtitov@uic.rnd.runnet.ru

Received October 13, 2003

Abstract—The process of grain structure formation and development in ferroelectric ceramics based on sodium noiobate are considered. Micrographs of the grain boundary regions are described in terms of multifractal parameters. Correlations between the multifractal and structural parameters of ferroelectric niobate ceramics are found. The process of secondary interrupted recrystallization has been studied. The results have been used for optimization of the technology of novel ferroelectric materials. *© 2004 MAIK "Nauka/Interperiodica".*

We have studied the formation and evolution of grain structure in the binary system $(1 - x)NaNbO_3$–$xCa_2Nb_2O_7$ ($0 \le x \le 1.0$), where $NaNbO_3$ is an antiferroelectric (AFE) compound with a perovskite structure [1] and $Ca_2Nb_2O_7$ is a ferroelectric (FE) compound with a stratified perovskite-like structure [2]. The interest in this system is related to the nonisostructural character of the components, which makes possible the formation of intermediate phases with unique electrical properties. The electrical and mechanical properties of ceramics are determined primarily by their microstructure (grain structure). In this context, we will consider the process of grain structure formation, which gives rise to the secondary interrupted recrystallization. This leads to anomalously rapid grain growth up to giant dimensions (above 100 μm), resulting in self-fracture of the samples.

The samples were prepared using conventional ceramic technology and by means of hot pressing. The microstructure was studied with an optical microscope (Neophot 21B) using specially prepared lapped sections subjected to thermal etching.

The grain structure of the samples was studied using the method of multifractal parametrization [3, 4]. According to this, the $f(\alpha)$ spectra and the D_q spectra of generalized dimensions [5, 6] were analyzed on the approximated black-and-white images obtained for the parts of micrographs of the sample grain structure. The calculations were performed for the cells coinciding with the grain boundaries revealed by thermal etching, which were assigned unit weights. Only the canonical spectra [3] obeying the condition $Dq_1 \ge Dq_2$ for $q_1 \le q_2$ were processed, so that $f(\alpha(q = 0))$ = maximum = D_0; $f(\alpha(q = 1)) = \alpha(q = 1) = D_1$; and $f(\alpha(q_1) \le f(\alpha(q_2))$ and $\alpha(q_1) \le \alpha(q_2)$ for $q_1 \ge q_2 \ge 0$. Here, q is a parameter appearing as the power in an expression for the cell weight used for the calculation of the generating function of measure [3–6].

The most informative variables for the quantitative description [3, 4] were the following parameters of the canonical spectra:

(i) Homogeneity parameter [3] $f_\infty = f(\alpha(q))$ for $q \gg 1$, which is a characteristic of the distribution of unit structural elements in the Euclidean space containing a given structure (in the calculations of $f(\alpha(q))$ for $q \gg 1$, we used $q = 40$).

(ii) Order parameter [3] $\Delta_\infty = D_1 - D_q$ for $q \gg 1$, which characterizes the degree of symmetry breakage in a given structure with respect to the multifractal transformation [4]. Here, D_1 (i.e., D_q for $q = 1$) is the value of information dimension [5, 6] (in the calculations of D_q for $q \gg 1$, we also used $q = 40$). In our case, the parameter Δ_∞ characterizes the degree of equilibrium (stability) of the grain structure, while the parameter f_∞ reflects the level of residual mechanical stresses arising in the course of recrystallization sintering of the ceramic material.

It was found that the microstructure of the $NaNbO_3$ ceramics is isometric (Fig. 1a), with a reduced diameter of the observed cubic sections varying from ~2 to 20 μm. In $Ca_2Nb_2O_7$ ceramics, the grains (with the length varying within 20–80 μm) have acicular shapes and are randomly oriented in space (Fig. 1b). We have determined the interval of compositions x ($0.125 \le x \le 0.2$) in which the microstructure of both types coexist (quasi-morphotropic region). It should be noted that acicular grains appear in a single phase (perovskite)

region extending up to $x = 0.2$ [7]. As x varies in the interval $0.2 \le x \le 1.0$, the system exhibits sequential crystallization of the structures corresponding to the empirical formula $A_nB_nO_{3n+2}$ with $n = 8$–4. Therefore, we may suggest that the perovskite region features the formation of clusters with stratified structures, the size and number of which increase on moving "deeper" into the system.

A comparison of the multifractal parameters determined in the interval of $0.1 \le x \le 0.2$ for selected regions with isotropic and acicular grains showed that, beginning with $x \ge 0.125$, the acicular type becomes more equilibrium. We have obtained nonmonotonic dependences of the Δ_∞ and f_∞ values on the content of $Ca_2Nb_2O_7$. The extrema in these dependences correlate with the boundaries of the regions of phase transformations in the system studied. Figure 2 presents the results of the multifractal analyses together with a fragment of the phase diagram of the $(1 - x)NaNbO_3$–$xCa_2Nb_2O_7$ system ($0 \le x \le 0.2$) [7], showing the following regions: (*1*) AFE; (*2*) AFE + FE; (*3*) FE; (*4*) paraelectric. In the phase diagram (Fig. 2), *R*(*M*4) denotes the orthorhombic phase with a fourfold monoclinic perovskite subcell; *R*(*M*2) is an orthorhombic phase with a double monoclinic perovskite subcell; *C*2 is a cubic phase with superstructure; and *C* is a cubic phase without superstructure.

An analysis of Fig. 2 shows that the minimum of f_∞ (and the maximum of Δ_∞) for $x \sim 0.05$ corresponds to an AFE–FE transition; the maximum of f_∞ (and the inflection on the Δ_∞ curve) at $x \sim 0.10$ reflects a transition to the two-phase region *R*(*M*2) + *C*2; the inflection on the f_∞ curve (and a minimum of Δ_∞) at $x \sim 0.125$ corresponds to a transition to the *C*2 phase; and the minimum of f_∞ (and a maximum of Δ_∞) at $x \sim 0.175$ reflects the transition to the *C* phase. In the region adjacent to $Ca_2Nb_2O_7$ ($0.7 \le x \le 1.0$), the extrema of f_∞ and Δ_∞ correspond to the sequential formation of stratified structures with the formula $A_nB_nO_{3n+2}$ with $n = 6$–4.

Thus, changes in the phase state of the system studied are reflected by variations of the multifractal parameters of homogeneity and order of the ceramic grain structure. It was also established that mutually consistent singularities in the behavior of the homogeneity (dips) and order (peaks) parameters precede two important states in the secondary interrupted recrystallization: the formation of giant grains and their merging into agglomerates. Therefore, the multifractal parameters can reveal changes in the grain structure not explicit from the standpoint of conventional characteristics, which provides a means of predicting and avoiding negative recrystallization processes, including those leading to critical changes in the mechanical properties of materials. Use of the multifractal approach for evaluation of the state of the microstruc-

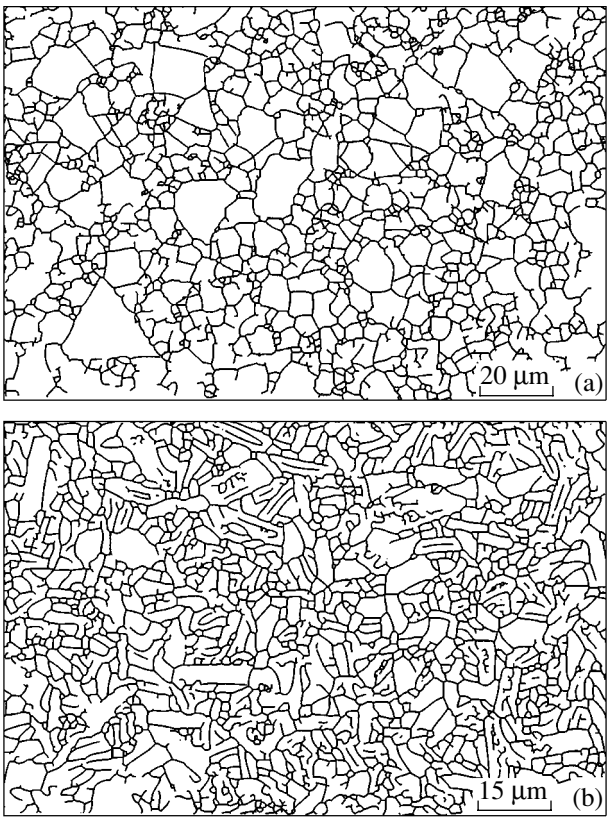

Fig. 1. Fragments of the approximated images of the grain structure of (a) $NaNbO_3$ and (b) $Ca_2Nb_2O_7$.

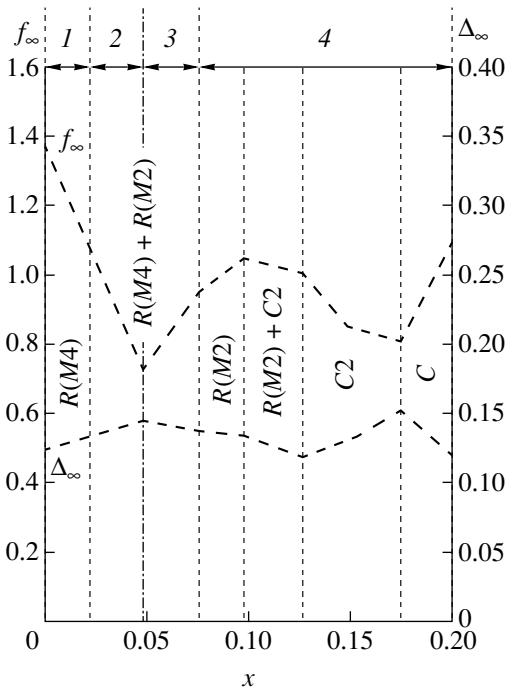

Fig. 2. Plots of the multifractal parameters f_∞ and Δ_∞ versus composition, combined with a fragment of the phase diagram of the $(1 - x)NaNbO_3$–$xCa_2Nb_2O_7$ system (see the text for explanations).

ture can be useful in simulating the properties and atomic design of advanced ferroelectric materials.

Acknowledgments. This study was supported by the Russian Foundation for Basic Research, project no. 02-02-17781.

REFERENCES

1. H. D. Megaw, Ferroelectrics **7**, 87 (1974).
2. J. K. Brandon and H. D. Megaw, Philos. Mag. **21** (169), 189 (1970).
3. G. V. Vstovsky, A. G. Kolmakov, and I. Zh. Bunin, *Introduction in Multi-Fractal Parametrization of Material Structures* (NITs "Regul. Khaot. Din.," Izhevsk, 2001) [in Russian].
4. G. V. Vstovsky, Found. Phys. **27**, 1413 (1997).
5. J. Feder, *Fractals* (Plenum, New York, 1988; Mir, Moscow, 1991).
6. T. C. Halsey, M. H. Jensen, L. P. Kadanoff, *et al.*, Phys. Rev. A **33**, 1141 (1986).
7. L. A. Reznichenko, O. N. Razumovskaya, L. A. Shilkina, *et al.*, in *Proceedings of the International Symposium on Order, Disorder, and Oxide Properties, Sochi, 2002*, Vol. 2, pp. 70–80.

Translated by P. Pozdeev

Technical Physics Letters, Vol. 30, No. 4, 2004, pp. 281–283. Translated from Pis'ma v Zhurnal Tekhnicheskoĭ Fiziki, Vol. 30, No. 7, 2004, pp. 48–53.

The Antimicrobial Action of High-Power Electric Discharge in Water. Part 2. Experimental Results

K. V. Vilkov, A. L. Grigor'ev, Yu. A. Nagel', and I. V. Uvarova

Keldysh Research Center, State Unitary Enterprise, Moscow, Russia

e-mail: kerc@elnet.msk.ru

Received March 18, 2003; in final form, September 11, 2003

Abstract—We have experimentally studied the antimicrobial action of high-power pulsed discharge in model solutions, natural water, and waste waters inoculated with *E. coli* 1257 and MS-2 coli-phage species. It is found that the efficiency of the antimicrobial treatment decreases in the presence of suspended macroscopic particles. A specific energy consumption of 0.02–0.04 kW h/m^3 has been achieved. © *2004 MAIK "Nauka/Interperiodica".*

Introduction. The energy efficiency of the antimicrobial treatment of water by periodic pulsed discharges with a pulse energy of 1–20 J was studied in [1–4]. It was established that the discharge action had a local character: the loss of test microbes upon multiply repeated discharges was observed only in a region adjacent to the discharge channel. According to the published data, the specific energy consumption amounted to 0.5–1.0 kW h/m^3.

The antimicrobial treatment of a significantly greater volume of water can be provided by high-power pulsed discharges with energies on the order of several kilojoules per pulse. In comparison to the aforementioned periodic pulse trains, the energy consumption may decrease because the number of discharges can be reduced to one, while the volume of water treated in a single cycle can be increased. In addition, a decrease in the number of charge–discharge cycles increases the working life of the capacitive energy store. A significant disadvantage of the latter approach is related to a considerable increase in the level of thermomechanical loads upon the electric-discharge setup. Accommodation of these loads requires finding the optimum design and technological solutions.

Experimental setup. The experiments were performed in a model chamber comprising a steel cylinder with thick walls and volume of ~10 dm^3, connected to four side channels with a 90° angle between channel axes (Fig. 1). The channels were made of cone-shaped parts jointed together. This design allowed the channel length to be varied from 0.24 to 2 m and the amount of aqueous medium to be reduced to 10–50 dm^3. Since the shock waves entered channels via holes (diaphragms), the pattern of the shock wave propagation in the model chamber differs from that in an infinite medium. According to [5], the difference is most pronounced in the region $0.5 < r/r_0 < 1.5$, where r_0 is the distance from a diaphragm to the shock wave source.

The electric discharge source was introduced into the chamber via an insulating flange on the top lid and connected to a capacitive energy store. The capacitor bank had a total capacitance of 72 μF, was charged to 24.6 kV, and released an energy of 21.5 kJ per pulse. The pressure was measured by manganin sensors. The integral pressure pulse was evaluated using crash type devices (comprising plungers with needles and a set of paper disks in cylindrical cases). Figure 1 shows the results of measurements of the maximum pressure at the shock wave front plotted in the dimensionless coordinates of p/p_c versus r/l, where p_c is the effective pressure calculated for an effective adiabate index of 1.31–1.45 in the discharge channel [6], r is the distance from electrode axis to the point of measurements, and l is the interelectrode distance. To within the experimental error, our results satisfactorily agree with the data reported for axisymmetric chambers [6].

Results and discussion. Figure 2 presents generalized data on the efficiency of antimicrobial action of high-power discharges on model aqueous media (physiological solution, dechlorinated tap water, and boiled water), natural water, and waste water inoculated with *E. coli* 1257 and MS-2 coli-phage species. The results of the antimicrobial tests are plotted in the coordinates of microbe concentration versus specific energy consumption.[1] The specific energy consumption was calculated as the ratio of consumed energy to the volume of water within an ovaloid formed by the revolution of an isobar (the line of equal pressures on the shock wave

[1] Comparative microbiological analyses of the initial and treated media were performed by the research group headed by Dr. N.A. Rusanova at the Research Institute of Water Supply and Purification.

1063-7850/04/3004-0281$26.00 © 2004 MAIK "Nauka/Interperiodica"

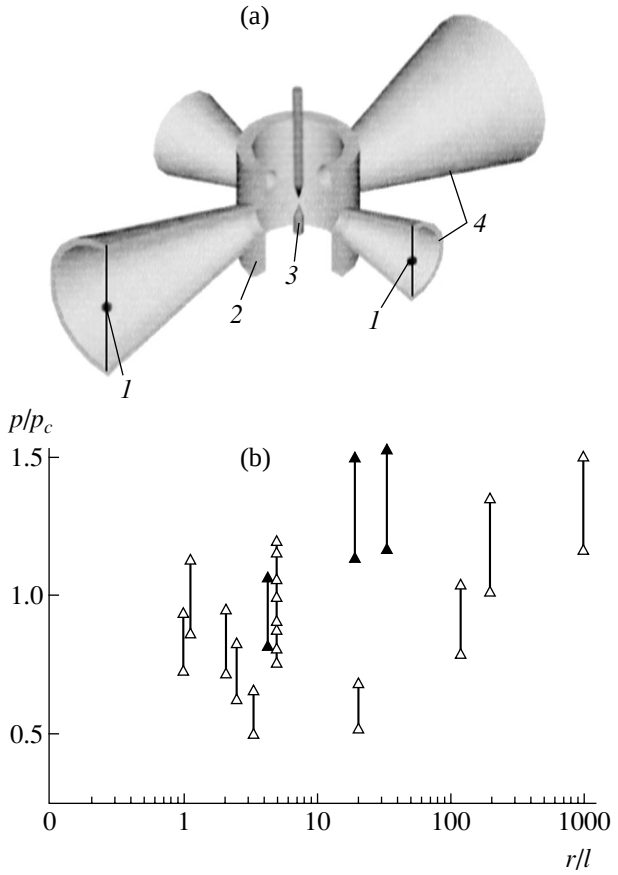

Fig. 1. (a) Schematic diagram of the model chamber and (b) comparative data on the maximum pressure at the shock wave front: (*1*) pressure sensors; (*2*) cylindrical vessel; (*3*) electric discharge gap; (*4*) cone-shaped channels; (▲) data of this study; (△) data for axisymmetric chambers [6].

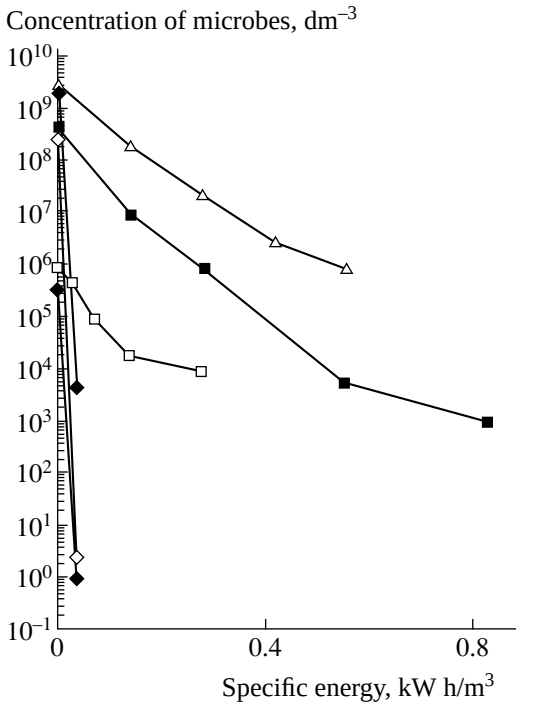

Fig. 2. Data on the efficiency of disinfection by pulsed discharges: (◇, □, △) *E. coli* 1257; (◆, ■) MS-2 coli-phage; (△) data from [1, 2]; (□, ■) data from [3, 4]; (◇, ◆) this study.

front) around the discharge axis in a hypothetical infinite medium. The isobar was determined by an equation proposed in [6]; the long axis of the ovaloid was taken equal to the distance R from the model chamber axis to the channel end. The value of R for which a single discharge provided for a decrease in the microbe concentration below 10^3 dm^{-3} was about 0.6 m. For comparison, Fig. 2 shows the data published for periodic pulsed discharges [1–4].

According to the results of our measurements, the pressure jump produced by arrival of a shock wave at the internal wall of a blunt channel end for $R \cong 0.6$ m was 10^2 MPa (averaged over five experiments), which corresponded to a pressure jump of $\Delta p \sim 0.5 \times 10^2$ MPa at the incident wave front [7]. It should be noted that this value is qualitatively consistent with theoretical predictions, according to which the pressure jump at a shock wave front required for the microbe destruction is $\Delta p > (0.6–1.35) \times 10^2$ MPa.

The obtained results indicate that the experimental setup parameters provided for a regime in which a single discharge led to the destruction of test microbes in a sufficiently large volume of an aqueous medium. This accounts for a significant decrease in the specific energy consumption for the antimicrobial treatment compared to the level achieved using the regime of low-energy periodic pulsed discharges (see [1–4]).

In the course of experiments, we observed a decrease in the efficiency of the antimicrobial treatment of water containing suspended organic particles. For example, the specific energy consumption for the disinfection of a waste water (containing suspended macroscopic particles at a weight fraction of $\alpha \sim 5 \times 10^{-5}$) was about twice that for waste water with $\alpha \cong 0$. Calculations showed that the observed difference could not be explained by the enhanced damping of shock waves of by the screening of microbes by suspended macroscopic particles. However, taking into account the small characteristic time required for the microbes to meet a particle (estimated at ~20 min), we may suggest that most microbes occur on or inside such particles, which leads to an increase in the energy required for their destruction.

Conclusions. We have experimentally studied the efficiency of antimicrobial action of high-power pulsed discharge in model solutions, natural (tap) water, and waste waters inoculated with *E. coli* 1257 and MS-2 coli-phage species. It is established that a single discharge suffices for decreasing the microbe concentration to a required level (below 10^3 dm^{-3}) provided that

the pressure drop at the shock wave front is not less than 50 MPa. A specific energy consumption of 0.02–0.04 kW h/m^3 has been achieved.

REFERENCES

1. V. L. Goryachev, F. G. Rutberg, and V. N. Fedyukovich, Teplofiz. Vys. Temp. **34**, 757 (1996).
2. V. L. Goryachev, F. G. Rutberg, and V. N. Fedyukovich, Izv. Akad. Nauk, Énerg. **34**, 40 (1998).
3. A. V. Avchinnikov, A. E. Nedachin, Yu. A. Rakhmanin, *et al.*, Med. Konsul'tatsiya, No. 1, 9 (1996).
4. A. V. Avchinnikov, Vestn. Smolensk. Med. Akad., No. 3, 75 (2001).
5. G. A. Atanov and L. A. Kunitsyn, Zh. Vychisl. Mat. Mat. Fiz. **15**, 1069 (1975).
6. E. V. Krivitskiĭ and V. V. Shamko, *Transient Processes in High-Voltage Discharge in Water* (Naukova Dumka, Kiev, 1979) [in Russian].
7. Yu. S. Yakovlev, *Hydrodynamics of Explosion* (Sudpromgiz, Leningrad, 1961) [in Russian].

Translated by P. Pozdeev

Technical Physics Letters, Vol. 30, No. 4, 2004, pp. 284–286. Translated from Pis'ma v Zhurnal Tekhnicheskoĭ Fiziki, Vol. 30, No. 7, 2004, pp. 54–59.

Spin Polarized Electron Spectroscopy of Thin Vanadium Films on a (110)$FeNi_3$ Surface

V. N. Petrov[a,*], A. S. Kamochkin[a], and V. M. Uzdin[b]

[a] *St. Petersburg State Technical University, St. Petersburg, 195251 Russia*

[b] *St. Petersburg State University, St. Petersburg, 199164 Russia*

* *e-mail: Petrov@tuexph.stu.neva.ru*

Received October 13, 2003

Abstract—The magnetic properties of vanadium films on a single crystal $FeNi_3$ surface have been studied by Auger electron spectroscopy with spin resolution. It is established that the films exhibit antiferromagnetic ordering relative to the substrate. The induced magnetic moment of a two monolayer thick vanadium film is estimated at ~$0.35\mu_B$. Vanadium deposition does not lead to a decrease in magnetization of the iron sublattice of $FeNi_3$. © *2004 MAIK "Nauka/Interperiodica".*

In recent years, much attention has been devoted to the magnetic properties of metal surfaces, interfacial layers, and superlattices. Such low-dimensional structures exhibit new basic laws of magnetism and provide a basis for the creation of novel electronic devices for commercial applications. Of special interest are the interfaces between ferromagnetic and nonmagnetic metals, the properties of which account for the interlayer magnetic exchange interaction and determine the magnetoresistance of multilayer structures. Convenient model systems for the investigation of such structures are offered by superlattices with vanadium playing the role of a nonmagnetic metal.

By incorporating hydrogen into a thin vanadium layer, it is possible to increase the crystal lattice parameter within 10% in the direction perpendicular to the superlattice plane. In this way, we can provide conditions for a reversible transition from antiferromagnetic (AFM) to ferromagnetic (FM) exchange coupling between layers and vice versa controlled by hydrogen pressure [1]. Using this approach, the passage from three-dimensional to quasi-two-dimensional magnetism can be realized and studied in experiment [2]. Information about the chemical and magnetic structure of the interface is of principal significance for the description of this transition.

Vanadium is a paramagnetic metal. However, vanadium atoms occurring at the interface with a ferromagnet such as iron may acquire the induced magnetic moment, the magnitude of which depends on the character of mixing in the boundary layer [3]. Calculations performed for thin vanadium films on iron showed that the induced moment can be rather significant, especially in a monolayer thick film where the *d*-electron band of vanadium exhibits narrowing as a result of decrease in the coordination number of near-surface atoms [4]. When the film thickness exceeds two monolayers, the competition between antiferromagnetic V–V and V–Fe interactions strongly suppresses the magnetic moments everywhere except for the interfacial atomic layer. The existence of an induced magnetic moment on vanadium atoms has been confirmed in experiment [5].

It should be noted that most calculations of the magnetic structure of such systems were performed under the assumption that the interfacial layer was one to three monolayers thick. In experiment, such a thin interlayer is very difficult to obtain. Additional problems are related to the control of atomic intermixing and determination of the component concentration profiles formed in the course of epitaxial growth.

Below, we report on the results of using the method of Auger electron spectroscopy (AES) with spin resolution for the investigations of thin vanadium films deposited onto a (110) face of an $FeNi_3$ single crystal.

The experiments were performed with a spin-polarized electron spectrometer developed by the Surface Magnetism Group at St. Petersburg State Technical University. The instrument comprises an original electron energy analyzer of the cylindrical mirror type combined with a compact electron spin polarimeter implementing the classical Mott scheme [6–8].

A (110)-oriented $FeNi_3$ single crystal had the shape of a square frame with the sides oriented along the [111] easy axes. The crystal was magnetized to saturation by a pulse of electric current passed through a coil of seven turns wound around one side of the frame. Vanadium films were prepared by thermal evaporation of the metal in vacuum followed by deposition onto a clean surface of the single crystal substrate at room temperature. The residual pressure in the vacuum chamber was on the level of 5×10^{-9} Torr.

1063-7850/04/3004-0284$26.00 © 2004 MAIK "Nauka/Interperiodica"

The sample films on the single crystal substrate were studied by measuring the spectra of secondary (Auger) electrons with spin resolution. The spin polarization of electrons was determined as $P = (N^{\uparrow} - N^{\downarrow})/(N^{\uparrow} + N^{\downarrow})$, where $N^{\uparrow}$ ($N^{\downarrow}$) is the number of electrons with the magnetic moments oriented parallel (antiparallel) to the direction of magnetization in $FeNi_3$.

The sample film thicknesses were determined from data on the intensities of Auger electron signals from Ni and V measured during deposition. The experimental AES peak intensities obeyed the exponential law, which allowed the absolute thickness of a vanadium film to be determined provided that the mean free path of electrons with the energies corresponding to these peaks are known [9]. The values of film thicknesses determined from the analysis of intensities of the AES peaks of Ni and V were in good quantitative agreement (the difference not exceeding 5%).

However, the rate of decrease in the low-energy peak amplitude of Fe and Ni in the course of vanadium deposition did not agree with a simple model assuming the formation of a homogeneous film of V atoms on a flat $FeNi_3$ substrate. Since the mean free path of low-energy Auger electrons is about half that of the high-energy ones, the amplitude of the former AES peaks was expected to decrease with the thickness of the vanadium layer at a much greater rate. The experimental fact that the amplitude of the low-energy AES signals of Fe and Ni decreased with increasing vanadium film thickness even slower than that of the high-energy signals of these elements indicated that either the film thickness was inhomogeneous or a significant amount of Fe and Ni atoms was dissolved in the vanadium deposit. The rate of decrease of the low-energy Fe and Ni peak intensity with increasing vanadium film thickness allowed the characteristic roughness height to be estimated at about 10 Å.

The spin-resolved AES peaks of V and Fe were measured for films with a thickness of 1, 2, and 12 monolayers (MLs). The spin polarization of the AES signal from Ni was not studied, since it was much less pronounced than that of the signal from Fe. For the 1-ML-thick film of vanadium, the AES peak of vanadium did not exhibit spin splitting (to within the experimental error). Figure 1 shows the typical spin-resolved AES peak of vanadium (upon background subtraction) for a 2-ML-thick film. This signal corresponds to the $L_3M_{23}M_{45}$ transition involving a single 3*d* electron. To the first approximation, the peak shape can be considered as determined by the density of states of *d* electrons. Using this assumption, the effective magnetization can be estimated from the polarization data.

Ignoring (i) the influence of a hole (2*p* changing to 3*p*) present in the V atom on the density of states in the valence band and (ii) the contribution of Auger processes with spin reversal, we can estimate the magnetic moment on a V atom as

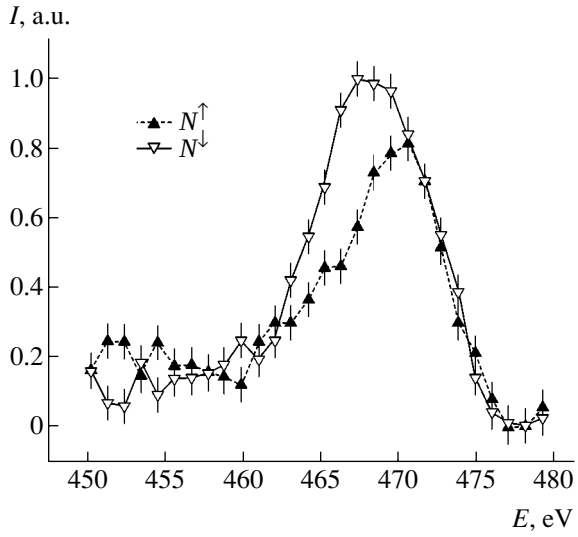

Fig. 1. The typical spin-resolved AES signal of vanadium from a 2-ML-thick film on a (110)$FeNi_3$ single crystal surface.

$$M = N\frac{S^{\uparrow} - S^{\downarrow}}{S^{\uparrow} + S^{\downarrow}}\mu_B,$$

where $S^{\uparrow}$ and $S^{\downarrow}$ are the areas under the Auger peaks of electrons with the corresponding spin projections, *N* is the number of valence electrons per atom, and μ_B is the Bohr magneton. This estimate can be refined by correcting the peak shape with allowance for the electron–electron correlations, but even in that case, quantitative interpretation of the Auger spectra requires introducing some fitting parameters [10, 11].

The polarization of the AES peak of vanadium determined as described above has proved to be negative, which implies that the intensity of the Auger peak of electrons with spin down is greater than that for spin up. This is indicative of the AFM ordering of the vanadium film relative to the substrate. Estimates gave the magnetic moment of a vanadium atom about $0.35\mu_B$. A weak polarization was also observed for a 12-ML-thick film, where the moment on a vanadium atom was less than $0.1\mu_B$. The presence of induced magnetic moment at such a long distance from the interface confirms the conclusion about interface roughness or the presence of a sufficiently large amount of Fe and Ni atoms incorporated into the vanadium film.

Figure 2 presents the Auger signal of iron (also corresponding to the $L_3M_{23}M_{45}$ electron transition) measured after deposition of a 2-ML-thick film of vanadium. An analysis of the experimental data showed that the magnetization of the iron sublattice did not decrease (to within the experimental error) upon deposition of

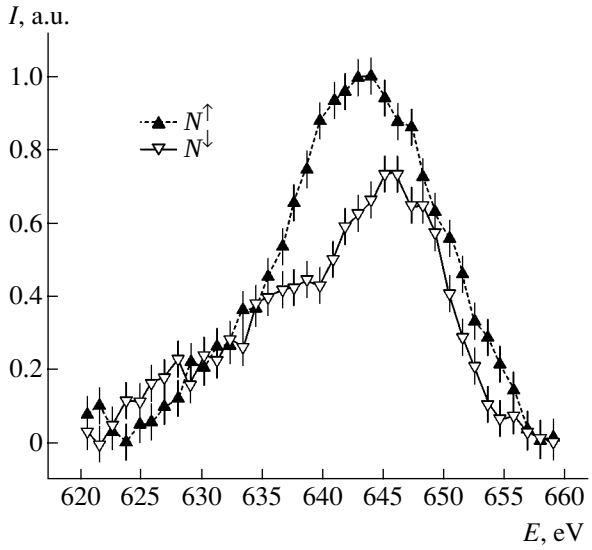

Fig. 2. The typical spin-resolved AES peak of iron for a (110)$FeNi_3$ single crystal covered with 2-ML-thick vanadium film.

this vanadium layer. Thus, coating a substrate crystal with a thin layer of vanadium does reduce the magnetization of near-surface iron atoms. After deposition of a 12-ML-thick vanadium film, the total intensity of the AES peak of Fe was small, which hindered detailed analysis with spin resolution.

Acknowledgments. This study was supported in part by the INTAS Foundation (grant no. 01-0386) and the Ministry of Education of the Russian Federation (project no. E02-3.4-255).

REFERENCES

1. B. Hjörvarsson, J. A. Dura, P. Isberg, *et al.*, Phys. Rev. Lett. **79**, 901 (1997).
2. V. Leiner, K. Westerholt, A. M. Blixt, *et al.*, Phys. Rev. Lett. **91**, 037202 (2003).
3. V. Uzdin, K. Westerholt, H. Zabel, and B. Hjörvarsson, Phys. Rev. B **68**, 214407 (2003).
4. D. Spisak and J. Hafner, Phys. Rev. B **61**, 4160 (2000).
5. M. M. Schwickert, R. Coehoorn, M. A. Tomaz, *et al.*, Phys. Rev. B **57**, 13681 (1998).
6. V. N. Petrov and A. S. Kamochkin, Rev. Sci. Instrum. (in press).
7. V. N. Petrov, M. Landolt, M. S. Galaktionov, *et al.*, Rev. Sci. Instrum. **68**, 4385 (1997).
8. V. N. Petrov, V. V. Grebenshikov, B. D. Grachev, *et al.*, Rev. Sci. Instrum. **74**, 1278 (2003).
9. M. D. Seah and W. A. Dench, Surf. Interface Anal. **1**, 1 (1979).
10. K. Schröder, E. Kisker, and A. Bringer, Solid State Commun. **55**, 377 (1985).
11. B. Sinkovic, E. Shekel, and S. L. Hulbert, Phys. Rev. B **52**, R15703 (1995).

Translated by P. Pozdeev

Technical Physics Letters, Vol. 30, No. 4, 2004, pp. 287–290. Translated from Pis'ma v Zhurnal Tekhnicheskoĭ Fiziki, Vol. 30, No. 7, 2004, pp. 60–68.

Statistical Modeling of the Ion–Plasma Sputter Deposition of Thin $YBa_2Cu_3O_{7-x}$ High-Temperature Superconductor Films

V. A. Volpyas, S. V. Razumov, A. V. Tumarkin, and A. B. Kozyrev

St. Petersburg State Electrotechnical University, St. Petersburg, Russia

e-mail: thinfilm@eltech.ru

Revised manuscript received October 15, 2003

Abstract—A model of the process of thin multicomponent film deposition by ion–plasma sputtering of amorphous and polycrystalline targets has been developed. Using this model, the film deposition rates and the film thickness homogeneity over the substrate have been evaluated for thin films of high-temperature superconductors based on $YBa_2Cu_3O_{7-x}$ (YBCO) ceramics. A comparison of the results of numerical simulations based on the proposed model and the experimental data on the YBCO film deposition rates showed that the model provides for a sufficiently correct description of the ion–plasma sputter deposition process. The results were used for optimization of the technology of ion–plasma sputter deposition of thin multicomponent films. The model of the deposition process is applicable in the range of sputter ion beam energies up to 1–3 keV, which is of interest for many basic problems and technological applications involving the process of ion and ion–plasma sputtering of multicomponent materials. © *2004 MAIK "Nauka/Interperiodica".*

Processes involved in the growth of high-temperature superconductor films have been extensively studied [1–4]. One of the most effective methods used for obtaining thin-film structures with preset physical properties is offered by the ion–plasma sputter deposition process [5]. A significant difficulty encountered in the implementation of the technology of high-quality films is related to a poor reproducibility of stoichiometry, phase composition, and properties depending on the variable parameters of the deposition regime.

The process of obtaining films using the method of ion–plasma sputter deposition can be conditionally divided into three main stages:

(i) the interaction of ions and atoms of the gas discharge plasma with a multicomponent target and the formation of a flow of sputtered atoms in the gas phase;

(ii) the transport of sputtered atoms via the gas phase in the drift space between the target and a substrate;

(iii) the synthesis of a multicomponent material and the film formation and growth on the substrate.

The first two stages determine the deposition rate, the homogeneity of the film thickness, and the stoichiometry of thin films of multicomponent materials. The synthesis and film formation on a substrate are determined by the atomic composition and structure of the substrate material and by the substrate temperature. Therefore, statistical modeling of the process of ion sputtering of a multicomponent target and the transport of sputtered atoms via the gas phase in the target–substrate drift space is necessary and sufficient for optimization of the deposition rate, the homogeneity of the film thickness, and the stoichiometry of thin films of multicomponent materials obtained by the ion–plasma sputter deposition technique.

Let us consider the first stage in the process of ion–plasma sputter deposition: the interaction of ions and atoms of the gas discharge plasma with a multicomponent target and the formation of a flow of sputtered atoms. According to modern notions of the interactions leading to ion sputtering, each ion penetrating into the target material gives rise to a cascade of binary elastic collisions of displaced atoms, in which the atoms exchange their energies and momenta. The collision cascade may result in the transfer of a sufficiently high energy and momentum to a surface atom, which will allow this atom to overcome forces binding it to the target surface.

In recent years, the progress in microelectronics has posed the problem of studying the ion and ion–plasma sputtering of multicomponent materials. For such materials, the sputtering process cannot be characterized by simple sputtering coefficients, because a depleted near-surface layer is formed in the target. In this case, a parameter adequately characterizing the efficiency of sputtering of a multicomponent material is the rate of target sputtering and its variation with depth of the depleted near-surface layer or with the target mass. In addition, the process of ion–plasma sputtering of a multicomponent material alters the initial stoichiometry of the near-surface layer of the target. On the one hand, this changes the composition of the flow of sputtered atoms. On the other hand, a change in the composition and properties (in particular, the electron–ion emission coefficient) of the target surface changes the integral characteristics of the gas discharge. In the course of sputtering, the process conditions exhibit sta-

1063-7850/04/3004-0287$26.00 © 2004 MAIK "Nauka/Interperiodica"

bilization and, provided that some technological parameters (such as the discharge voltage and the working gas composition and pressure) are maintained constant, a steady-state regime of target sputtering is established.

Now, let us consider in more detail the form and algorithm of the proposed regression model of the ion–atom collision cascade [6]. Using the method of Monte Carlo simulation adopted to the process of particle scattering in the course of ion–atom collisions, we simulate the trajectory of a bombarding ion in the target and calculate the momentum transfer to target atoms as a result of the ion–atom pair collisions. By the same token, we simulate the trajectories of the primary target atoms of various types displaced due to collisions with the bombarding ion and calculate the corresponding energy losses in each atom–atom pair collision with the secondary displaced atoms of the target.

The trajectories of the displaced target atoms in various branches of the primary collision cascade are simulated unless either the energy reduced as a result of sequential atom–atom pair collisions will become lower than the binding energy of atoms of the corresponding type or the trajectory will cross the target surface. The ratio of the number of displaced atoms, whose trajectories cross the target surface in a simulated branch of the collision cascade, to the total number of bombarding ions determines the probability for the target atoms to escape from the surface. The escape probability depends on the mass, atomic number, and initial energy of the bombarding ion and on the masses, atomic numbers, binding energies, and concentrations of various component atoms of the solid target.

The possibility of simulating the trajectories of subsequent branches in the cascade of displaced atoms is limited by the computational facilities. However, the laws established using simulations of the ion–atom and primary atom–atom pair collision branches of the cascade can be expanded by means of regression analysis to describe the development of all subsequent atom–atom pair collision branches in the cascade of displaced atoms. Obviously, the branches in the cascade of primary atoms displaced under the action of bombarding ions include a greater number of collisions and involve greater initial energies than the subsequent branches in the cascade of atoms displaced due to atom–atom pair collisions. Therefore, the probability of escape from the target surface for atoms in the subsequent branches of the atomic collision cascade (i.e., the probability for the atomic trajectories to cross the target surface) will be smaller compared to the probability of escape for the target atoms displaced in the primary collisions with bombarding ions. The lower the initial energy (and, hence, the number of atom–atom pair collisions) in subsequent branches of the cascade of atomic displacements, the smaller the contribution of these branches to the yield of displaced atoms from the target surface.

For multicomponent targets, variation of the selective rate of ion sputtering of the jth component in depth of the target is determined by the relation

$$V_j = \frac{dx}{dt} = \frac{M_j P_j}{N_a q_i \rho_j} j_i,$$

where M_j and ρ_j are the atomic mass and density of the jth component; N_a is the Avogadro number; q_i is the charge of a bombarding ion; j_i is the ion current density; and P_j is the probability for atoms of the jth component to escape from the target surface under the action of bombarding ions. In multicomponent targets, the total rate of sputtering V_i is determined by the inertia of sputtering of a component with a minimum selective sputtering rate V_{ij}. As can be seen from the above formula, the main difficulty in determining the rate of sputtering for multicomponent targets is related to calculation of the escape probability P_j for atoms of the jth component. Indeed, the parameter M_j/ρ_j is determined by the experimental conditions, while the ion current density j_i can be measured directly.

Now, let us proceed to considering peculiarities of the second stage of the ion–plasma sputter deposition process: the transport of sputtered atoms via the gas phase in target–substrate drift space. The existing models of this transport [7] consider the transfer process from the standpoint of thermalization of particles and their diffusion and do not provide a strict description of the distribution of spatial densities, atomic flux intensities, and particle velocities in the interelectrode space. Variations in the elastic scattering cross sections and the scattering angles depending on the relative velocities of interacting particles complicates the description of the transport process within the framework of the classical theory of scattering. For this reason, the method of Monte Carlo simulations offers the main approach to investigation of the transport of sputtered atoms. Simulations (numerical experiments) of the transfer of particles describe a multistage process involving the escape of sputtered atoms from a target, their scattering on atoms of the working gas, and establishment of a diffusion regime [8]. The complexity of calculations involved in numerical simulations of the scattering processes by the Monte Carlo method depends primarily on the choice of the atomic interaction potential. It is necessary to compromise between realistic physical description of the interaction processes and sufficiently simple computational procedure to be used for numerical simulations.

Previously, there were attempts to describe the process of elastic scattering of atomic particles using a procedure of fitting of an approximate interaction potential to the real one for a certain distance between particles accounting for the maximum contribution to the scattering process. However, practically all the proposed approximate interaction potentials work poorly at large aiming parameters, leading to overstated values of the

energy transferred in the course of elastic scattering of atomic particles. We have developed a model of quasi-hard spheres [9], which allows the elastic scattering of atomic particles to be simulated using various interaction potentials, while retaining relatively high computation speeds achieved for simulations using the conventional hard model of hard spheres. The procedure proposed for the simulation of elastic scattering restricts the region of large aiming parameters for thermal energies of the interacting particles to their gaskinetic dimensions. For greater energies of colliding particles, the region of large aiming parameters corresponds to very small scattering angles and transferred energies and, hence, does not significantly contribute to the scattering process.

Using the proposed algorithm of simulation of the transport of sputtered atoms via the gas phase in the target–substrate drift space [10], it is possible to evaluate the energy characteristics and spatial distributions of sputtered atoms and determine the density and stoichiometry of particle flows in any section of the target–substrate drift space for the given technological parameters of the ion–plasma sputter deposition process.

In order to check the adequacy of the proposed model of the ion–plasma sputter deposition process, we have used this model for optimization of the technology of thin films of high-temperature superconductors based on $YBa_2Cu_3O_{7-x}$ (YBCO) ceramics [5]. For this purpose, we have studied the film deposition rates and the homogeneity of the film thickness as functions of the working gas (oxygen) pressure for a given system geometry and a preset gas discharge power. The homogeneity of the film thickness over the substrate is determined primarily by the flow of atoms of the heaviest component—Ba atoms—which are thermalized at a higher pressure than the relatively light Y and Cu atoms. Using the results of numerical simulations, we have compared the intensities of the flux of Ba atoms (most difficultly sputtered component) at the center of the substrate holder, $j_{Ba}(0)$, and in the zone of target sputtering, $j_{Ba}(R)$, where R is the distance from the substrate holder center to the sputtering zone center. The sputtering zone comprised a 15-mm-wide ring with an outer diameter of 53 mm.

The results of numerical simulations based on the proposed model of the ion–plasma sputter deposition process are presented in Fig. 1, showing the intensity of the flux of Ba atoms in the substrate plane as a function of the working gas pressure. As can be seen, the relative intensity of the flux of Ba atoms to the substrate surface under the target erosion zone is virtually the same as that at the center for a working gas pressure above 100 Pa and does not change with further increase in the pressure. On the other hand, an increase in the working gas pressure is accompanied by a decrease in the rate of delivery of the component atoms to the target surface and in the film growth velocity. These results allow the optimum working gas pressure to be chosen so as to provide for the formation of films with homogeneous thicknesses at a sufficiently high growth rate.

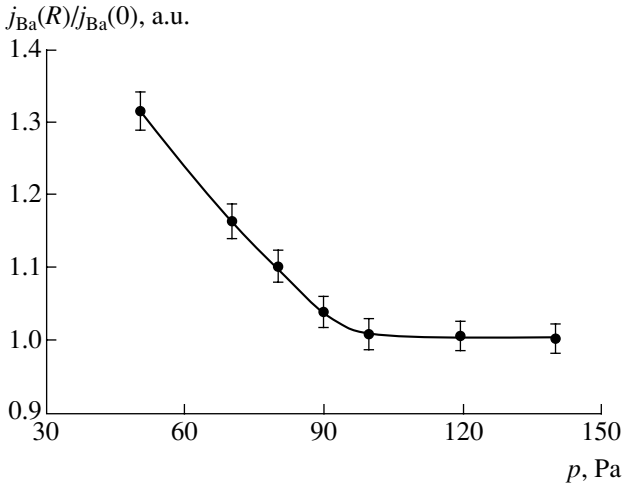

Fig. 1. Effect of the working gas pressure on the homogeneity of the flux of Ba atoms over the substrate holder radius.

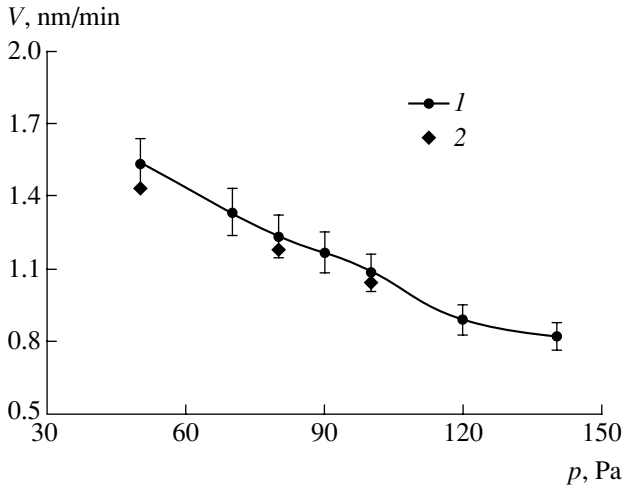

Fig. 2. A comparison of (*1*) the rate of delivery of a sputtered target material to the substrate surface (simulation results) and (*2*) the YBCO film growth velocity (experimental data) as functions of the working gas pressure.

Using the results of simulations, we have determined the intensities of atomic fluxes of the target components in the substrate plane. The rates of delivery of the sputtered material to the substrate surface are conveniently expressed in units of nm/min, which corresponds to the film growth velocity on a substrate at an adsorption coefficient of unity. This provides for a convenient comparison of the results of numerical simulations of the sputtering process and experimental determinations of the film growth velocity. The corresponding data for various working gas pressures are presented in Fig. 2. As can be seen from these data, the technological process parameters were selected so that the rates of delivery of the target material to the substrate surface (determined by simulations based on the

proposed model of the ion–plasma sputter deposition process) coincide to within 10% with the experimentally measured growth velocities for YBCO films. Even at rather high working gas pressures, there is no significant re-evaporation of deposited atoms from the substrate surface. Atoms not incorporated immediately into the crystal structure of a growing YBCO film are involved in the secondary nucleation and thus built in the film. An increase in the rate of material delivery to the substrate leads to a decrease in the crystal structure perfection of the growing film and to a reduction in the crystal grain size. Therefore, the rate of the sputtered material delivery to the substrate must correspond to the rate of incorporation of atoms into the structure of the growing film. A disbalance of these rates disturbs the process of atomic assembly and gives rise to disorder in the crystal structure of the deposit.

Thus, we have demonstrated that numerical simulation of the process of ion–plasma sputter deposition using the proposed model allows optimum technological regimes to be selected, which ensures obtaining high-quality stoichiometric film materials of complex compositions.

Acknowledgments. This study was supported by the Russian Foundation for Basic Research, project no. 02-02-17667.

REFERENCES

1. F. Vassenden, G. Linker, and J. Geerk, Physica C **175**, 566 (1991).
2. S. Sievers, F. Mattheis, and H. Krebs, J. Appl. Phys. **78**, 5545 (1995).
3. A. H. Carim, S. N. Basu, and R. E. Muenchausen, Appl. Phys. Lett. **58**, 871 (1991).
4. C. W. Nieh, L. Anthony, J. Y. Losefowicz, *et al.*, Appl. Phys. Lett. **56**, 2138 (1990).
5. E. K. Hollmann, S. V. Razumov, and A. V. Tumarkin, Physica C **338**, 246 (2000).
6. V. A. Volpyas and P. M. Dymashevskiĭ, Zh. Tekh. Fiz. **71** (11), 1 (2001) [Tech. Phys. **46**, 1347 (2001)].
7. V. A. Volpyas, E. K. Gol'man, and M. A. Tsukerman, Zh. Tekh. Fiz. **66** (4), 16 (1996) [Tech. Phys. **41**, 304 (1996)].
8. V. A. Volpyas and A. B. Kozyrev, *Physics of Weakly Ionized Plasma (Monograph)* (Skladen, St. Petersburg, 1997) [in Russian].
9. V. A. Volpyas and E. K. Gol'man, Zh. Tekh. Fiz. **70** (3), 13 (2000) [Tech. Phys. **45**, 298 (2000)].
10. V. A. Volpyas, P. K. Petrov, and R. A. Chakalov, Vacuum **52**, 427 (1999).

Translated by P. Pozdeev

Technical Physics Letters, Vol. 30, No. 4, 2004, pp. 291–294. Translated from Pis'ma v Zhurnal Tekhnicheskoĭ Fiziki, Vol. 30, No. 7, 2004, pp. 69–76.

Duration of the Process of Complete Synchronization of Two Coupled Identical Chaotic Systems

A. A. Koronovskiĭ*, A. E. Hramov, and I. A. Khromova*****

State Scientific Center "College," Saratov State University, Saratov, Russia

*e-mail: * alkor@cas.ssu.runnet.ru; ** aeh@cas.ssu.runnet.ru; *** KhromovaIA@yandex.ru*

Received September 4, 2003

Abstract—We consider the time required for complete synchronization of two identical one-way coupled van der Pol–Duffing oscillators occurring in the regime of dynamic chaos. The influence of the initial phase difference between oscillators on the duration of the process of complete synchronization has been studied. At a fixed phase of chaotic oscillations of the self-excited drive oscillator, the period of time (past the coupling onset) during which the complete synchronization regime is established depends on the phase of the self-excited response oscillator. *© 2004 MAIK "Nauka/Interperiodica".*

The phenomenon of synchronization of self-excited oscillatory systems attracted the attention of researchers for a long time and is still an important problem in the modern theory of nonlinear oscillations and waves (see, e.g., [1–6]). In recent years, the duration of the synchronization process has been extensively studied for dynamical systems exhibiting both periodic and chaotic behavior [7–11]. The interest in this problem is related, in particular, to the extensively developing direction of research devoted to the use of chaotic signals for data transmission [12–14].

The time required for the complete (full) synchronization after the onset of external action can be considered as the duration of a transient process in a nonautonomous dynamical system. As is well known, the transient process duration in a dynamical system depends on the initial conditions and obeys certain laws [15–17]. In self-excited oscillators exhibiting periodic behavior, the initial conditions can be represented by the phase of oscillations. In particular, it was recently demonstrated [9] for self-excited oscillatory dynamical systems, both with a finite (van der Pol oscillator) and with infinite (distributed active medium of the "helical electron beam–backward electromagnetic wave" type) number of degrees of freedom under an external periodic action, that the duration of synchronization at the drive frequency significantly depends on the initial phase difference of oscillations in the response (slave) and drive (master) systems. Similar results were obtained for the time of complete synchronization of one-way coupled identical subsystems occurring in the regime of periodic oscillations [11].

In cases when a response dynamical system occurs in the regime of chaotic oscillations, the phase of these oscillations determined by one or another method [5, 18–20] does not uniquely determine the state of the system, although it is still a convenient characteristic. This study was aimed at establishing how the time of complete synchronization of two identical one-way coupled chaotic subsystems depends on the initial phase difference under otherwise variable initial conditions.

We have studied a model system comprising one-way coupled van der Pol–Duffing oscillators [21, 22]. As is known [23, 24], one-way coupled oscillators of this type (Fig. 1a) exhibit the phenomenon of complete chaotic synchronization. The drive oscillator is described by a system of dimensionless differential equations,

$$\dot{x} = -\nu[x^3 - \alpha x - y], \quad \dot{y} = x - y - z, \quad \dot{z} = \beta y, \quad (1)$$

and the response oscillator is described the system

$$\begin{aligned} \dot{u} &= -\nu[(u)^3 - \alpha u - v] + \nu\varepsilon(x-u)\sigma(\tau-\tau_0), \\ \dot{v} &= u - v - w, \quad \dot{w} = \beta v. \end{aligned} \quad (2)$$

Here, $\sigma(\xi)$ is the Heaviside function and (x, y, z) and (u, v, w) are the dynamical variables characterizing the states of the drive and response oscillators, respectively. These quantities are related to the dimensional values by the following formulas [23, 24]: $x = V_1\sqrt{bR}$; $y = V_2\sqrt{bR}$; $z = i_L\sqrt{bR^3}$; $u = U_1\sqrt{bR}$; $v = U_2\sqrt{bR}$; $w = i_L'\sqrt{bR^3}$.

The current–voltage characteristic of the nonlinear element N is described by a cubic parabola

$$i(V) = aV + bV^3. \quad (3)$$

The dimensionless time in the system of Eqs. (1) and (2) is defined as $\tau = t/(RC_2)$, and the dimensionless quantities α, β, and ν are related to the dimensionless

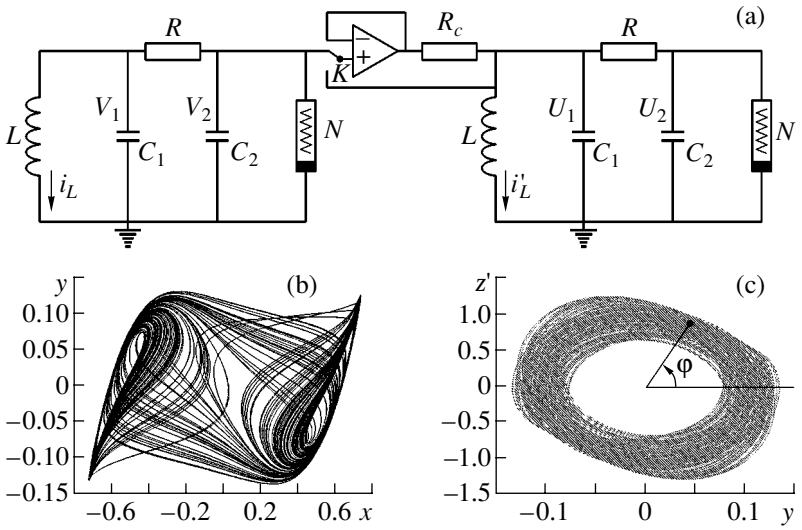

Fig. 1. A system of one-way coupled van der Pol–Duffing oscillators: (a) schematic diagram; (b) phase portrait of the drive oscillator (1) in a regime of bistable chaos with double-band chaotic attractor for the control parameters $\alpha = 0.35$, $\beta = 300$, and $\nu = 100$; (c) projection of the chaotic attractor onto the (y, z') plane for determining the phase φ of chaotic oscillations.

parameters of oscillators as $\alpha = -(1 + aR)$, $\beta = C_2R^2/L$, and $\nu = C_2/C_1$; the coupling parameter is $\varepsilon = R/R_c$.

The system of equations describing one-way coupled oscillators (1) and (2) was numerically solved using the fourth-order Runge–Kutta method with an integration time step of $\Delta\tau = 2 \times 10^{-5}$. The control parameters were set (by analogy with [24]) equal to $\alpha = 0.35$, $\beta = 300$, and $\nu = 100$, for which the system (1) exhibits bistable chaotic dynamics (Fig. 1b). The coupling parameter was selected equal to $\varepsilon = 1.35$, which ensures settling of the regime of complete synchronization of the two subsystems [24].

The one-way coupling of the self-excited drive and response oscillators was switched on at a time τ_0 when the transient processes in both subsystems were accomplished and the imaging points in the phase spaces (x, y, z) and (u, v, w) reached the corresponding chaotic attractors. Prior to this moment, both oscillators occurred in the state of autonomous self-excited oscillations. The period of time T_s required for the complete synchronization was determined as

$$T_s = \tau_s - \tau_0, \tag{4}$$

where τ_s is the time corresponding to the onset of complete synchronism. A criterion for the complete synchronization was selected in the following form:

$$\sqrt{(x-u)^2 + (y-v)^2 + (z-w)^2} \le 5 \times 10^{-3}, \quad \forall\tau \ge \tau_s. \tag{5}$$

The phase φ of chaotic oscillations for each oscillator was defined as the angle of projection of the chaotic attractor onto the plane of a new coordinate system: ($y' = y$, $z' = -0.8192x + 0.5735z$) for the drive oscillator (Fig. 1c) and ($v' = v$, $w' = -0.8192u + 0.5735w$) for the response oscillator (see [5, 18, 19]).

In the course of numerical simulation of Eqs. (1) and (2), the coupling between oscillators was always switched on at the same moment of time τ_0, when the dynamical variables characterizing the state of the drive system (1) were $x = 0.41009$, $y = -0.09994$, $z = 0.75978$, which corresponded to the phase of chaotic oscillations in the drive (master) system $\varphi_m = 3\pi/4$. The initial conditions (u, v, w) for the response oscillator (2) at the moment of coupling onset were taken different for each simulation, but such that the imaging point would belong to a chaotic attractor and the initial phase φ_s of the response (slave) system would also be fixed.

The chaotic attractor of each system has two "bands" ($x < 0$ and $x > 0$) corresponding to bistable chaotic dynamics, whereby the system exhibits switching between the two states (Fig. 1b). For this reason, the duration of synchronization for each initial slave phase φ_s was studied separately for the upper and lower band of the chaotic attractor. The initial conditions for the drive oscillator were always taken the same (see above), corresponding to the upper (positive) band of the chaotic attractor.

The results of numerical simulations showed that the time of complete synchronization for the dynamical systems with bistable chaotic attractors depends on whether the initial conditions in the drive and response oscillators belong to the like or unlike bands of the corresponding chaotic attractor. When the initial conditions are selected on different bands (e.g., the upper band for the drive oscillator and the lower band for the response oscillator) of the chaotic attractor, the duration of complete synchronization depends to a significant

extent on the phase of chaotic oscillations in the response subsystem (for a fixed initial phase of the drive oscillator).

These results are illustrated in Figs. 2a and 2b, showing the distribution of synchronization times T_s for different initial phases φ_s of chaotic oscillations in the response oscillator. Each distribution is constructed for 100 sets of initial conditions (with the same initial phase) belonging to the lower band of the chaotic attractor. As can be seen, the shape of distributions is close to the δ function. This indicates that the time of complete synchronization in the system described by Eqs. (1) and (2) is determined by the phase of chaotic oscillations. For various initial conditions (belonging to the lower band of the chaotic attractor) corresponding to the same initial slave phase φ_s, the time of complete synchronization is also virtually the same.

A somewhat different pattern is observed when the initial conditions for the response oscillator at the coupling onset time τ_0 are selected so that the imaging points fall within the like (in this case, the upper) bands of bistable chaotic attractors. If the initial phases of the drive (φ_m) and response (φ_s) oscillators differ rather significantly, the distribution of synchronization times, like that observed for the initial conditions belonging to the unlike bands, has a shape close to the δ function (Fig. 2c). However, should the initial phases of the drive and response oscillators be sufficiently close (for the imaging points in the like bands of the chaotic attractors), the distribution of synchronization times "scatters" (Fig. 2d). In this case, the time of complete synchronization of two one-way coupled subsystems varies within rather broad limits for the same initial phase of chaotic oscillations of the response subsystem.

This phenomenon is probably explained as follows. When the imaging points corresponding to the dynamics of drive and response oscillators have close initial phases and occur in the like bands of chaotic attractors, the subsystems can be sufficiently close to the state of complete synchronism. In this case, the time of complete synchronization will be much shorter than that for the same oscillators in the initial states significantly far from synchronism. However, the fact that the imaging points have close initial phases and belong to the like bands by no means implies that the two subsystems are necessarily close to synchronism, since it is known that chaotic dynamics is characterized by exponential expansion of the phase trajectories [25]. Therefore, the synchronization time T_s will be comparable with that for the other initial slave phases φ_s. For this reason, the distribution f synchronization ties T_s acquires the form depicted in Fig. 2d.

Thus, the time of synchronization of one-way coupled van der Pol–Duffing oscillators occurring in the regime of chaotic oscillations depends on the initial phase φ_s of chaotic oscillations in the response oscillator (at a fixed initial phase φ_m of the drive oscillator).

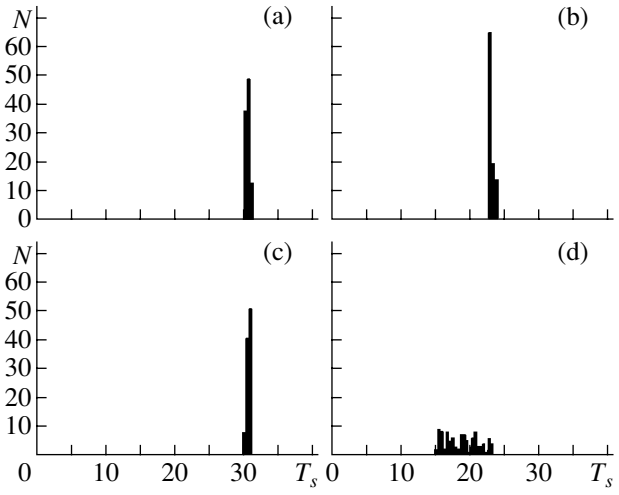

Fig. 2. Distributions of the time of complete synchronization of one-way coupled van der Pol–Duffing oscillators. The initial conditions for the drive oscillator are selected in the upper band of the bistable chaotic attractor and correspond to the initial phase $\varphi_m = 3\pi/4$. The initial conditions for the response oscillator are as follows: (a) lower band, $\varphi_s = 1.03$; (b) lower band, $\varphi_s = 1.73$; (c) upper band, $\varphi_s = 1.03$; (d) upper band, $\varphi_s = 2.78$. Each distribution is constructed for 100 sets of initial conditions randomly selected on the corresponding chaotic attractor.

Another important factor is whether the imaging points corresponding to the states of the drive and response oscillators occur in the like or unlike bands of the bistable chaotic attractors at the time τ_0 of switching on the one-way coupling between the subsystems. When the imaging points belong to the unlike bands, the time T_s of complete synchronization is virtually the same for all initial conditions corresponding to the same slave phase φ_s. However, should the imaging points of the two oscillators occur in the like bands of their chaotic attractors and have not strongly different initial phases at the moment of coupling onset, the average time of complete synchronization decreases and the shape of the T_s distribution becomes different from the δ function characteristic of the situations with other initial slave phases φ_s.

Acknowledgments. This study was supported by the Russian Foundation for Basic Research (project no. 02-02-16351) and jointly by the Scientific-Education Center "Nonlinear Dynamics and Biophysics" at Saratov State University and the US Civilian Research and Development Foundation for the Independent States of the Former Soviet Union (CRDF grant no. REC-006).

REFERENCES

1. I. I. Blekhman, *Synchronization of Dynamical Systems* (Nauka, Moscow, 1971) [in Russian].
2. I. I. Blekhman, *Synchronization in Nature and Engineering* (Nauka, Moscow, 1981) [in Russian].

3. P. S. Landa, *Nonlinear Oscillations and Waves in Dynamical Systems* (Kluwer, Dordrecht, 1996).
4. V. S. Anishchenko, T. E. Vadivasova, and V. V. Astakhov, *Nonlinear Dynamics of Random and Stochastic Systems* (Izd. Sarat. Univ., Saratov, 1999) [in Russian].
5. A. Pikovsky, M. Rosenblum, and J. Kurths, Int. J. Bifurcation Chaos Appl. Sci. Eng. **10**, 2291 (2000).
6. V. S. Anishchenko and T. E. Vadivasova, Radiotekh. Élektron. (Moscow) **47**, 133 (2002).
7. H. K. Leung, Phys. Rev. E **58**, 5704 (1998).
8. P. Woafo and R. A. Kraenkel, Phys. Rev. E **65**, 036225 (2002).
9. A. A. Koronovskiĭ, D. I. Trubetskov, and A. E. Hramov, Dokl. Akad. Nauk **389**, 749 (2003) [Dokl. Phys. **48**, 166 (2003)].
10. D. I. Trubetskov, A. A. Koronovskiĭ, and A. E. Hramov, Izv. Vyssh. Uchebn. Zaved. Radiofiz. (in press).
11. A. A. Koronovskiĭ, A. E. Hramov, and I. A. Khromova, Pis'ma Zh. Tekh. Fiz. **30** (6), 79 (2004) (in press).
12. K. M. Cuomo and A. V. Oppenheim, Phys. Rev. Lett. **71**, 65 (1993).
13. A. S. Dmitriev, L. V. Kuz'min, A. I. Panas, and S. O. Starkov, Radiotekh. Élektron. (Moscow) **43**, 1115 (1998).
14. A. S. Dmitriev, M. Hasler, A. I. Panas, and K. V. Zakharchenko, Nonlinear Phenomena in Complex Systems **6** (1), 1 (2003).
15. A. A. Koronovskiĭ, A. E. Hramov, and I. A. Khromova, Izv. Vyssh. Uchebn. Zaved. Prikl. Nelineĭnaya Din. **11** (1), 36 (2003).
16. A. A. Koronovskiĭ, D. I. Trubetskov, A. E. Hramov, and A. E. Khramova, Izv. Vyssh. Uchebn. Zaved. Radiofiz. **45**, 880 (2002).
17. G. B. Astaf'ev, A. A. Koronovskiĭ, A. E. Hramov, and A. E. Khramova, Izv. Vyssh. Uchebn. Zaved. Prikl. Nelineĭnaya Din. **11** (4) (2003) (in press).
18. M. G. Rosenblum, A. S. Pikovsky, and J. Kurths, Phys. Rev. Lett. **76**, 1804 (1996).
19. M. G. Rosenblum, A. S. Pikovsky, and J. Kurths, Phys. Rev. Lett. **78**, 4193 (1997).
20. M. G. Rosenblum and J. Kurths, *Nonlinear Analysis of Physiological Data*, Ed. by H. Kantz and J. Kurths (Springer, Berlin, 1998), pp. 91–99.
21. G. P. King and S. T. Gaito, Phys. Rev. A **46**, 3092 (1992).
22. M. G. M. Gomes and G. P. King, Phys. Rev. A **46**, 3100 (1992).
23. K. Murali and M. Lakshmanan, Phys. Rev. E **48**, R1624 (1993).
24. K. Murali and M. Lakshmanan, Phys. Rev. E **49**, 4882 (1994).
25. S. P. Kuznetsov, *Dynamic Chaos*, in *Modern Theory of Vibrations and Waves* (Fizmatlit, Moscow, 2001) [in Russian].

Translated by P. Pozdeev

Technical Physics Letters, Vol. 30, No. 4, 2004, pp. 295–297. Translated from Pis'ma v Zhurnal Tekhnicheskoĭ Fiziki, Vol. 30, No. 7, 2004, pp. 77–82.

Velocities of Nanometer-Scale Displacements Determined Using the Autodyne Signal Spectrum of a Quantum-Confined Semiconductor Structure Laser

D. A. Usanov*, A. V. Skripal', and A. S. Kamyshanskiĭ

Saratov State University, Saratov, Russia

** e-mail: UsanovDA@info.sgu.ru*

Received August 25, 2003

Abstract—We have studied the possibility of using an autodyne signal of a quantum-confined semiconductor structure laser for determining the velocities of motions on a nanometer scale. It is suggested to normalize the laser autodyne signal with respect to additional mechanical oscillations induced in the object at an amplitude of no less than half of the laser radiation wavelength. In this case, the velocity of displacements can be determined by measuring the autodyne signal phase increment. © *2004 MAIK "Nauka/Interperiodica".*

In recent years, it has been demonstrated that lasers based on quantum-confined semiconductor structures can be used for determining the characteristics of vibrations on a nanometer level [1–4] in various objects. The field of such applications would be further expanded, provided that the velocities of motions on a nanometer scale could be measured as well. Such data are required, for example, in the characterization of thermal expansion of slowly heated or nanodimensional objects.

In this context, we have studied the possibility of using an autodyne signal of a quantum-confined semiconductor structure laser for determining the velocities of motions on a nanometer scale.

The variable informative component of a laser autodyne signal at a feedback level significantly below unity can be written in the following form [4]:

$$P = \cos(\omega_0 \tau(t)), \tag{1}$$

where $\tau(t)$ is the round trip time of the laser radiation for the distance L from laser to the external reflector and ω_0 is the resonance frequency of a laser diode without feedback. If the external reflector (spaced from the laser diode cavity by a distance L_0 at the time $t = 0$) moves at a velocity v, the laser signal travel time varies according to the law

$$\tau_0(t) = \frac{2}{c}\left(L_0 + \int_0^t v(t')dt'\right). \tag{2}$$

For normalizing the autodyne signal intensity, we suggest the signal amplitude to be divided by a maximum value corresponding to a reflector displacement by no less than half of the laser radiation wavelength. Using the normalized autodyne signal, it would be possible to determine the object velocity $v(t)$ by measuring $P(t)$ and using relation (1). Unfortunately, methods for solving such inverse problems are not yet developed. On the other hand, there are well-developed and verified methods for solving the inverse problems in the case of a reflector performing periodic (in particular, harmonic) oscillations [5]. Thus, upon exciting additional mechanical oscillations in the object whose velocity has to be determined, it will be possible to measure τ_0 and find the unknown velocity $v(t)$ by solving the corresponding inverse problem using verified spectral techniques.

Let harmonic oscillations to be excited in the moving object studied,

$$f(t) = \xi \sin(\Omega t + \varepsilon), \tag{3}$$

where ξ and Ω are the amplitude and frequency of oscillations of the external reflector, respectively, and ε is the initial phase. The autodyne signal travel time in this system can be expressed as

$$\tau(t) = \tau_0(t) + \tau_a \sin(\Omega t + \varepsilon), \tag{4}$$

where $\tau_a = 2\xi/c$.

The rate of variation of the amplitude of excited mechanical oscillations should be much greater than the object velocity. In this case, the inverse problem can be solved using the oscillation spectrum measured at each particular time with neglect of the τ_0 increment related to the slow motion. Thus, the oscillatory system comprises a "fast" subsystem, involving the induced additional oscillations, and a "slow" subsystem performing displacements on a nanometer scale. In deter-

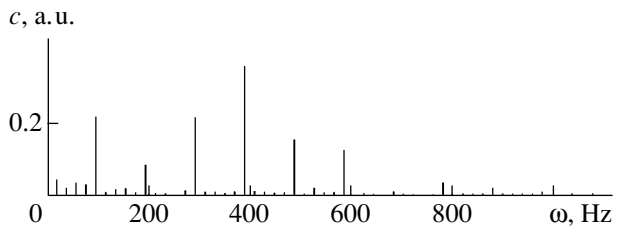

Fig. 1. Autodyne signal spectrum measured within a time window equal to five periods of oscillations of the object.

mining τ for each particular time interval, the value of τ_0 can be considered as constant, entering as a parameter into the total variable τ. Then, the autodyne signal can be written in the following form:

$$P(t) = \cos(\theta(t) + \sigma\sin(\Omega t + \varepsilon)), \quad (5)$$

where $\theta(t) = \omega_0\tau_0(t)$ is the autodyne signal phase increment, $\sigma = 4\pi\xi/\lambda$, and λ is the laser radiation wavelength.

Let us represent $P(t)$ in the form of expansion with respect to the Bessel functions,

$$P(t) = \cos\theta J_0(\sigma) + 2\cos\theta\sum_{n=1}^{\infty} J_{2n}(\sigma)\cos[2n\Omega t + \varepsilon] - 2\sin\theta\sum_{n=1}^{\infty} J_{2n-1}(\sigma)\cos[(2n-1)\Omega t + \varepsilon], \quad (6)$$

where J_n are the nth order Bessel functions (n is the number of the spectral component of the autodyne signal detected). Let us also expand the autodyne signal into Fourier series,

$$P(t) = \frac{1}{2}a_0 + \sum_{n=1}^{\infty}\{a_n\cos n\omega t - b_n\sin n\omega t\}, \quad (7)$$

where a_n and b_n are the expansion coefficients. Equating the two expansions, we obtain relations for calculation of the amplitude of longitudinal oscillations of the object studied:

$$\xi^2 = \frac{\lambda^2}{\pi^2}\frac{6(c_n + c_{n+1})}{(c_n + c_{n+2})(c_{n-1} + c_{n+1})}, \quad (8)$$

where c_n are the coefficients proportional to the spectral components of the signal (these coefficients can be determined as described, e.g., in [6]).

Using the expansions of $P(t)$ into series with respect to the Bessel functions and Fourier harmonics, we can calculate the autodyne phase increment using coefficients c_n with four sequential numbers n:

$$\theta_{2n} = \arctan\left[\sqrt{\frac{(2n+1)}{(2n-1)}\frac{(c_{2n+3} + c_{2n+1})c_{2n+1}}{(c_{2n+2} + c_{2n})c_{2n+2}}}\right] \quad (9)$$

or

$$\theta_{2n-1} = \arctan\left[\sqrt{\frac{(2n+1)}{2n}\frac{(c_{2n+1} + c_{2n-1})c_{2n+1}}{(c_{2n+2} + c_{2n})c_{2n}}}\right]. \quad (10)$$

Formulas (9) and (10) are used when the phase increment is determined using four sequential c_n coefficients beginning with an even and odd number, respectively.

By moving the "window" (i.e., the time interval in which the measured signal is analyzed) along the time axis and calculating the corresponding phase increments of the laser autodyne signal, we obtain a slowly varying function $\theta(t)$. Using this dependence, we can determine the object velocity averaged over the given time window Δt:

$$v(t) = \frac{\lambda}{4\pi}\frac{\Delta\theta}{\Delta t}. \quad (11)$$

The experimental investigation was performed using an autodyne measuring system employing a laser diode of the RLD-650 type based on a quantum-confined semiconductor structure operating on a diffraction-limited solitary spatial mode. The laser parameters were as follows: output power, 5 mW; working wavelength, 652 nm; threshold current 20 mA.

The output radiation of the semiconductor laser struck a reflector mounted on a sample. The sample with reflector was driven by a $BaTiO_3$ piezoceramic transducer excited with a signal of an audio-frequency generator. Part of the radiation reflected from the object returned to the semiconductor laser cavity. The change in the laser output power was measured with a photodetector. The photodetector signal, passed via an ac filter and amplified by a broadband amplifier, was processed by an analog-to-digital converter and fed into a computer for data processing, storage, and display.

For determining the object velocity, it is necessary to determine the frequency Ω, the oscillation amplitude ξ, and the phase increment θ of the autodyne signal. These values were calculated from the measured autodyne signal components using formulas (8)–(10). Taking into account that the window Δt used for the signal processing has to be, on the one hand, sufficiently small to provide for the constancy of the phase increment (θ = const) within this time interval and, on the other hand, sufficiently large to provide for a good spectral resolution, we selected Δt equal to five periods of the object oscillations (0.05 s).

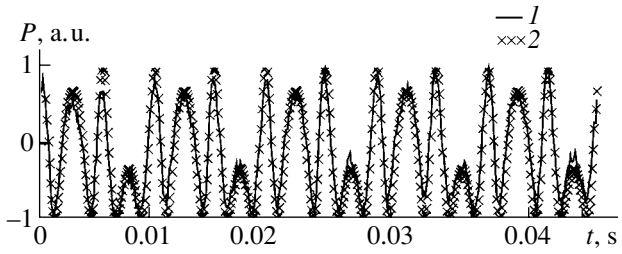

Fig. 2. Waveforms of the (*1*) experimental (initial) and (*2*) reconstructed autodyne signals (rms deviation, 0.1).

Figure 1 shows the spectrum of the autodyne signal measured within a time window equal to five periods of the object oscillations. Using this spectrum, the frequency Ω, oscillation amplitude ξ, and phase increment θ of the autodyne signal were determined. Then, the initial phase was calculated and the autodyne signal was reconstructed assuming that θ = const within a Δt interval.

Figure 2 presents the autodyne signal reconstructed as described above in comparison with the measured waveform. The autodyne signal was separated into 0.05-s-long portions by increasing the forming interval with a 0.01 s step. The mutual overlap of processed intervals favors an increase in the accuracy of calculations. An analysis of all such regions gave the time variation of the autodyne signal phase increment $\theta(t)$, which had the shape of a sloped straight line. A comparison of the theoretical dependence of the phase increment with the plot constructed by the experimental data allowed the rate of the thermal expansion of the object studied to be estimated at 50 nm/s.

Thus, we have demonstrated that a quantum-confined semiconductor structure laser operating in the autodyne regime allows the motion of objects moving with small velocities to be studied on a nanometer scale, provided that additional mechanical oscillations are induced in the object at an amplitude of no less than half of the probing laser radiation wavelength.

Acknowledgments. This study was supported by the Ministry of Education of the Russian Federation within the framework of the Program “Basic Research by Scientific and Pedagogical Staff of Higher Schools” (project no. 2.12.03).

REFERENCES

1. Yu. A. Bykovskiĭ, K. B. Dedushenko, M. V. Zver’kov, and A. N. Mamaev, Kvantovaya Élektron. (Moscow) **19**, 657 (1992).
2. S. Donati, G. Giuliani, and S. Merlo, IEEE J. Quantum Electron. **31**, 113 (1995).
3. N. N. Ledentsov, V. M. Ustinov, V. A. Shchukin, *et al.*, Fiz. Tekh. Poluprovodn. (St. Petersburg) **32**, 385 (1998) [Semiconductors **32**, 343 (1998)].
4. D. A. Usanov and A. V. Skripal’, Pis’ma Zh. Tekh. Fiz. **29** (9), 51 (2003) [Tech. Phys. Lett. **29**, 377 (2003)].
5. D. A. Usanov, A. V. Skripal’, and S. V. Gangnus, Avtometriya, No. 1, 117 (2001).
6. D. A. Usanov, Al. V. Skripal’, and An. V. Skripal’, *Numerical Methods in Physics of Solids: Student’s Manual* (Izd. Saratov. Univ., Saratov, 2002), p. 136.

Translated by P. Pozdeev

Technical Physics Letters, Vol. 30, No. 4, 2004, pp. 298–300. Translated from Pis'ma v Zhurnal Tekhnicheskoĭ Fiziki, Vol. 30, No. 7, 2004, pp. 83–87.

Local Enhanced Evaporation of Carbon Pellets in a Wendelstein 7-AS Stellarator

V. M. Timokhin[a], B. V. Kuteev[a], V. Yu. Sergeev[a], V. G. Skokov[a], and R. Burhenn[b]

[a] *St. Petersburg State Technical University, St. Petersburg, Russia*

[b] *Max Planck Institut für Plasmaphysik, EURATOM Ass., 17491 Greifswald, Germany*

Received September 9, 2003

Abstract—Experiments with second-harmonic electron cyclotron resonance plasma heating performed on a Wendelstein 7-AS stellarator revealed a new regime of the carbon pellet evaporation, whereby sharp peaks with the characteristic spatial width of a few millimeters appeared on the evaporation rate profile. The peaks were observed in a peripheral region of the plasma column for an electron density in the central region below and the heating power above the threshold values. The appearance of these peaks is correlated with the observation of a superthermal emission in the low-frequency part of the cyclotron radiation spectrum. The observed effect is related to the excitation of superthermal electrons by the cyclotron radiation of gyrotrons. The energy and density of the superthermal electron population are estimated at 30–50 keV and 10^{11}–10^9 cm^{-3}, respectively.

Superthermal electrons can significantly influence the properties of a high-temperature plasma in tokamaks and stellarators [1, 2]. The appearance of such groups of electrons was detected using cyclotron radiation detectors in the plasma of a Wendelstein 7-AS stellarator (W7-AS) operating in the regimes of high-power (~1 MW) microwave second-harmonic electron cyclotron resonance heating (ECRH) and a low electron density (~10^{13} cm^{-3}) of the plasma [2, 3]. Investigations of the process of carbon pellet evaporation in such regimes (see [4, 5]) revealed the zones of enhanced evaporation on a centimeter scale in the peripheral regions of the plasma column. The effect was related to an increase in the energy flux to the pellet surface caused by the superthermal electron population.

Below, we describe a qualitatively new regime of pellet evaporation characterized by sharp cyclotron radiation emissions from spatial regions on a millimeter scale and suggest a mechanism describing this phenomenon.

In the experiments under consideration, spherical carbon pellets with a diameter of 0.40 ± 0.01 mm were accelerated using a DIM-6 injector [6] to a velocity from 150 to 350 m/s toward the plasma column center. The pattern of pellet evaporation was monitored from two directions by several high-speed CCD cameras and a wide-aperture photodetector. The optical filters with a transmission band at 720 ± 5 nm were used to separate the dominating CII line emission, the intensity of which was assumed to be proportion al to the pellet evaporation rate [7]. The scheme of experiments has been described in more detail elsewhere [5, 7].

Figure 1 shows the typical evaporation rate profiles measured along the pellet trajectory (see [7]) for various ECRH powers (a) and plasma densities (b). The coordinate along the pellet trajectory is measured relative to the center of the vacuum chamber, the positive direction being toward the center of the W7-AS setup. Each pellet crossed the separatrix in the region of 16–14 cm along the trajectory, depending on the discharge and injection parameters.

As can be seen from Fig. 1a, the electron density in the central region $n_e(0) = 4.5 \times 10^{13}$ cm^{-3} at $P_{\mathrm{ECRH}} = 400$ kW (shot 50055) corresponds to a smooth profile of the evaporation rate $\dot{N}$. As P_{ECRH} increases to 700 kW (shot 50058), the characteristic local enhanced evaporation zone appears in the peripheral region of the plasma column. This zone contains two narrow (FWHM, ~0.1 cm) peaks with the evaporation rate more than five times the average $\dot{N}$ value in the smooth profile. When the P_{ECRH} value is increased to 900 kW (shot 49966), the zone of enhanced evaporation expands to 2 cm and the number of peaks increases to seven.

Figure 1b shows the $\dot{N}(r)$ profiles for the pellets evaporated in a plasma with $P_{\mathrm{ECRH}} = 900$ kW for $n_e(0) = (1.8, 4.5, 6.0) \times 10^{13}$ cm^{-3}. As can be seen from these data, a decrease in the charge density leads to expansion of the enhanced evaporation zone and to an increase in the number of peaks in the evaporation rate profile. The threshold of disappearance of the zone of local enhanced evaporation at this power occurs above 6.0×10^{13} cm^{-3} (the maximum value in the experiments reported here). Thus, the phenomenon of local enhanced evaporation was observed under all discharge conditions studied in this series.

1063-7850/04/3004-0298$26.00 © 2004 MAIK "Nauka/Interperiodica"

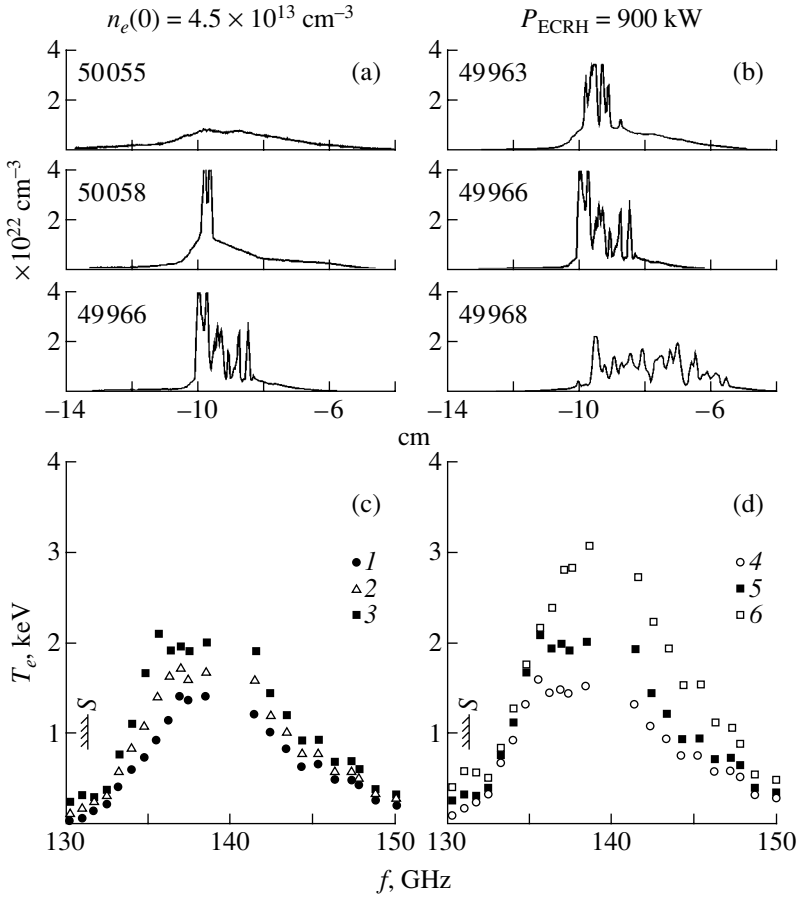

Fig. 1. (a, b) Profiles of the carbon pellet evaporation rate and (c, d) the corresponding cyclotron radiation spectra (*S* indicates the position of plasma column separatrix) for discharges with fixed (a, c) electron densities and (b, d) ECRH power: (*1*) shot 50055 (P_{ECRH} = 400 kW); (*2*) shot 50058 (P_{ECRH} = 700 kW); (*3*) shot 49966 (P_{ECRH} = 900 kW); (*4*) shot 49963 ($n_e = 6.0 \times 10^{13}$ cm^{-3}); (*5*) shot 49966 ($n_e = 4.5 \times 10^{13}$ cm^{-3}); (*6*) shot 49968 ($n_e = 1.8 \times 10^{13}$ cm^{-3}).

Figures 1c and 1d show the cyclotron radiation spectra of discharges corresponding to the evaporation rate profiles $\dot{N}(r)$ depicted in Figs. 1a and 1b, respectively. As can be seen, an increase in P_{ECRH} and a decrease in the $n_e(0)$ leads to a growth in the intensity of emission in the frequency interval 130–133 GHz corresponding to the electron cyclotron resonance region beyond the plasma column separatrix [2, 3]. Superthermal electrons are generated in the cross section of ECRH power deposition and spread over the whole magnetic field surface with partial thermalization due to collisions. In this way, superthermal electrons reach the injection cross section outside the tore and induce the effects manifested in the $\dot{N}(r)$ profiles. Therefore, pellets produce effective "backlight" of the groups of superthermal electrons and allow their exact location in the plasma to be determined (which is impossible by means of cyclotron radiation diagnostics).

Having determined the positions of peaks on the $\dot{N}(r)$ profile and assuming that the low-frequency part of the cyclotron radiation spectrum is related to superthermal electrons, we can estimate their energies (E_{st}) by measuring the relativistic shift of the frequency of emission toward lower values. These estimates yield $E_{st} \sim 3$–20 keV. By measuring the ratio of the evaporation rates inside and outside the peak, it is possible to evaluate the ratio of energy fluxes toward the pellet surface due to thermal and superthermal electrons. Then, once the E_{st} value is known, it is possible to estimate the corresponding electron density as $n_{st} \propto n_e(T_e/E_{st})^{3/2}$, where n_e and T_e are the electron density and temperature in the background plasma. Using this approach, the superthermal electron densities responsible for the features observed in the $\dot{N}(r)$ profiles were estimated within $n_{st} \sim 10^{11}$–10^{12} cm^{-3}. This accounts for 1% (for E_{st} = 20 keV) to 10% (for E_{st} = 3 keV) of the background plasma density.

An alternative estimate can be obtained by assuming that superthermal electrons are generated at the cross section of ECRH power deposition from the side of

strong field on the same magnetic field surfaces that correspond to peaks in the $\dot{N}(r)$ profiles in the injection cross section. According to calculations of the magnetic field configuration of W7-AS, the zone of these magnetic field surfaces is displaced ~10 cm from the magnetic axis toward the strong field region. Using the resonance condition in this region and taking into account the relativistic mass shift $\omega_{ce} = eB/m_0c\gamma = 140$ GHz, we estimate the energy of the superthermal electron population as 30–50 keV (e is the electron charge, B is the magnetic induction in the zone of superthermal electron production, m_0 is the rest mass of electron, c is the speed of light, and γ is the relativistic factor). In this case, the estimated superthermal electron density decreases to $n_{st} \sim 10^9$–10^{11}, which accounts for 0.001–1% of the background plasma density.

Thus, the regimes of high-power microwave second-harmonic ECRH revealed local enhanced evaporation of carbon pellets in the plasma of a W7-AS stellarator. Behavior of the local enhanced evaporation zones depending on the plasma parameters and its correlation with the low-frequency part of the cyclotron radiation spectrum indicate that the observed phenomenon is related to superthermal electrons. Estimates based on the relativistic frequency shift indicate that the observed effects can be produced by a population of superthermal electrons with energies in the interval of 30–50 keV and a density ranging within 10^9–10^{11} cm^{-3}. The cyclotron radiation spectra and the positions of peaks in the $\dot{N}(r)$ curves show that the plasma under local enhanced evaporation may contain superthermal electrons with the energies within 3–20 keV. Therefore, it would be expedient to perform additional measurements in the low-frequency part of the cyclotron radiation spectrum (up to 120 GHz), where the emission of electrons with energies on the order of 50 keV should be manifested.

Acknowledgments. The authors are grateful to the staff of Wendelstein 7-AS for their help in conducting experiments.

This study was supported in part by the Russian Foundation for basic Research, project no. 02-02-17555a.

REFERENCES

1. V. V. Parail and O. P. Pogutse, Rev. Plasma Phys. **11**, 1 (1986).
2. M. Rome, V. Erckmann, U. Gasparino, *et al.*, Plasma Phys. Controlled Fusion **39**, 117 (1997).
3. M. Hase, W. Pernreiter, and H. J. Hartfufl, J. Plasma Fusion Res. **1**, 99 (1998).
4. S. M. Egorov, B. V. Kuteev, I. V. Miroshnikov, *et al.*, Nucl. Fusion **32**, 2025 (1992).
5. L. Ledl *et al.*, Europhys. Conf. Abstr. **23J**, 1477 (1999).
6. P. T. Lang, P. Cierpka, R. S. Lang, *et al.*, Rev. Sci. Instrum. **65**, 2316 (1994).
7. L. Ledl, PhD Thesis (Max-Planck-Inst. für Plasmaphysik, 2000), IPP-Report III/257.

Translated by P. Pozdeev

Technical Physics Letters, Vol. 30, No. 4, 2004, pp. 301–303. Translated from Pis'ma v Zhurnal Tekhnicheskoĭ Fiziki, Vol. 30, No. 7, 2004, pp. 88–94.

Electron Transport in Xenon–Hydrogen Gas Mixtures

V. M. Atrazhev[a,*], V. V. Dmitrenko[b,], and I. V. Chernysheva[b,***]**

[a] *Institute for High Energy Densities, Associated Institute for High Temperatures, Russian Academy of Sciences, Moscow, Russia*

[b] *Moscow Physical Engineering Institute (State Technical University), Moscow, Russia*

*e-mail: * atrazhev@yandex.ru; ** dmitren@kfl.mephi.ru; *** Chernysheva@nm.ru*

Received August 20, 2003

Abstract—We present the results of numerical solution of the Boltzmann equation in a two-term approximation taking into account both elastic and inelastic electron collisions in Xe–H_2 gas mixtures. Using the obtained electron energy distribution functions, the electron transport properties (drift velocities, mobilities, mean and characteristic energies, diffusion coefficients) are calculated for the E/N parameter (the electric field strength to gas density ratio) ranging within several townsends. A similarity rule is derived for the properties of Xe–H_2 mixtures of various densities, which allows the electron transport coefficients to be determined for the mixtures with small (below 4%) hydrogen content. © *2004 MAIK "Nauka/Interperiodica".*

A promising direction of development of gamma-radiation spectrometry is related to the creation of new detectors based on high-pressures ionization chambers filled with xenon [1]. The main task of gamma spectrometry measurements is to determine the intensities of discrete emission lines from various sources and to identify these sources. This determines the requirements to instruments, which should possess a high energy resolution, high operation speed, high efficiency of the total absorption measurements, good working parameters (simple maintenance, reliability, long working life), resistance to environmental factors, and low cost.

The performance characteristics of detectors based on gas-filled ionization chambers depend on the transport properties of electrons generated by gamma quanta in the working gas. The energy resolution, spatial resolution, and operation speed are determined by the ability of electrons to drift in the working gas at a maximum velocity and a minimum diffusion blurring. For optimizing the parameters of working gases (pressure, temperature, molecular additives) for ionization chambers, it is necessary to study the transport properties of electrons injected into such media.

Adding molecular hydrogen to inert gases (Ar, Kr, Xe) is widely used as a means of increasing the electron drift velocity in gas-filled radiation detectors [2]. This paper presents the results of calculations of the electron transport coefficients for Xe–H_2 mixtures, based on numerical solution of the Boltzmann equation for the electron energy distribution function. The results of calculations are compared to the published experimental data on the drift velocities and the characteristic transverse energies in Xe–H_2 mixtures [3, 4] and in pure hydrogen [5]. The electron transport properties are determined in a broad range of electric field strengths and molecular admixture concentrations.

The kinetics of electrons moving in molecular and atomic gases are significantly different. In atomic gases, electrons with the kinetic energies below 10 eV exhibit only the elastic collisions with atoms and lose a small energy fraction proportional to $\delta \sim 2m/M \ll 1$, where m and M are the masses of electron and atom, respectively. The smallness of parameter δ allows the integral of elastic collisions between electrons and atoms to be written in a divergent form, thus reducing the Boltzmann equation to a second-order differential equation for the symmetric part of the electron energy distribution function $f_0(\varepsilon)$. Note that the energy losses during elastic collisions take place for any electron energies.

The situation is substantially different in molecular gases, where electrons may exhibit inelastic collisions with molecules, leading to the excitation of their vibrational and/or rotational degrees of freedom. In these processes (inelastic collisions of type I), electrons lose a considerable fraction of their energies, which is equal to the quantum ε_i of the corresponding vibrational and rotational excitation energy. Another characteristic feature of such inelastic processes is the existence of a certain threshold, whereby electrons with energies below the excitation quantum ($\varepsilon < \varepsilon_i$) are not involved in inelastic collisions with energy losses. An exception is the inelastic collision process of type II, whereby an electron collides with a molecule in an excited state and gains the energy equal to that of the corresponding excitation quantum. The main property of such inelastic processes, which are possible for electrons with any energy, is that colliding electrons gain a considerable energy quantum. Inelastic collisions do not lead to diffusion blurring in the energy space (which is the main condition for writing the collision integral in a divergent form) and are manifested by the passage of an

electron from the phase volume $d\varepsilon$ at the energy ε to that near the energy $\varepsilon - \varepsilon_i$ (for the inelastic collision of type I) or near $\varepsilon + \varepsilon_i$ (for the inelastic collision of type II).

We have solved the stationary Boltzmann equation for the isotropic part of the electron energy distribution function $f_0(\varepsilon)$ in a homogeneous (or weakly varying) electric field E taking into account both elastic and inelastic collisions of electrons with gas molecules. The heating of electrons in the field will be described in a two-term approximation [6] with neglect of the influence of the electron density gradient on the distribution function. This is acceptable for calculations of the electron mobility $\mu(E/N)$ and the coefficient of diffusion $D_T(E/N)$ across the electric field. The considerations below refer to a mixture of atomic and molecular gases with the fraction of molecules $\chi = N_M/N$, where $N = N_A + N_M$ is the total concentration and N_A and N_M are the partial concentrations of atoms and molecules in the gas phase.

The frequency of elastic collisions will include the interactions of electrons both with atoms and with molecules. The frequency of energy transfer during elastic scattering will also take into account the elastic collisions with both atoms and molecules. The integral of inelastic collisions on the right-hand side of the equation is proportional to the concentration of molecules N_M. In rarefied gases, the electron transport coefficients depend on the electric field strength and the gas density in the form of the ratio E/N. Thus, the Boltzmann equation can be written in the following form:

$$\frac{d}{d\varepsilon}\left\{\left[\frac{e^2}{3}\left(\frac{E}{N}\right)^2\frac{\varepsilon}{q_A(\varepsilon)(1-\chi)+q_M(\varepsilon)\chi}\right.\right.$$
$$\left.+T\varepsilon^2\left(\frac{2m}{M_A}q_A(\varepsilon)(1-\chi)+\frac{2m}{M_M}q_M(\varepsilon)\chi\right)\right]\frac{df_0}{d\varepsilon}$$
$$\left.+\varepsilon^2\left(\frac{2m}{M_A}q_A(\varepsilon)(1-\chi)+\frac{2m}{M_M}q_M(\varepsilon)\chi\right)f_0(\varepsilon)\right\} \quad (1)$$
$$+\chi\sum_i S_i(q_i(\varepsilon)+q_{-i}(\varepsilon))\varepsilon f_0(\varepsilon)$$
$$=\chi\sum_i S_i((\varepsilon+\varepsilon_i)q_i(\varepsilon+\varepsilon_i)f_0(\varepsilon+\varepsilon_i)$$
$$+(\varepsilon-\varepsilon_i)q_{-i}(\varepsilon-\varepsilon_i)f_0(\varepsilon-\varepsilon_i)),$$

where $q_A(\varepsilon)$ and $q_M(\varepsilon)$ are the known transport cross sections for the elastic scattering of electrons on Xe atoms and H_2 molecules, respectively [7]; M_A and M_M are the masses of atoms and molecules, respectively; $q_i(\varepsilon)$ is the cross section of inelastic collisions of type I in which electrons lose the energy ε_i; and $q_{-i}(\varepsilon)$ is the cross section of inelastic collisions of type II in which electrons gain the energy ε_i. We will take into account the following inelastic processes: (i) excitation of the rotational levels of H_2 molecules with the rotational quantum numbers J: 0 ⟶ 2, 1 ⟶ 3, 2 ⟶ 4, and 3 ⟶ 5; (ii) type II impacts with J: 2 ⟶ 0, 3 ⟶ 1, 4 ⟶ 3, and 5 ⟶ 3; and (iii) excitation of the vibrational level with the vibrational quantum number V: 0 ⟶ 1.

The cross sections for the excitation of molecular rotations and for type II impacts are given by the Gerjuoy–Stein formula [8]. Threshold energies for the rotational transitions were as follows: $\varepsilon_{02} = 0.0434$ eV, $\varepsilon_{13} = 0.0727$ eV, $\varepsilon_{24} = 0.107$ eV, and $\varepsilon_{35} = 0.138$ eV. The statistical factor S_i determining populations of the rotational states J of hydrogen molecules can be written as [9]

$$S_J = \frac{p_J\exp(-E_J/kT)}{\sum_J p_J\exp(-E_J/kT)},$$

where $p_J = (2t+1)(t+a)(2J+1)$ are the statistical weights, t is the nuclear spin ($t = 1/2$ for H_2), and $a = 0$ and 1 for the even and odd J, respectively. The electron impact excitation of the vibrational degrees of freedom is characterized by a much higher threshold: $\varepsilon_V = 0.52$ eV. These cross sections are tabulated [7] as functions of the electron energies and cannot be approximated in terms of elementary functions.

Equation (1) was numerically solved using an algorithm proposed by Dyatko *et al.* [10]. The obtained electron energy distribution functions $f_0(\varepsilon)$ were used to calculate the electron drift velocities, mobilities, and transverse diffusion coefficients for $E/N \le 4$ Td and any hydrogen concentration in Xe–H_2 mixtures. Figure 1 shows calculated plots of the drift velocity versus E/N in comparison with the available experimental data. As can be seen, even small (a fraction of a percent) hydrogen additives lead to a severalfold increase in the drift velocity of hot electrons. We have performed calculations for very small molecular impurity concentrations in order to estimate the minimum amount of H_2 influencing the electron transport properties in gaseous xenon. The estimated minimum amount of the molecular additive is $\chi_{min} = 0.01\%$.

An analysis of the results of numerical calculations and the structure of the Boltzmann equation (1) showed that the electron transport characteristics (mobilities, mean and characteristic energies, diffusion coefficients) in gas mixtures with small fractions of the molecular impurity obey a similarity rule with respect to the parameter $E/(N\chi\sqrt{1-\chi})$ [11]. This implies that the values of transport coefficients (varying with the impurity content χ for a fixed E/N) fit to the same curve plotted as a function of the similarity parameter $E/(N\chi\sqrt{1-\chi})$. This rule is illustrated in Fig. 2, where the calculated electron mobilities and transverse diffusion coefficients in Xe–H_2 mixtures with various hydro-

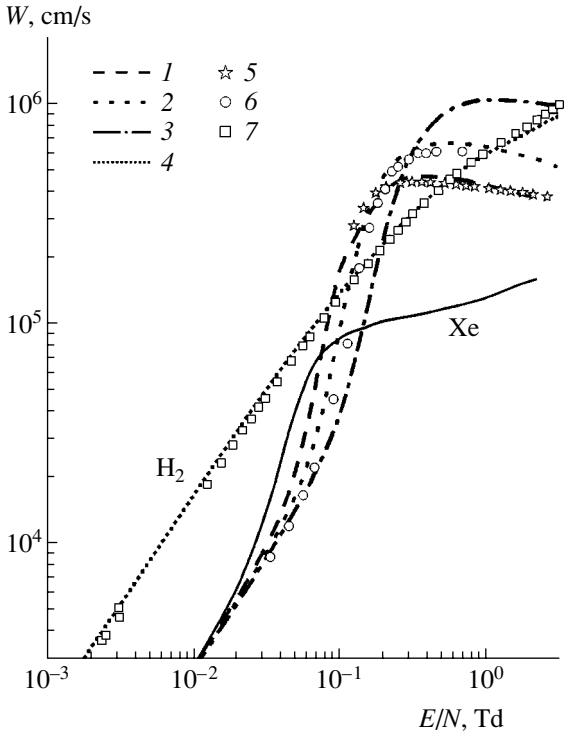

Fig. 1. Plots of the drift velocity versus E/N calculated for Xe–H_2 mixtures with H_2 concentrations of 0.46 (*1*), 1 (*2*), 3 (*3*), and 100% (*4*) in comparison with relevant experimental data reported in [4] (*5*), [3] (*6*), and [5] (*7*); solid curve shows the results of calculations for pure xenon.

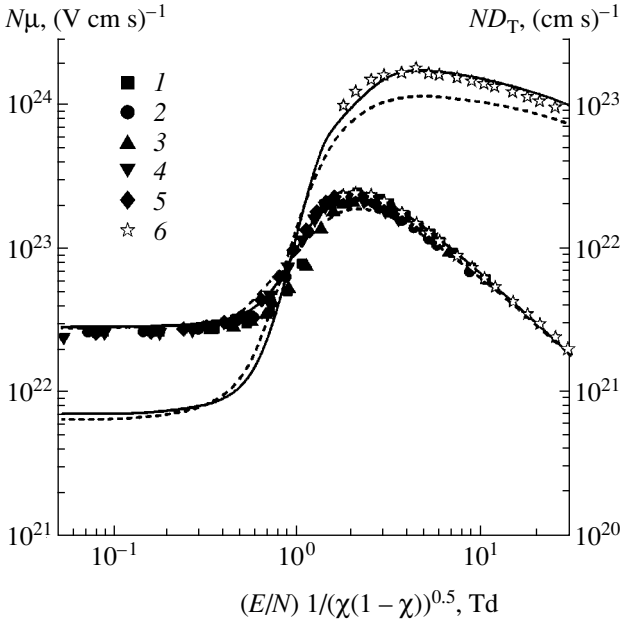

Fig. 2. Universal plots of the electron mobilities and transverse diffusion coefficients versus the reduced parameter $E/N\sqrt{\chi(1-\chi)}$ calculated for Xe–H_2 mixtures with H_2 concentrations of 1 (solid curve) and 4% (dashed curve) in comparison with the experimental data for (*1*) 0.4% H_2, (*2*) 0.6% H_2, (*3*) 1% H_2, (*4*) 1.6% H_2, (*5*) 2% H_2 (all from [3]), and (*6*) 0.46% H_2 [4].

gen concentrations are plotted in comparison with the available experimental data. As can be seen, the values of $N\mu(E/(N\chi\sqrt{1-\chi}))$ and $ND_T(E/(N\chi\sqrt{1-\chi}))$ concentrate at the universal curves. Deviations from the similarity curves are observed for $\chi > 0.04$ (4%). This upper boundary is determined by the ratio of cross sections of the elastic electron scattering on atoms and molecules.

In concluding, it should be noted that the results of our investigation allow the values of the electron transport coefficients to be determined with sufficiently high accuracy in a broad range of conditions (gas density N, field strength E, molecular admixture fraction χ) for which experimental data are not available. These data are very important for developing gamma spectrometers based on high-pressure ionization chambers filled with xenon.

Acknowledgments. This study was supported by the Russian Foundation for Basic Research (project no. 03-02-16451) and by the Presidential Grant for Support of Young Scientists and Leading Scientific Schools in the Russian Federation (project no. NSh-1953.2003.2).

REFERENCES

1. K. F. Vlasik, V. M. Gratchev, V. V. Dmitrenko, *et al.*, Instrum. Exp. Tech. **42** (5), 114 (1999).
2. L. G. Christophorou, D. V. Maxey, D. L. McCorkle, *et al.*, Nucl. Instrum. Methods **171**, 4913 (1980).
3. A. V. Kirilenkov, S. P. Konovalov, S. V. Murav'ev, *et al.*, Preprint No. 149, FIAN (Lebedev Physical Institute, Academy of Sciences of USSR, Moscow, 1981).
4. M. T. Elford, S. Sasaki, and K. F. Ness, Aust. J. Phys. **47**, 253 (1994).
5. J. A. Dutton, J. Phys. Chem. Ref. Data **4**, 577 (1975).
6. V. L. Ginzburg and A. V. Gurevich, Usp. Fiz. Nauk **50**, 201 (1960) [Sov. Phys. Usp. **3**, 115 (1960)].
7. S. Trajmar, D. F. Register, and A. Chutjian, Phys. Rep. **97**, 219 (1983).
8. E. Gerjuoy and S. Stein, Phys. Rev. **97**, 1671 (1955); **98**, 1848 (1955).
9. L. S. Frost and A. V. Phelps, Phys. Rev. **127**, 1621 (1962).
10. N. A. Dyatko, I. V. Kochetov, A. D. Napartovich, *et al.*, Preprint No. IAE-3842/12 (Kurchatov Institute of Atomic Energy, Moscow, 1983).
11. V. M. Atrazhev, I. V. Chernysheva, E. V. Davydovskaya, *et al.*, in *Proceedings of the International Seminar "High Pressure Xenon," Scientific Session MIFI-2003* (MIFI, Moscow, 2003), Vol. 7, p. 200.

Translated by P. Pozdeev

Technical Physics Letters, Vol. 30, No. 4, 2004, pp. 304–306. Translated from Pis'ma v Zhurnal Tekhnicheskoĭ Fiziki, Vol. 30, No. 8, 2004, pp. 1–6.

Photoelectron Emission Caused by Surface Plasmons in Silver Nanoparticles

É. L. Nollé* and M. Ya. Shchelev

Prokhorov Institute of General Physics, Russian Academy of Sciences, Moscow, 117924 Russia

** e-mail: nolle@ran.gpi.ru*

Received October 3, 2003

Abstract—A new intense band of photoelectron emission peaked at a wavelength of 490 nm has been observed in granular silver films with a nanoparticle size of 10–50 nm. Coinciding with an optical reflection band, the new photoelectron emission peak is related to the excitation of surface plasmons in silver nanoparticles. The quantum yield of photoemission (0.25%) for the new band is approximately equal to that for a longwave band of the classical silver–oxygen–cesium photocathode. It is demonstrated that the photoelectron emission from both photoemitters has a common nature and a time constant on the order of several femtoseconds can be obtained. © *2004 MAIK "Nauka/Interperiodica".*

As is known [1], a maximum of the band of photoelectron emission (PEE) from thin silver (Ag) films activated in cesium (Cs) vapor falls within the ultraviolet spectral region ($\lambda \approx 350$ nm) and the intensity of this band strongly depends on the Ag film thickness and structure. It was demonstrated [2] that the PEE intensity in this band increases approximately by one order in magnitude when the Ag film activated in Cs has a granular (rather than continuous) structure, consisting of Ag nanoparticles with a grain size from 10 to 50 nm. This increase is explained by the fact that the PEE process at $\lambda \approx 350$ nm is related to the excitation of surface plasmons, which sharply increases in nanoparticles due to the dimensional effects [3]. The plasma resonance frequency in solids is proportional to the charge carrier density N and inversely proportional to the dielectric permittivity ε and the effective mass m^* of carriers: $\omega_p = (4\pi Nq^2/m^*\varepsilon)^{1/2}$. Metal nanoparticles may feature enhanced plasma resonance at the main frequency and exhibit additional resonances at lower frequencies caused by a change in the dielectric permittivity of a finely dispersed medium. The low-frequency resonances can be related, for example, to an oblate shape of Ag nanoparticles (as manifested in their absorption spectra [4]) or to the presence of two populations of nanoparticles of different size (manifested in the reflection spectra [2]).

This paper reports on the PEE caused by a low-frequency plasma resonance due to the size effects in silver nanoparticles.

The preparation of thin granular Ag films, their activation with Cs and oxygen (O), the measurements of the PEE quantum yield and optical reflection spectra, and the surface composition analysis were performed in an ultrahigh vacuum (10^{-10} Torr) setup (Riber, France) with Auger electron spectroscopy (AES) and X-ray photoelectron spectroscopy (XPS) facilities. Granular Ag films were prepared on thin amorphous underlayers of aluminum oxide, which provided electric contact with Ag nanoparticles by means of the tunneling effect. First, thick (100 nm) aluminum layers were deposited onto glass substrates and then kept in air for one day, which resulted in the formation of an approximately 3-nm-thick amorphous aluminum oxide film. Then, thin (7 nm) Ag films were deposited onto the surface of aluminum oxide in the Riber setup and the samples were heated in vacuum for 20 min at $T \approx 300$°C. According to [2], this treatment leads to the formation of a granular Ag film with nanoparticle dimensions from 10 to 50 nm. Finally, the granular Ag films were activated with Cs and O by a conventional method developed for the negative electron affinity semiconductor photocathodes [5]. The activation procedure consists in Cs deposition followed by repeated cycles of O deposition without switching off the Cs source. This treatment, ensuring a more pronounced decrease in the vacuum energy level compared to that achieved by the activation with Cs alone [2], allowed us to observed the PEE related to a low-frequency plasma resonance.

The measurements of PEE and the reflection spectra were performed using an unpolarized light beam incident at 45° onto the sample surface. In the wavelength range studied (400–800 nm), the PEE quantum yield $Q(\lambda)$ of Cs-activated continuous 20-nm-thick Ag films increased with decreasing λ (Fig. 1, curve *4*). In the region of $\lambda < 430$ nm, the Q value exhibited a sharp growth related [2] to the PEE due to the main plasma resonance with a maximum at $\lambda \approx 350$ nm. A single admission of oxygen after Cs activation led to a decrease in the Q value. In contrast, repeated switching of the oxygen source on and off after the initial Cs treatment allowed the maximum PEE quantum yield to be reached. After such a cyclic treatment with oxygen, the

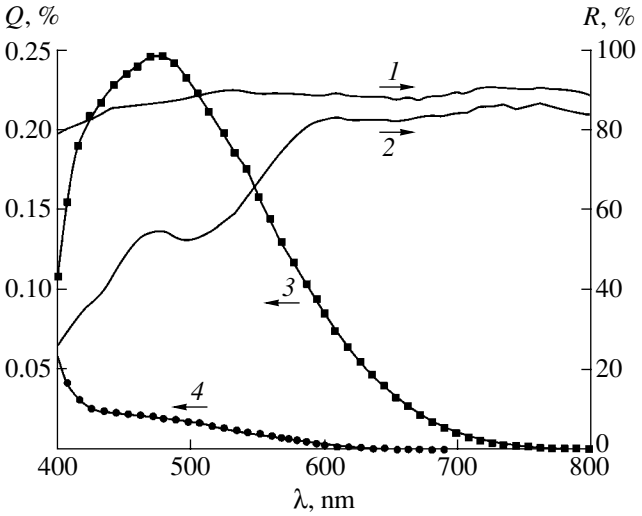

Fig. 1. The spectra of (*1*, *2*) reflection coefficient *R* and (*3*, *4*) PEE quantum yield *Q* of (*2*, *3*) granular Ag films activated with Cs and O and (*1*, *4*) continuous Ag films activated with Cs.

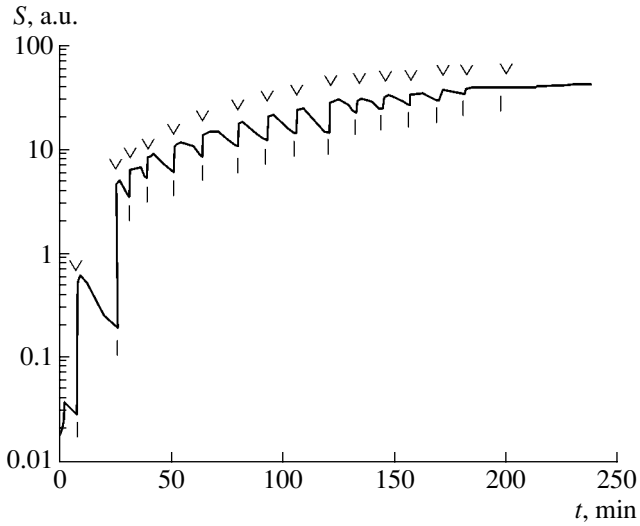

Fig. 2. A plot of the photosensitivity *S* of a granulated Ag film versus the time of activation with Cs and O. Symbols | and ∨ indicate the moments of oxygen source switching on and off.

value of *Q* increased one to three orders of magnitude compared to that upon the initial Cs activation (Fig. 2).

The PEE quantum yield spectrum of granular Ag films exhibited a new PEE band with a maximum at λ = 490 nm (Fig. 1, curve *3*). This peak was situated in the region of the minimum of a longwave reflection band (Fig. 1, curve *2*) observed for granular Ag films and absent in the reflection spectra of continuous films (curve *1*). The full width at half maximum of the PEE band was about Δ = 1 eV. The reflection spectra of granular Ag films also revealed the beginning of a band related to the enhanced main plasma resonance at $\lambda <$ 450 nm. The PEE spectra of such films did not show the beginning of the band due to the main plasma resonance because the deposition of oxygen in the course of activation of continuous films decreases the intensity of this PEE band. As was shown in [6], this is explained by dissipation of the energy of photoelectrons emerging into vacuum by tunneling via a potential barrier formed by the activation layer, the thickness of which increases in the course of cyclic oxygen deposition. As a result, the shortwave PEE decreases, while the longwave PEE from the states of lower energy increases as a result of decrease in the electron work function φ. The PEE quantum yield from granular Ag films at λ = 490 nm reaches *Q* = 0.25%, which is more than ten times the *Q* value for continuous films.

The appearance of a new intense PEE band in the granular Ag films activated with Cs and O, which is peaked at λ = 490 nm and coincides with a band of longwave plasma resonance reflection, indicates that this PEE is related to the excitation of surface plasmons in Ag nanoparticles. It should be noted that the spectral position of this band coincides with that of a band in the absorption spectrum [4] of plasmons excited in oblate spheroidal Ag nanoparticles prepared by a method analogous to that used in this study. Investigation of the reflection spectra [2] showed that the position of the longwave plasma resonance band depends on the temperature of annealing of thin Ag films upon deposition. As the annealing temperature (influencing the size of Ag nanoparticles) decreases, the plasma resonance band shifts toward longer wavelength and approaches λ = 700–800 nm, corresponding to the maximum PEE quantum yield of $Q \approx 0.3\%$ observed for a silver–oxygen–cesium (Ar–O–Cs) photocathode [1].

We have studied by AES and XPS the surface compositions of the granular Ag films activated with Cs and O, Ag–O–Cs photocathodes, and negative electron affinity photocathodes with Schottky barriers. The results of this investigation showed that the surface compositions of these photoemitters are identical. In the negative electron affinity photocathodes, a decrease in the electron work function φ upon the activation with Cs and O is caused to the formation of a thin (~1 nm) dipole layer involving dipoles of Cs^+ ions and Cs–O–Cs. Therefore, a decrease in the φ value in the case of granular Ag films can also be related to the appearance of an analogous layer upon activation.

The PEE from granular Ag films activated with Cs and O can be considered as the photoemission from a two-dimensional Ag–O–Cs photocathode. In such a photocathode, the surface of Ag nanoparticles with dimensions about 10–50 nm occurring on a thin Al_2O_3 substrate is surrounded by a layer of Cs^+ ion dipoles decreasing the electron work function to $\varphi \approx 2$ eV and by a thicker layer of Cs–O–Cs dipoles further reducing this value to $\varphi \approx 1$ eV. The results of investigations show that the longwave PEE band in such photocathodes is related to the excitation of surface plasmons in

Ag nanoparticles, while the spectral position of this band apparently depends on the size, shape, and distribution of these nanoparticles. In the known photocathodes, the PEE is due to a bulk three-stage external photoelectric process involving photoelectron generation, transport to the surface, and escape into vacuum. The characteristic time constant of such photocathodes is determined by the transport of photoelectrons to the emitter surface [1, 5].

In our two-dimensional photoemitter, we deal with a surface photoelectric process determined by the excitation of surface plasmons and, hence, the stage of photoelectron transport is missing. Therefore, the time constant t can be significantly smaller compared to that in the conventional photocathodes. In the two-dimensional photoemitter studied, the t value is determined by the time of plasma wave propagation through a nanoparticle. For Ag nanoparticles with an average size of $d \approx 10$ nm, this time can be estimated as $t = d/2v_F \approx 5$ fs, where $v_F \approx 10^6$ m/s is the electron velocity on the Fermi surface. The small relaxation time of the plasma wave is confirmed by a large width of the surface plasmon band reaching $\Delta \approx 1$ eV (Fig. 1).

Acknowledgments. This study was supported by the Presidium of the Russian Academy of Sciences within the framework of the "Low-Dimensional Quantum Structures" Program (project no. 4.12).

REFERENCES

1. A. H. Sommer, *Photoemissive Materials* (Wiley, New York, 1968; Énergiya, Moscow, 1973).
2. F. Sabary and J. C. Dudek, Vacuum **41**, 476 (1990).
3. S. G. Tikhodeev, A. L. Yablonskii, E. A. Muljarov, *et al.*, Phys. Rev. B **66**, 045102 (2002).
4. S. W. Kennerly, J. W. Little, R. J. Warmack, *et al.*, Phys. Rev. B **29**, 2926 (1984).
5. R. L. Bell, *Negative Electron Affinity Devices* (Clarendon Press, Oxford, 1973; Énergiya, Moscow, 1978).
6. É. L. Nollé, Fiz. Tverd. Tela (Leningrad) **31**, 225 (1989) [Sov. Phys. Solid State **31**, 1965 (1989)].

Translated by P. Pozdeev

Technical Physics Letters, Vol. 30, No. 4, 2004, pp. 307–308. Translated from Pis'ma v Zhurnal Tekhnicheskoĭ Fiziki, Vol. 30, No. 8, 2004, pp. 7–11.

On the Possibility of Using Indium Nitride in Thermophotovoltaic Converters

S. V. Shutov and E. S. Appazov*

Kherson State Technical University, Kherson, Ukraine

** e-mail: eappazov@yandex.ru*

Received August 12, 2003

Abstract—The efficiency of thermophotovoltaic converters employing indium nitride (InN) has been evaluated. The results of calculations show that InN based converters are advantageous over the conventional GaSb devices under the conditions of operation at elevated temperatures. © *2004 MAIK "Nauka/Interperiodica".*

A true value reported quite recently [1, 2] for the bandgap width of indium nitride, which had been previously considered as a typical wide-bandgap semiconductor, allowed the revision of the possible fields of application of this material. Since the bandgap width of InN has proved to be much lower ($E_g \approx 0.7$ eV at 300 K) than that accepted previously, we may expect that this material can be used in effective radiation detectors for the IR range.

This Letter is devoted to evaluation of the efficiency of InN based thermophotovoltaic (TPV) converters. It should be noted that experimental data available on the optical and electric properties of InN refer mostly to that period when this material was treated as a wide-bandgap semiconductor. For this reason, our calculations were performed within the framework of a general thermodynamic approach successfully used for evaluation of the limiting efficiency of solar cells [3].

The efficiency of a TPV converter was defined by the formula

$$\eta = \frac{E_{max} I_{ph}}{q E_c},$$

where

$$E_{max} \approx q\left(U_{id} - \frac{AkT}{q}\ln\left[\frac{qU_{id}}{AkT} + 1\right] - \frac{AkT}{q}\right);$$

$$U_{id} \approx \frac{AkT}{q}\ln\left(\frac{I_{ph}}{I_0}\right)$$

and U_{id} is the idle duty voltage. A model source of IR radiation was the blackbody with the ideal selective filter reflecting all photons with $h\nu < E_g$. The total surface radiation density E_c and the photocurrent I_{ph} were determined from the spectral density of photons $dn_{ph}/d(h\nu)$ of the model source (Fig. 1, curve *1*). The saturation current I_0 was determined as [4]

$$I_0 = \frac{q(n^2 + 1)E_g^2 kT}{4\pi^2 \hbar^3 c^2}\exp\left(\frac{-E_g}{kT}\right).$$

It was assumed that the absorption of each photon with an energy in the interval $E_g \le h\nu \le E_g + 0.1$ eV leads to the production of a conduction electron, while photons with the energies $h\nu > E_g + 0.1$ eV are absorbed by the crystal lattice with an increase in the semiconductor temperature. For comparison, we have used the same model to perform calculations for a converter based on GaSb, a material widely and successfully used in TPV converters. The curves of relative thermal losses in TPV converters versus blackbody temperature for InN and GaSb are presented in Fig. 1 (curves *3* and *2*, respectively).

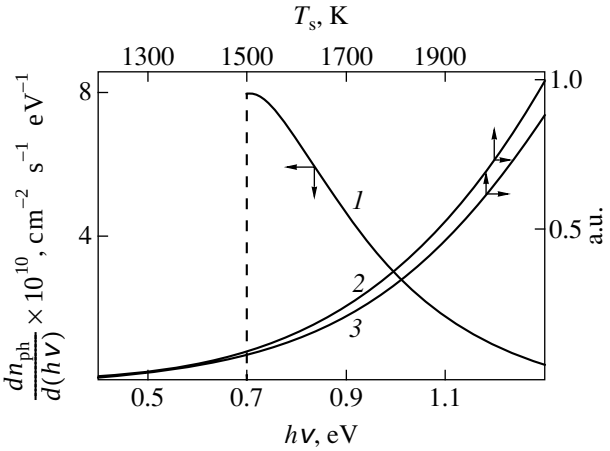

Fig. 1. The spectral distribution of the photon flux density for a model source with $T_s = 1973$ K (*1*); the fraction of the source radiation spent for thermal losses versus blackbody temperature for TPV converters based on (*2*) GaSb and (*3*) InN.

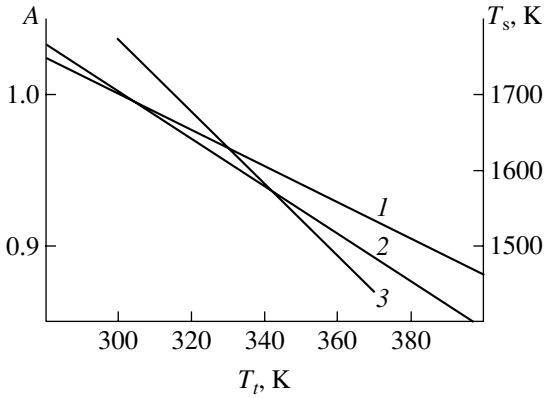

Fig. 2. Plots of (*1*, *2*) the efficiency A (normalized to the value at 300 K) of TPV converters based on InN and GaSb, respectively, and (*3*) the T_t value versus source temperature T_s.

The operation of TPV converters under real conditions involves increased energy flux densities analogous to those encountered in solar cells—converters of concentrated solar radiation. For this reason, we adopted the approach to determining the contributions of various parameters to the temperature dependence of the TPV conversion efficiency developed in [5]. According to this, the temperature dependence of η is, in the first approximation, fully determined by the character of variation of the function $dU_{id}/dt = (E_g - U_{id})/T$. It was also assumed that the values of $E_g(T)$ for both GaSb and InN are constant in the temperature interval from 300 to 400 K (no data on $E_g(T)$ of InN are available at present). This assumption does not influence the character of $\eta(T)$: a decrease in the semiconductor bandgap width with increasing TPV temperature leads to an insignificant change in the photocurrent I_{ph}, which is almost completely compensated by the corresponding growth of I_0. The calculations were performed for the following parameters: $A = 1.5$; $E_{gGaSb}^{300\ K} = 0.70$ eV; $E_{gInN}^{300\ K} = 0.72$ eV; $n_{GaSb} = 3.79$ [6]; $n_{InN} = 2.0$ [7].

Figure 2 shows the temperature dependences of the conversion efficiency (normalized to that at 300 K) calculated using the above model with a source temperature of $T_s = 1973$ K for TPV converters based on InN and GaSb. As can be seen, the $\eta(T)$ value for InN does not vary as strongly with the temperature as does that for GaSb. This is an important result, since an increase in T_s gives rise to the fraction of photons absorbed in the TPV crystal without the production of charge carriers participating in the photocurrent (this fraction is always greater for GaSb than for InN: cf. curves *2* and *3* in Fig. 1). A TPV converter based on GaSb will be heated to a greater extent, since the thermal conductivity of this material is lower than that of InN ($\kappa = 0.35$ W/(cm K) [5] versus 0.45 W/(cm K) [7], respectively). The thermal conductivity of sapphire (usual substrate material for the epitaxial growth of InN) amounts to ~1.0 W/(cm K) [8]. By comparing of the efficiencies of TPV converters based on InN and GaSb at various temperatures, we determined the temperatures T_t above which the absolute efficiency of the InN based converter exceed that of the GaSb based device in the temperature interval studied. The plot of $T_t = f(T_s)$ is also presented in Fig. 2.

In conclusion, it should be noted that the observed behavior of $\eta(T)$ qualitatively agrees with the results of other researchers (see, e.g., [9]) and does not contradict published experimental data [10]. On the whole, the results of our calculations show that TPV converters based on InN are advantageous at elevated temperatures.

REFERENCES

1. V. Yu. Davydov, A. A. Klochikhin, V. V. Emtsev, *et al.*, Phys. Status Solidi B **233**, R10 (2002).
2. V. Yu. Davydov, A. A. Klochikhin, V. V. Emtsev, *et al.*, Phys. Status Solidi B **234**, 787 (2002).
3. V. M. Andreev, V. A. Grikhiles, and V. D. Rumyantsev, *Photoelectric Conversion of Concentrated Solar Radiation* (Nauka, Leningrad, 1989).
4. C. H. Henry, J. Appl. Phys. **51**, 4494 (1980).
5. J. C. G. Fan, Sol. Cells **17**, 309 (1986).
6. *Handbook on Electrotechnical Materials*, Ed. by Yu. V. Koritskiĭ, V. V. Pasynkov, and B. M. Tareev (Énergoatomizdat, Leningrad, 1988).
7. V. A. Tyagaĭ, A. M. Evstigneev, A. N. Krasiko, *et al.*, Fiz. Tekh. Poluprovodn. (Leningrad) **11**, 2142 (1977) [Sov. Phys. Semicond. **11**, 1257 (1977)].
8. S. Krukowski, A. Witek, J. Adamchyk, *et al.*, Phys. Chem. Solids **59**, 289 (1998).
9. J. Luther, G. Stollwerck, and M. Zenker, in *Proceedings of the 10th Workshop on Quantum Solar Energy Conversion (QUANTSOL-98), Bad Hofgastein, 1998*; http://www.esqsec.unibe.ch/pub_22.htm.
10. I. Ballard, K. W. J. Barnham, J. Nelson, *et al.*, in *Proceedings of the 2nd World Conference and Exhibition on Photovoltaic Solar Energy Conversion, Vienna, 1998*, pp. 3624–3628.

Translated by P. Pozdeev

Technical Physics Letters, Vol. 30, No. 4, 2004, pp. 309–312. Translated from Pis'ma v Zhurnal Tekhnicheskoĭ Fiziki, Vol. 30, No. 8, 2004, pp. 12–19.

The Laws of Plane Defect Wave Propagation across the Interface between Two Viscoplastic Media

N. V. Chertova* and Yu. V. Grinyaev

Institute of Strength Physics and Materials Science, Siberian Division, Russian Academy of Sciences, Tomsk, 634055 Russia

** e-mail: chertova@ms.tsc.ru*

Received June 18, 2003

Abstract—Relations determining the laws of reflection and refraction of a plane wave in the defect field at an interface between two viscoplastic media are obtained based on the dynamic equations of the continuum theory of defects. The reflection and transmission coefficients relating the amplitudes of reflected and transmitted waves to the incident wave amplitude are determined. The obtained relations are applied to a particular case of media with weakly decaying waves. *© 2004 MAIK "Nauka/Interperiodica".*

Previously [1, 2] the laws of propagation of plane defect waves and the structure of these waves in a viscoplastic medium were considered based on defect field theory. In a continuation of that analysis, let us take into account processes at an interface between two such media. Numerous results [3–5] show evidence of a special role of interfaces in the process of deformation. Hence, studying the behavior of loaded materials in the presence of interfaces is an important problem of the mechanics of deformed bodies.

As was demonstrated in [1, 2], the field of defects in a viscoplastic medium obeying the relation

$$\sigma = \eta I \tag{1}$$

satisfies the following system of dynamic equations of the defect field theory,

$$\begin{gathered} \nabla \cdot \hat{I} = 0, \quad \nabla \cdot \hat{\alpha} = 0, \\ \frac{\partial \hat{\alpha}}{\partial t} = \nabla \times \hat{I}, \quad S(\nabla \times \hat{\alpha}) = -B\frac{\partial \hat{I}}{\partial t} - \hat{\sigma}, \end{gathered} \tag{2}$$

written in terms of the line vectors $\hat{I}_i = [I_{ix}, I_{iy}, I_{iz}]$, $\hat{\alpha}_i = [\alpha_{ix}, \alpha_{iy}, \alpha_{iz}]$, and $\hat{\sigma}_i = [\sigma_{ix}, \sigma_{iy}, \sigma_{iz}]$ of the corresponding tensors. Here, η is the tensor of viscosity coefficients, α is the defect density tensor, I is the defect flux density tensor, and σ is the effective stress tensor; B and S are constant quantities; and signs $(\cdot)$ and $(\times)$ denote the scalar and vector product, respectively.

In order to uniquely determine characteristics of the defect field proceeding from preset initial values, the above equations have to be supplemented by the boundary conditions formulated in the usual way [6]. We assume that the normal $(\hat{I}_n, \hat{\alpha}_n)$ and tangential $(\hat{I}_t, \hat{\alpha}_t)$ components of characteristics of the defect field at the interface satisfy the following conditions:

$$\begin{gathered} \hat{I}_n^1 - \hat{I}_n^2 = 0, \quad \hat{\alpha}_n^1 - \hat{\alpha}_n^2 = 0, \\ \hat{I}_t^1 - \hat{I}_t^2 = 0, \quad S_1\hat{\alpha}_t^1 - S_2\hat{\alpha}_t^2 = 0. \end{gathered} \tag{3}$$

Let the interface between two homogeneous media to coincide with the plane $z = 0$ in the Cartesian coordinate system. Media occupying the upper ($z > 0$) and lower ($z < 0$) half-spaces are characterized by the sets of parameters B_1, S_1, η_1 and B_2, S_2, η_2, respectively. Consider a plane wave with frequency ω and the wave vector $K_0 = k_1 m_0$ ($k_1 = \omega/V_1$ (where m_0 is the unit vector of the normal to the wave front) incident from the first (upper) medium onto the interface at an angle of θ_0 relative to the z axis (Fig. 1). Let the plane of incidence containing vector K_0 and the z axis coincide with the xz plane. Denoting the wave vectors of the reflected and

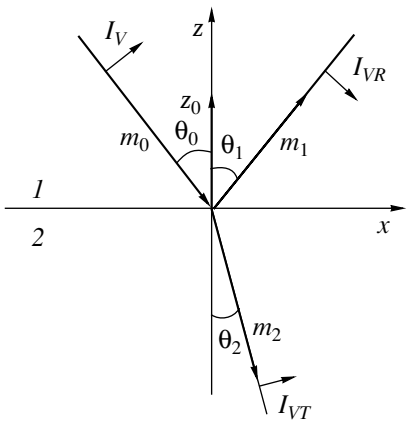

Fig. 1. The geometry of reflection and transmission of a plane wave at the interface between two media.

1063-7850/04/3004-0309$26.00 © 2004 MAIK "Nauka/Interperiodica"

transmitted waves by $K_1 = k_1 m_1$ and $K_2 = k_2 m_2$, respectively, and introducing the unit vector z_0 of the normal to the interface, the defect field can be written as follows [1, 2]. For the incident wave,

$$\begin{aligned} \hat{I} &= \hat{I}_0 \exp(-i\omega t + ik_1 m_0 r), \\ \hat{\alpha} &= \lfloor m_0 \hat{I}_0 \rfloor Z_1 \exp(-i\omega t + ik_1 m_0 r), \end{aligned} \tag{4}$$

for the reflected wave,

$$\begin{aligned} \hat{I}_R &= \hat{I}_1 \exp(-i\omega t + ik_1 m_1 r), \\ \hat{\alpha}_R &= \lfloor m_1 \hat{I}_1 \rfloor Z_1 \exp(-i\omega t + ik_1 m_1 r), \end{aligned} \tag{5}$$

and for the transmitted wave,

$$\begin{aligned} \hat{I}_T &= \hat{I}_2 \exp(-i\omega t + ik_2 m_2 r), \\ \hat{\alpha}_T &= \lfloor m_2 \hat{I}_2 \rfloor Z_2 \exp(-i\omega t + ik_2 m_2 r). \end{aligned} \tag{6}$$

Here, $Z_1 = 1/V_1$, $Z_2 = 1/V_2$, and V_1, V_2 are the wave propagation velocities given by the formulas (subscripts are omitted)

$$V = \sqrt{\frac{S}{B}/\left(1 + \frac{i\eta}{B\omega}\right)} = C/\sqrt{1 + i\tan\delta} = C/(n + i\chi),$$

where n and χ are the coefficients of refraction and absorption, respectively; $\tan\delta = \eta/B\omega$ is the loss tangent; and $C = \sqrt{S/B}$.

Writing boundary conditions (3) for the tangential components of the total wave field $\hat{\alpha}$ and $\hat{I}$ as

$$\begin{aligned} [z_0 I_0]\exp(iK_0 r) + [z_0 I_1]\exp(iK_1 r) &= [z_0 I_2]\exp(iK_2 r), \\ [z_0[m_0 I_0]]\exp(iK_0 r) + [z_0[m_1 I_1]]\exp(iK_1 r) &= \frac{S_2 Z_2}{S_1 Z_1}[z_0[m_2 I_2]]\exp(iK_2 r), \end{aligned} \tag{7}$$

we find that the phase factors must obey the relations

$$k_1 m_0 r|_{z=0} = k_1 m_1 r|_{z=0} = k_2 m_2 r|_{z=0}$$

or

$$k_1 \sin\theta_0 = k_1 \sin\theta_1 = k_2 \sin\theta_2.$$

From this it follows that the angle of reflection θ_1 is equal to the angle of incidence θ_0 (the law of reflection),

$$\theta_0 = \theta_1, \tag{8}$$

and the angles of refraction and incidence are related as (the law of refraction)

$$\frac{\sin\theta_2}{\sin\theta_0} = \frac{k_1}{k_2} = \frac{V_2}{V_1}. \tag{9}$$

In order to determine the amplitudes of the reflected and transmitted waves, let us return to Eqs. (7) and consider waves having two different linear polarizations: a horizontally polarized wave with the vector $\hat{I}$ having nonzero components perpendicular to the plane of incidence ($I_{xi} = I_{zi} = 0$, $I_{yi} \neq 0$) and a vertically polarized wave with the vector $\hat{I}$ having nonzero components in the plane of incidence ($I_{yi} = 0$, $I_{xi} \neq 0$, $I_{zi} \neq 0$). In the first case, the unknown amplitudes I_1, I_2 satisfy the equations

$$I_0 + I_1 = I_2, \quad S_1 Z_1 (I_0 - I_1)\cos\theta_0 = S_2 Z_2 I_2 \cos\theta_2. \tag{10}$$

Solving these equations, we obtain the coefficients relating the amplitudes of reflected and transmitted waves to that of the incident wave,

$$\begin{aligned} R_g &= R_\perp = \frac{S_1 Z_1 \cos\theta_0 - S_2 Z_2 \cos\theta_2}{S_1 Z_1 \cos\theta_0 + S_2 Z_2 \cos\theta_2}, \\ T_g &= T_\perp = \frac{2 S_1 Z_1 \cos\theta_0}{S_1 Z_1 \cos\theta_0 + S_2 Z_2 \cos\theta_2}, \end{aligned} \tag{11}$$

where $R_g = I_1/I_0$ and $T_g = I_2/I_0$. For the vertically polarized wave, the system of equations (7) yields

$$\begin{aligned} (I_0 - I_1)\cos\theta_0 &= I_2 \cos\theta_2, \\ S_1 Z_1 (I_0 + I_1) &= S_2 Z_2 I_2 \end{aligned} \tag{12}$$

and the coefficients relating the amplitudes of three waves (known in electrodynamics as the Fresnel coefficients [7]) appear as

$$\begin{aligned} R_v &= R_{\text{II}} = \frac{S_2 Z_2 \cos\theta_0 - S_1 Z_1 \cos\theta_2}{S_2 Z_2 \cos\theta_0 + S_1 Z_1 \cos\theta_2}, \\ T_v &= T_{\text{II}} = \frac{2 S_1 Z_1 \cos\theta_0}{S_2 Z_2 \cos\theta_0 + S_1 Z_1 \cos\theta_2}. \end{aligned} \tag{13}$$

Using relation (9), expressions (11) and (13) can be rewritten as functions of the angle of incidence. In particular, for the normal incidence ($\theta_0 = 0$),

$$R_g = \frac{S_1 Z_1 - S_2 Z_2}{S_1 Z_1 + S_2 Z_2} = -R_v.$$

Let us apply the general expressions (11) and (13) to analysis of a particular case of the interface between two media with weakly decaying waves, $\tan\delta_1 \ll 1$ and $\tan\delta_2 \ll 1$, whereby the ratio

$$\frac{V_2}{V_1} = \frac{C_2}{C_1}\sqrt{\frac{1 + i\tan\delta_1}{1 + i\tan\delta_2}} \cong \frac{C_2}{C_1} = \sqrt{\frac{S_2 B_1}{S_1 B_2}}$$

is real. The coefficients of reflection and refraction given by formulas (11)–(13) for $V_2/V_1 < 1$ are also real, so the phase shift between the incident and reflected waves is either zero or π. Figures 2a and 2b show the

reflection coefficients $R_g(\theta_0)$ and $R_v(\theta_0)$ for various ratios of the model parameters (such that $V_2/V_1 < 1$): (I) $S_1/S_2 > V_2/V_1$; (II) $S_1/S_2 = 1$; and (III) $S_1/S_2 < V_2/V_1$. The curves of $R_g(\theta_0)$ exhibit no singularities and cross zero only for $V_2/V_1 = 1$ and $S_1/S_2 = 1$, that is, for the two media with identical properties, whereby the interface disappears and reflection vanishes. The coefficient $R_v(\theta_0)$ can be alternatively expressed as

$$R_v = \frac{S_2\sin\theta_0\cos\theta_0 - S_1\sin\theta_2\cos\theta_2}{S_2\sin\theta_0\cos\theta_0 + S_1\sin\theta_2\cos\theta_2} = \frac{\tan(\theta_0-\varphi)}{\tan(\theta_0+\varphi)}.$$

Besides the points where $V_2/V_1 = 1$ and $S_1/S_2 = 1$, this expression exhibits an additional singularity at

$$\theta_0 + \varphi = \frac{\pi}{2}, \text{ where } \varphi = \frac{1}{2}\arcsin(S_1/S_2\sin 2\theta_2). \quad (14)$$

By jointly solving equations (9) and (14), we determine the angle of incidence

$$\theta_0^* = \arcsin\sqrt{[(V_2/V_1)^2 - (S_2/S_1)^2]/[(V_2/V_1)^4 - (S_2/S_1)^2]},$$

for which this singularity takes place. The angle θ_0^* corresponds to the total polarization, whereby an arbitrarily polarized wave incident at this angle will be reflected horizontally polarized.

Now, let the reflection take place at an interface between two media obeying the condition $V_2/V_1 > 1$, which, according to relation (9), implies that $\theta_2 > \theta_0$. Then, for $\sin\theta_0 > V_1/V_2$, the quantity

$$\cos\theta_2 = \sqrt{1-(V_2/V_1)^2\sin^2\theta_0} = \pm i\sqrt{(V_2/V_1)^2\sin^2\theta_0 - 1} \quad (15)$$

is imaginary. This case corresponds to the total internal reflection from the interface between two viscous media. The angle θ_0 satisfying the condition

$$\sin\theta_0 = \frac{V_1}{V_2} \quad (16)$$

is called the total internal reflection angle. In this case, $\sin\theta_2 = 1$ and the transmitted wave propagates parallel to the interface. Let us consider in more detail the structure of this wave for the angles equal to or greater than the limiting value. Using relation (15), the transmitted wave (6) can be expressed as

$$\hat{I}_T = \hat{I}_2\exp[-i(\omega t - k_1\sin\theta_0 x) - |z|k_2\sqrt{(V_2/V_1)^2\sin^2\theta_0 - 1}\,].$$

This expression describes a plane inhomogeneous wave with the phase varying along the x axis and the amplitude exponentially decaying along the z axis.

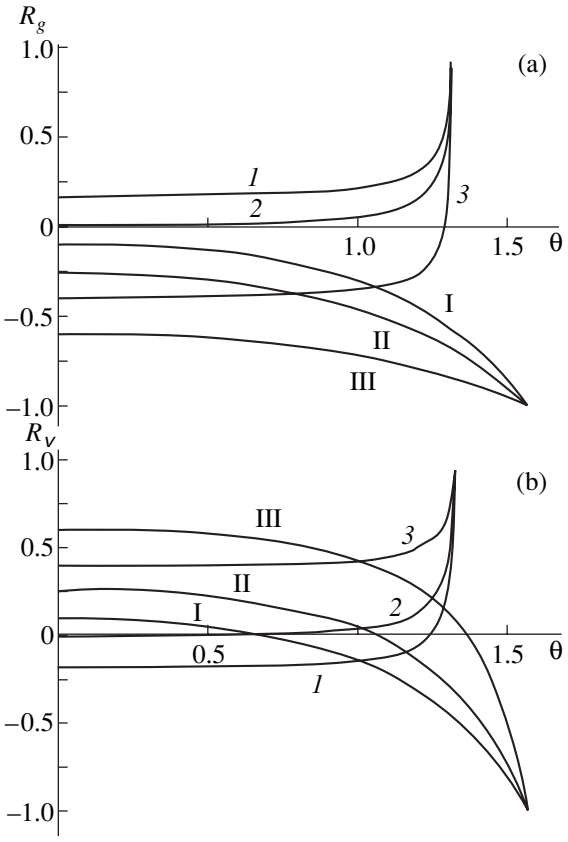

Fig. 2. Plots of the reflection coefficients (a) R_g and (b) R_v versus angle of incidence for (I–III) $V_2/V_1 = 0.6 < 1$ and (*1–3*) $V_2/V_1 = 1.033 > 1$: (I, *1*) $S_1/S_2 = 1.43$; (II, *2*) $S_1/S_2 = 1$; (III, *3*) $S_1/S_2 = 0.43$.

In Figs. 2a and 2b, curves *1–3* show the reflection coefficients $R_g(\theta_0)$ and $R_v(\theta_0)$ for $V_2/V_1 > 1$. As can be seen from formulas (11) and (13), the case of total internal reflection corresponds to $|R_g| = |R_v| = 1$, whereby the intensity of the reflected wave is equal to that of the incident wave for each component with horizontal or vertical polarization. The same formulas allow the phase change between the reflected and incident waves to be readily calculated as

$$\tan\frac{\delta_g}{2} = \frac{-\sqrt{(V_2/V_1)^2\sin^2\theta_0 - 1}}{S_1V_2/S_2V_1\cos\theta_0},$$

$$\tan\frac{\delta_v}{2} = \frac{-\sqrt{(V_2/V_1)^2\sin^2\theta_0 - 1}}{S_2V_1/S_1V_2\cos\theta_0}.$$

In conclusion, the main results can be formulated as follows. We have established the relations describing the laws of propagation of plane waves of a defect field

across the interface between two viscoplastic media (i.e., the laws of reflection and refraction of defect waves) and determined the corresponding reflection and transmission coefficients. It was demonstrated that certain relations between the characteristics of two media in contact makes possible the phenomena of total internal reflection and total polarization of the reflected wave. In the former case, the wave of the defect field and, hence, the plastic strain propagate along the interface and do not penetrate into the second medium. In the latter case, a wave incident at the angle θ_0^* and possessing arbitrary nonzero components is reflected with horizontal polarization, that is, has a nonzero component perpendicular to the plane of incidence.

Acknowledgments. This study was supported by the Russian Foundation for Basic Research, project no. 02-01-01188.

REFERENCES

1. N. V. Chertova and Yu. V. Grinyaev, Pis'ma Zh. Tekh. Fiz. **25** (18), 91 (1999) [Tech. Phys. Lett. **25**, 756 (1999)].
2. N. V. Chertova, Pis'ma Zh. Tekh. Fiz. **29** (2), 83 (2003) [Tech. Phys. Lett. **29**, 78 (2003)].
3. V. E. Panin, Fiz. Mezomekh. **2** (6), 5 (1999).
4. V. P. Alekhin, *The Physics of Strength and Plasticity of the Surface Layers of Materials* (Nauka, Moscow, 1983).
5. L. G. Orlov, Fiz. Tverd. Tela (Leningrad) **9**, 2345 (1967) [Sov. Phys. Solid State **9**, 1836 (1967)].
6. L. I. Sedov, *A Course in Continuum Mechanics* (Nauka, Moscow, 1976; Wolters-Noordhoff, Groningen, 1971–1972), Vol. 1.
7. J. A. Stratton, *Electromagnetic Theory* (McGraw-Hill, New York, 1941; Gostekhizdat, Moscow, 1948).

Translated by P. Pozdeev

Technical Physics Letters, Vol. 30, No. 4, 2004, pp. 313–315. Translated from Pis'ma v Zhurnal Tekhnicheskoĭ Fiziki, Vol. 30, No. 8, 2004, pp. 20–26.

Laser Doppler Chromatic Imaging of Rotating Structures

P. P. Belousov, P. Ya. Belousov, and Yu. N. Dubnishchev*

Institute of Thermal Physics, Siberian Division, Russian Academy of Sciences, Novosibirsk, Russia

** e-mail: dubnistchev@itp.nsc.ru*

Received July 30, 2003

Abstract—A method of the flow field velocity monitoring has been developed based on the laser Doppler imaging with chromatic selection of the velocity vector components in an orthogonal coordinate basis set.

Most important problems in the optical diagnostics of flows are related to the imaging and measurement of the flow velocity field. Laser Doppler anemometry techniques [1] are most suited for the measurement of a local flow velocity. The known methods of particle image velocimetry (PIV) [2] involve basic limitations related to the dependence of the results of measurements on the spatial and temporal frequencies of a probing set and, hence, on the concentration of calibrated particles introduced into the medium studied. There are many unresolved problems encountered in the processing and identification of particle tracks. These methodological and technical limitations cast doubt on the very possibility of using traditional PIV techniques for real-time imaging and measurement of flow velocity fields.

Previously [3], we developed a method for the online laser Doppler imaging and measurement of the flow velocity field. Based on the optical frequency demodulation of a light field, the proposed method was later called global laser velocimetry (GLV) [4]. Laser Doppler imaging of the velocity field of a swirling flow in the Rank–Hilsh vortex tube was reported for the first time in [5], where this technique confirmed the existence of double-helix vortices previously revealed by the method of Gilbert optics [6].

Recently [7], we proposed a possible solution to the problem of imaging and measurement of the flow velocity field in a three-dimensional coordinate basis set, based on a temporal selection of the velocity vector components and a linear transformation of the cross-sectional image frequency-demodulated in a coherent light. In this method, the frequency of switching of a light field forming the "laser sheet" is restricted to the Nyquist frequency related to the upper boundary of the power spectrum of the process studied. This Letter reports on the method of real-time imaging and measurement of a flow velocity field, which is free of the above limitation.

Figure 1 shows a schematic diagram of the experimental setup comprising a hydrodynamic device forming a swirling flow in a cylindrical channel and a laser Doppler system imaging the velocity flow field with chromatic selection of the velocity vector components in an orthogonal coordinate basis set. The measuring system employs an argon laser generating blue and green spectral lines. A dispersion prism splits the laser radiation into the blue and green beams. Past mirrors M_1 and M_2, anamorphic optical system (*AOS*), and mirror M_3, the blue beam is transformed into a blue laser sheet selecting an axial probed cross section in the transparent cylindrical channel with a water flow perturbed by the vortexer. By the same token, the green beam is transformed by an analogous anamorphic optical system and mirrors M_4–M_6 into a green laser sheet adjusted so as to coincide with the blue sheet. The light fields in the blue and green planes are oriented in the opposite directions,

$$\frac{\mathbf{k}_b}{k_b} = \frac{\mathbf{k}_g}{k_g},$$

where $\mathbf{k}_b$ and $\mathbf{k}_g$ are the wave vectors of the blue and green light fields, respectively. The laser sheets illuminate the selected cross section of the flow.

A bichromatic Doppler processor (BDP) with a coherent feedback is based on a semiconfocal optical cavity with a mode structure matched with that of the probing laser in the blue and green spectral regions. The transmission function of BDP for the blue and green laser emission lines has a resonance shape. A linear portion of the corresponding chromatic amplitude–frequency characteristic of BDP is used as the discrimination curve. The optical axis of BDP is orthogonal to the laser sheet. In the output plane, BDP forms an image of the selected cross section of the flow in a frequency-demodulated coherent light. The frequency-demodulated image is monitored by a CCD camera. After separation of the signal into RGB components, the G and B images are normalized to the corresponding chro-

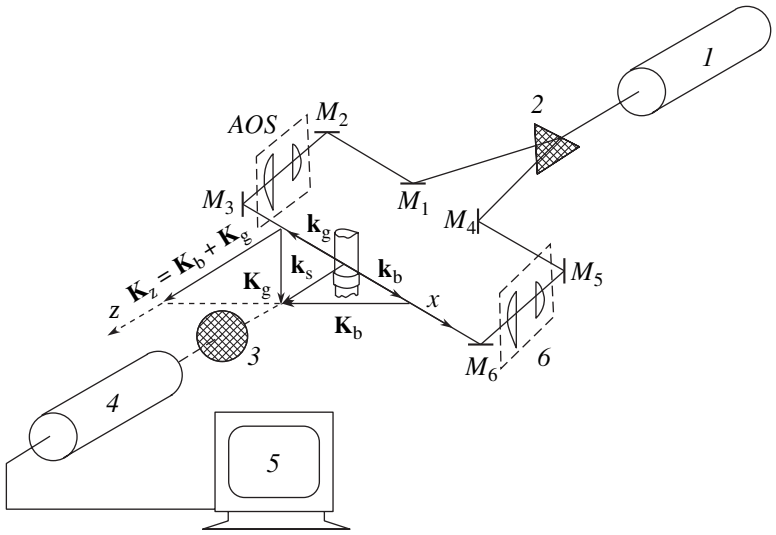

Fig. 1. Schematic diagram of the experimental setup: (*1*) laser; (*2*) prism; (*3*) objective lens; (*4*) optical processor; (*5*) personal computer; (*6*) anamorphic optical system.

matic images not subjected to frequency demodulation. The images are processed in a personal computer.

The light field intensity at each point of the image is a single-valued function of the projection of the velocity vector onto the direction of the sensitivity vector **K** equal to the difference of wave vectors of the scattered ($\mathbf{k}_s$) and incident ($\mathbf{k}_i$) light beams ($\mathbf{K} = \mathbf{K}_s - \mathbf{k}_i$). The two-dimensional (2D) coordinate basis set is formed by the vectors $\mathbf{K}_x$ and $\mathbf{K}_y$,

$$\mathbf{K}_x = \mathbf{K}_b - \beta\mathbf{K}_g;$$

$$\mathbf{K}_y = \mathbf{K}_b - \beta\mathbf{K}_g,$$

where $\mathbf{K}_b = \mathbf{k}_{bs} - \mathbf{k}_b$, $\mathbf{K}_g = \mathbf{k}_{gs} - \mathbf{k}_g$; $\mathbf{k}_{bs}$ and $\mathbf{k}_{gs}$ are the wave vectors of the blue and green scattered beams, respectively; $\mathbf{k}_b$ and $\mathbf{k}_g$ are the wave vectors of the blue and green laser sheet fields forming the spatially coinciding oppositely directed laser sheets; and $\beta = k_b/k_g$.

Indeed, the cross section probed by a light field with the wave vector $\mathbf{k}_b$ is imaged at the BDP output by a set of images of the scattering optical inhomogeneities $\varphi(\xi, \eta)\delta(x - \xi, y - \eta)$, where (ξ, η) are the coordinates of the optical inhomogeneities in the (x, y) plane of the cross section. Therefore, a frequency-demodulated image of the cross section selected by the blue laser sheet can be described as

$$\omega_{D1}(x, y) = \gamma\iint\mathbf{K}_b\mathbf{v}(\xi, \eta)\varphi(\xi, \eta)\delta(x - \xi, y - \eta)d\xi d\eta$$
$$= \gamma\mathbf{K}_b\mathbf{v}(x, y)\varphi(x, y),$$

where the integral is taken over the whole selected cross section, $\omega_{D1}(x, y)$ is the Doppler frequency shift of the blue light beam forming the point (x, y) in the image at the BDP output, $\mathbf{v}(x, y)$ is the velocity vector at the point (x, y), and γ is the slope of the BDP discrimination curve. The factor $\varphi(x, y)$ corresponds to the scattering function in the direction $\mathbf{K}_b$, which describes the primary image of the selected cross section (not subjected to frequency demodulation). Then, the function

$$\tilde{\omega}_{Db}(x, y) = \frac{\omega_{D1}(x, y)}{\gamma\varphi(x, y)} = \mathbf{K}_b\mathbf{v}(x, y)$$

describes a distribution of the relative intensity of the frequency-demodulated image. From this it follows that $\tilde{\omega}_{Db}(x, y)$ is a single-valued function of the velocity field component in the direction $\mathbf{K}_b$:

$$v_b(x, y) = \frac{1}{K_b}\mathbf{v}(x, y)\mathbf{K}_b. \quad (1)$$

By the same token, the velocity field component in the direction of the sensitivity vector $\mathbf{K}_g$ corresponding to the green spectral range of the probing laser is

$$v_g(x, y) = \frac{1}{K_g}\mathbf{v}(x, y)\mathbf{K}_g. \quad (2)$$

Equations (1) and (2) describe the fields of the color-selected velocity vector components in the orthogonal basis set formed by the sensitivity vectors $\mathbf{K}_b$ and $\mathbf{K}_g$. In order to pass to a 2D basis set with the x axis lying in the plane of the laser sheet and the z axis perpendicular to this plane, it is sufficient to apply a linear transforma-

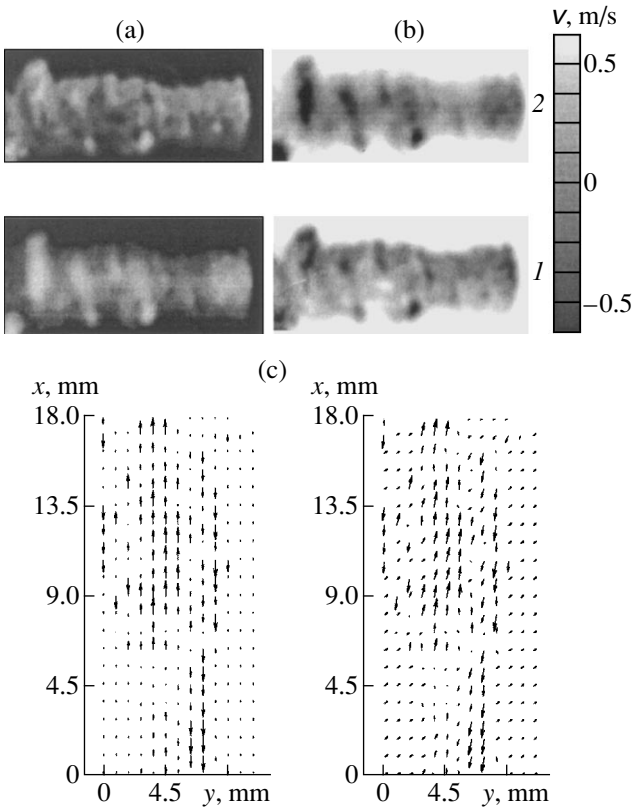

Fig. 2. Laser Doppler imaging of the velocity field of a swirling water flow: (a, b) images in the ($\mathbf{K}_b$, $\mathbf{K}_g$) and ($\mathbf{K}_x$, $\mathbf{K}_z$) coordinate basis sets in the (*1*) green and (*2*) blue laser sheet channels; (c) stereoscopic reconstruction of the 2D flow vector velocity field (for 3D perception, eyes should be accommodated to the infinity).

tion to the images $v_b(x, y)$ and $v_g(x, y)$. Subtracting and adding Eqs. (1) and (2) yields

$$v_b(x, y) - v_g(x, y) = \mathbf{v}(x, y)\left(\frac{\mathbf{K}_b}{K_b} - \frac{\mathbf{K}_g}{K_g}\right) = \mathbf{v}(x, y)\frac{\mathbf{K}_x}{K_x} = v_x(x, y); \quad (3)$$

$$v_b(x, y) + v_g(x, y) = \mathbf{v}(x, y)\left(\frac{\mathbf{K}_b}{K_b} + \frac{\mathbf{K}_g}{K_g}\right) = \mathbf{v}(x, y)\frac{\mathbf{K}_z}{K_z} = v_z(x, y). \quad (4)$$

Figure 2a shows an example of the optical image of a 2D velocity field in the flow cross section selected by the laser sheet plane, constructed in the orthogonal coordinate basis set ($\mathbf{K}_b$, $\mathbf{K}_g$). Figure 2b presents the 2D velocity field of the swirling flow in the coordinate basis set ($\mathbf{K}_x$, $\mathbf{K}_z$). Figure 2c shows a stereo image of the reconstructed 2D velocity field (for 3D perception, eyes should be accommodated to the infinity).

For velocity field imaging with chromatic selection of the velocity vector components in a 3D orthogonal coordinate basis set, it is sufficient to form the third laser sheet plane using, for example, the radiation of a laser operating in the red spectral range. The wave vector $\mathbf{k}_r$ of the red laser sheet field should be perpendicular to the wave vectors of the blue ($\mathbf{k}_b$) and green ($\mathbf{k}_g$) laser sheets. The RGB signal separation into components and their processing are performed as described above.

The proposed method is the first technique capable of imaging the dynamic fields of flow velocity vectors in the orthogonal coordinate basis set, which considerably expands the possibilities of optical diagnostics in basic hydrodynamics and gasdynamics as well as in commercial technologies encountering the problem of nonperturbative monitoring and control of flows in fluids and condensed media.

Acknowledgments. This work was supported by the INTAS Foundation (project no. 00-135).

REFERENCES

1. Yu. N. Dubnishchev and B. S. Rinkevichyus, *Methods of Laser Doppler Anemometry* (Nauka, Moscow, 1982).
2. J. Puvost, J. Legrand, P. Legentilhömme, and L. Doubliez, Exp. Fluids **29**, 291 (2000).
3. P. Ya. Belousov, Yu. N. Dubnishchev, and I. G. Palchikova, Opt. Spektrosk. **52**, 876 (1982) [Opt. Spectrosc. **52**, 524 (1982)].
4. J. T. Turner, in *Proceedings of the 2nd International Conference of Fluid Dynamic Measurement and Its Application* (Int. Academic, Beijing, 1994), p. 551.
5. P. P. Belousov, P. Ya. Belousov, and Yu. N. Dubnishchev, Pis'ma Zh. Tekh. Fiz. **28** (16), 6 (2002) [Tech. Phys. Lett. **28**, 666 (2002)].
6. V. A. Arbuzov, Yu. N. Dubnishchev, A. V. Lebedev, *et al.*, Pis'ma Zh. Tekh. Fiz. **23** (23), 84 (1997) [Tech. Phys. Lett. **23**, 938 (1997)].
7. P. P. Belousov, P. Ya. Belousov, and Yu. N. Dubnishchev, Optoelectronics, Instrumentation, and Data Processing, No. 5, 1 (2001).

Translated by P. Pozdeev

Technical Physics Letters, Vol. 30, No. 4, 2004, pp. 316–318. Translated from Pis'ma v Zhurnal Tekhnicheskoĭ Fiziki, Vol. 30, No. 8, 2004, pp. 27–33.

One-Dimensional Fractal Walk at a Finite Free Motion Velocity

V. V. Uchaikin* and R. T. Sibatov

Ul'yanovsk State University, Ul'yanovsk, Russia

** e-mail: uchaikin@sv.uven.ru*

Received October 8, 2003

Abstract—We consider one-dimensional symmetric fractal walk of a particle with free path lengths distributed according to an asymptotic power law ($\propto x^{-\alpha-1}$) modeling the transport in a strongly inhomogeneous fractal media. The spatial distribution of particles is determined, which is a Gaussian distribution for $\alpha > 2$, a stable Lévy distribution for $1 < \alpha < 2$, and is confined within a finite segment for $\alpha < 1$, exhibiting a minimum in the middle and integrable singularities at the ends. Qualitative differences between these distributions are explained by the predominance of one of the two competitive processes: diffusion ($\alpha > 1$) and ballistic ($\alpha < 1$).

The transport theory and its numerous applications (see, e.g., [1]) are based on a simple model of randomly walking particles, with their trajectories representing broken lines consisting of independent random straight segments called free paths. The distribution of free path lengths in a homogeneous medium obeys an exponential law. In inhomogeneous media, an exponential law describes the distribution of the optical path length defined as the integral of the interaction cross section along the path. In the case of a self-similar inhomogeneous (fractal) medium modeling porous and some other media (see, e.g., review [2] and monograph [3]), the concept of cross section is inapplicable and the distributions acquire unusual forms. This Letter considers the simplest problem of this kind.

The one-dimensional symmetric walk of a particle at a finite free motion velocity v is characterized by a density of the distribution of the particle coordinate x at a time t,

$$p(x, t) = \frac{1}{2}\int_0^t [\, f(x - v\tau, t - \tau) + f(x + v\tau, t - \tau)]P(v\tau)d\tau, \quad (1)$$

where $P(x) = \int_x^\infty p(x)dx$, $p(x)$ is the distribution density of the random free path lengths at the end of which the direction of motion can change with a probability of 1/2 and $f(x, t)$ is the density of collisions (the average number of collisions on a unit length interval per unit time). If a particle starts walking from the origin at $t = 0$, the density of collisions $f(x, t)$ satisfies an integral equation [4]

$$f(x, t) = \frac{1}{2}\int_0^t [\, f(x - v\tau, t - \tau) + f(x + v\tau, t - \tau)\,]p(v\tau)d\tau + \delta(x)\delta(t). \quad (2)$$

In a homogeneous medium with exponential distribution of free path lengths, Eq. (2) converts into a differential equation in partial derivatives of second order (telegraph equation) [5]. The automodel solution of this equation is expressed in terms of modified Bessel functions and transforms into the normal (Gaussian) distribution in the asymptotic case of large times. For an arbitrary distribution density function $p(x)$ with a finite second-order moment, the telegraphy equation is satisfied with the asymptotic part of the solution.

Previously [4, 6, 7], it was demonstrated that asymptotic automodel solutions exist in the case of fractal walk with $p(x) \sim \alpha\varepsilon_0^\alpha x^{-\alpha-1}$, where $0 < \alpha < 2$. Below, we present the results of calculations for such distribution.

Using the Fourier–Laplace transform

$$\tilde{p}(k, \lambda) = \int_0^\infty dt \int_{-\infty}^{+\infty} dx \exp(ikx - \lambda t)\, p(x, t),$$

integral equations (1) and (2) can be transformed into algebraic relations of the type

$$\tilde{p}(k, \lambda) = \frac{1}{v} W(k, \lambda)\, \tilde{f}(k, \lambda),$$

$$\tilde{f}(k, \lambda) = 1 + w(k, \lambda)\tilde{f}(k, \lambda),$$

which can be solved with respect to the transform of the unknown distribution to yield

$$\tilde{p}(k, \lambda) = \frac{W(k, \lambda)}{v[1 - w(k, \lambda)]}. \quad (3)$$

Here,

$$w(k, \lambda) = \int_0^\infty e^{-(\lambda/v)x}\cos(kx)p(x)dx$$
$$= (1/2)[\tilde{p}(\lambda/v - ik) + \tilde{p}(\lambda/v + ik)],$$

$$W(k, \lambda) = \int_0^\infty \left[e^{-(\lambda/v)x}\cos(kx)\int_x^\infty p(\xi)d\xi\right]dx$$
$$= \frac{\lambda/v}{(\lambda/v)^2 + k^2}[1 - w(k, \lambda)]$$
$$+ \frac{k}{(\lambda/v)^2 + k^2}(1/2i)[\tilde{p}(\lambda/v - ik) - \tilde{p}(\lambda/v + ik)],$$

and

$$\tilde{p}(\lambda) = \int_0^\infty e^{-\lambda x}p(x)dx$$

is the Laplace transform of the free path length distribution density. Substituting these expressions into (3), we obtain

$$\tilde{p}(k, \lambda) = \frac{2(\lambda/v) - (\lambda/v + ik)\tilde{p}(\lambda/v - ik) - (\lambda/v - ik)\tilde{p}(\lambda/v + ik)}{v[k^2 + (\lambda/v)^2][2 - \tilde{p}(\lambda/v - ik) - \tilde{p}(\lambda/v + ik)]}. \quad (4)$$

According to the Tauber theorem [8], the asymptotic ($t \longrightarrow \infty$) behavior of the density $p(x, t)$ is determined by the asymptotic ($\lambda \longrightarrow 0$) behavior of the transform $\tilde{p}(k, \lambda)$. In the case of fractal walks, we have the following expansions:

$$\tilde{p}(\lambda) = 1 - c\lambda^\alpha, \quad c = (A/\alpha)\Gamma(1 - \alpha), \quad 0 < \alpha < 1,$$

$$\tilde{p}(\lambda) = 1 - m_1\lambda + c_1\lambda^\alpha, \quad c_1 = (A/\alpha)\frac{\Gamma(2 - \alpha)}{\alpha - 1},$$
$$1 < \alpha < 2,$$

$$\tilde{p}(\lambda) = 1 - m_1\lambda + (m_2/2)\lambda^2 - c_2\lambda^\alpha,$$
$$c_2 = (A/\alpha)\frac{\Gamma(3 - \alpha)}{(\alpha - 1)(\alpha - 2)}, \quad \alpha > 2,$$

where m_k are the moments of the free path length distribution.

In the first case ($0 < \alpha < 1$), we obtain the expression

$$\tilde{p}(k, \lambda) = \frac{(\lambda/v - ik)^{\alpha - 1} + (\lambda/v + ik)^{\alpha - 1}}{v[(\lambda/v - ik)^\alpha + (\lambda/v + ik)^\alpha]}.$$

In particular, for $\alpha = 1/2$, the transform

$$\tilde{p}(k, \lambda) = \frac{1}{v\sqrt{(\lambda/v)^2 + k^2}}$$

is readily inverted to yield

$$p(x, t; 1/2) = \frac{1}{\pi\sqrt{(vt)^2 - x^2}}. \quad (5)$$

For $1 < \alpha < 2$, the asymptotics of $|\lambda/vk| \longrightarrow 0$ yields the transform

$$\tilde{p}(k, \lambda)$$
$$= \frac{2m_1 - c_1(\lambda/v - ik)^{\alpha - 1} - c_1(\lambda/v + ik)^{\alpha - 1}}{v[2m_1(\lambda/v) - c_1(\lambda/v - ik)^\alpha - c_1(\lambda/v + ik)^\alpha]}$$
$$\sim \frac{1}{v[(\lambda/v) + R|k|^\alpha]},$$

where

$$R = (c_1/m_1)|\cos(\alpha\pi/2)|$$
$$= [\Gamma(2 - \alpha)/\varepsilon^{1 - \alpha}]|\cos(\alpha\pi/2)|.$$

In this case, the inverse Laplace transform leads to a characteristic function of the random coordinate of the walking particle that is related to the characteristic function $\tilde{g}(k; \alpha) = \exp(-|k|^\alpha)$ of the stable distribution density $g(x; \alpha)$ as

$$\tilde{p}(k, t) = e^{-Rvt|k|^\alpha} = \tilde{g}((Rvt)^{1/\alpha}k).$$

Reconstructing $p(x, t)$, we obtain

$$p(x, t) = \frac{1}{2\pi}\int_{-\infty}^{+\infty}\tilde{p}(k, t)e^{-ikx}dk = \frac{1}{2\pi}\int_{-\infty}^{+\infty}e^{-|(Rvt)^{1/\alpha}k|^\alpha}e^{-ikx}dk$$
$$= (Rvt)^{-1/\alpha}g(x(Rvt)^{-1/\alpha}; \alpha, 0),$$

where $g(x; \alpha, 0)$ is the symmetric stable density [9].

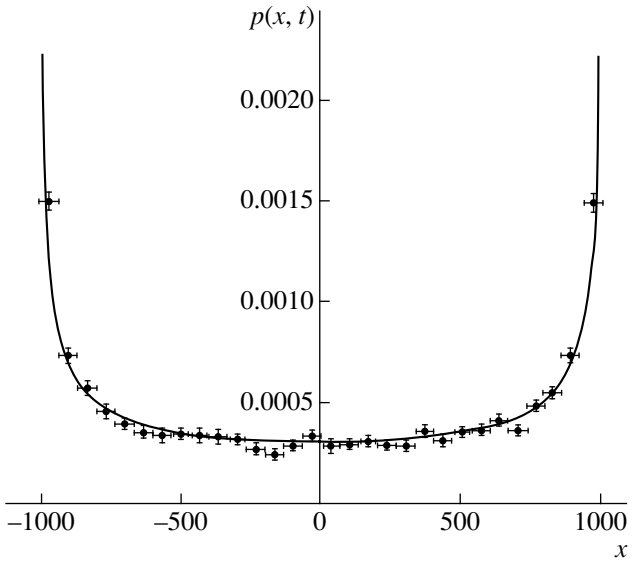

Fig. 1. Distribution density $p(x, t)$ for $t = 10^3$, $v = 1$, and $\alpha = 1/2$. Solid curve shows the results of calculations by formula (5); points present the results of Monte Carlo simulation.

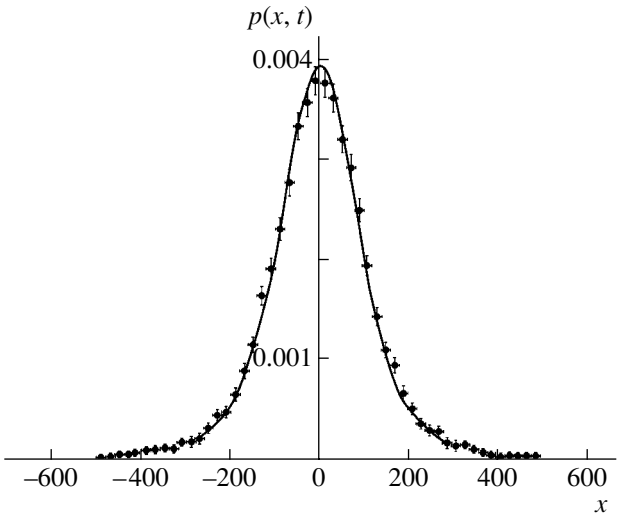

Fig. 2. Distribution density $p(x, t)$ for $t = 10^3$, $v = 1$, and $\alpha = 3/2$. Solid curve is constructed using data from the table of stable distribution densities; points present the results of Monte Carlo simulation.

Finally, for $\alpha > 2$ we obtain

$$\tilde{p}(k, \lambda) = \frac{2m_1 - m_2(\lambda/v) + c_2(\lambda/v - ik)^{\alpha-1} + c_2(\lambda/v + ik)^{\alpha-1}}{v[2m_1(\lambda/v) - m_2((\lambda/v)^2 - k^2) + c_2(\lambda/v - ik)^{\alpha} + c_2(\lambda/v + ik)^{\alpha}]}$$

$$\sim \frac{1}{v[(\lambda/v) + (m_2/2m_1)k^2]},$$

which yields

$$p(x, t) = (1/\sqrt{vtm_2/2m_1})g(x/\sqrt{vtm_2/2m_1}; 2, 0),$$

where $g(x; 2, 0)$ is the Gaussian distribution density.

Figures 1 and 2 show the results of numerical calculations for $\alpha = 1/2$ and 3/2 in comparison to the results of direct simulation using the Monte Carlo method. The qualitative difference between the distributions can be explained in terms of the competition between two processes: diffusion, corresponding to the expansion $\propto t^{1/\alpha}$ in the absence of limitations, and ballistic, restricting the particle position to the $[-vt, vt]$ segment. For $\alpha > 1$ and large times, the former process is predominating (rapidly expanding interval $[-vt, vt]$ ceases to influence the diffusion). For $\alpha < 1$, the role of kinematic limitations increases and the distribution concentrates in the regions adjacent to the boundaries. Originally, a distribution of this kind was obtained by Monte Carlo method in [10].

Acknowledgments. This study was supported by the Russian Foundation for Basic Research (project no. 03-01-00163) and the British Royal Society Foundation (grant gt/fSU/JP).

REFERENCES

1. A. M. Kol'chuzhkin and V. V. Uchaĭkin, *An Introduction to the Theory of Particles Transmission through Substance* (Atomizdat, Moscow, 1978) [in Russian].
2. M. B. Isichenko, Rev. Mod. Phys. **64**, 961 (1992).
3. D. Ben-Avraham and S. Havlin, *Diffusions and Reactions in Fractal and Disordered Systems* (Cambridge University Press, Cambridge, 2000).
4. V. V. Uchaikin, Zh. Tekh. Fiz. **68**, 138 (1998) [Tech. Phys. **43**, 124 (1998)].
5. V. V. Uchaikin and V. V. Saenko, J. Phys. Stud. **4**, 371 (2000).
6. V. V. Uchaikin, Physica A **255**, 65 (1998).
7. V. V. Uchaikin and V. M. Zolotarev, *Chance and Stability* (VSP, Ultrech, 1999).
8. W. Feller, *An Introduction to Probability Theory and Its Applications*, 3rd ed. (Wiley, New York, 1966; Mir, Moscow, 1967).
9. V. M. Zolotarev, *One-Dimensional Stable Distributions* (Fizmatlit, Moscow, 1983).
10. V. M. Zolotarev, V. V. Uchaikin, and V. V. Saenko, Zh. Éksp. Teor. Fiz. **115**, 1411 (1999) [JETP **88**, 780 (1999)].

Translated by P. Pozdeev

Technical Physics Letters, Vol. 30, No. 4, 2004, pp. 319–321. Translated from Pis'ma v Zhurnal Tekhnicheskoĭ Fiziki, Vol. 30, No. 8, 2004, pp. 34–39.

Analytical Solution of the Takagi Equations for X-ray Backscattering from a Cylindrically Bent Crystal

T. Chen

Moscow State Academy of Fine Chemical Technology, Moscow, Russia

e-mail: docent65@mtu-net.ru; ttchen@e-mail.ru

Received September 9, 2003

Abstract—An approximate analytical solution of the system of Takagi equations for the amplitudes of diffracted and transmitted waves is obtained for the backscattering of a plane X-ray wave from an elastically bent crystal. In the case of diffraction in the reverse direction (strict backscattering), the obtained solution is exact.

This Letter reports on an analytical solution of the system of Takagi equations describing the amplitudes of diffracted and transmitted waves in the case of a monochromatic X-ray wave backscattering from a bent ideal crystal.

Consider a plane X-ray wave $E_0(\mathbf{r}, t) = E_0(\mathbf{r}, \omega)\mathbf{e}_0\exp(i\mathbf{k}_0\mathbf{r} - i\omega t)$ outgoing from a point source S (Fig. 1), passing through a monochromator separating the frequency ω, and incident onto a cylindrically bent crystal at an angle of φ_0 with respect to the normal to the crystal surface at its center. Here, ω is the wave frequency, $\mathbf{e}_0$ is the polarization vector, and $\mathbf{k}_0$ is the wave vector of the incident wave. Expanding the X-ray polarizability $\chi(\mathbf{r})$ of the crystal into a Fourier series and restricting the expansion to the first three terms, we obtain

$$\chi(\mathbf{r}) = \sum_{0, \pm h} \chi_h \exp\{i\mathbf{h}[\mathbf{r} - \mathbf{u}(\mathbf{r})]\}. \qquad (1)$$

Here, $\chi_h = \chi_{hr} + i\chi_{hi}$ are the Fourier components of the X-ray polarizability of the ideal crystal and $\mathbf{r}(x, y)$ is the radius vector of an atom in the unbent crystal. Let us consider the case of $\varphi_0 \le |\chi_{hr}|^{1/2}$, which corresponds to the incident wave fully reflected from the crystal in the reverse direction. When $\varphi_0 \gg |\chi_{hr}|^{1/2}$, we may assume that $\theta_B \neq \pi/2$. For this case, an analytical solution of the system of Takagi equations was obtained by Chukhovskii *et al.* [1–3]. The diffraction reflection in the direction of the wave vector $\mathbf{k}_h$ is elastic and coherent, so that $\mathbf{k}_h^2 = \mathbf{k}_0^2 = \kappa^2$.

Let us consider backscattering from a crystal with one-dimensional bending, whereby $\mathbf{hu} = \kappa(x^2/R_x + z^2/R_z)$. Here, $\mathbf{h}$ is the reciprocal lattice vector of the ideal unbent crystal, $\mathbf{u}$ is the vector of elastic displacement of atoms in the crystal lattice upon elastic bending of the crystal, R_x is the radius of crystal bending in the diffraction plane determined by the $\mathbf{k}_0$ and $\mathbf{n}$ vectors, and R_z is the radius expressed via components of the reciprocal tensor of elastic moduli [4, 5].

Previously [6], the system of Takagi equations [7, 8] was reduced to a second-order differential equation for the diffracted wave amplitude E_h,

$$d^2E_h/dz^2 + A(z)dE_h/dz + B(z)E_h(z) = 0, \qquad (2)$$

where

$$A(z) = A_1 + A_2z, \quad A_1 = 2i(\Delta\theta)^2, \quad A_2 = 2i\kappa/R_z,$$
$$B(z) = B_1 + B_2z,$$

$$B_1 = \kappa^2\{\chi_0(\chi_0 + \alpha) - \chi_h\chi_{-h}\}/4,$$
$$B_2 = -\kappa^2(\chi_0 - \alpha)/R_z,$$

$$\alpha = -4(\Delta\theta)^2, \quad \Delta\theta = \theta - \pi/2,$$

and θ is the sliding angle for the incident plane harmonic wave. Equation (2) was obtained for an (x, z) region inside the crystal such that $x \gg z\tan\varphi_0$, where (according to the above assumption) $\tan\varphi_0 \sim |\chi_{hr}|^{1/2}$ (Fig. 2). In the case of diffraction in the reverse direction (strict backscattering), whereby $\varphi_0 = 0$, Eq. (2) is valid for any x, z.

A solution to Eq. (2) has the form of a Fourier integral,

$$E_h(2) = (2\pi)^{-1}\int_{-\infty}^{+\infty} dkG_h(k)\exp(ikz), \qquad (3)$$

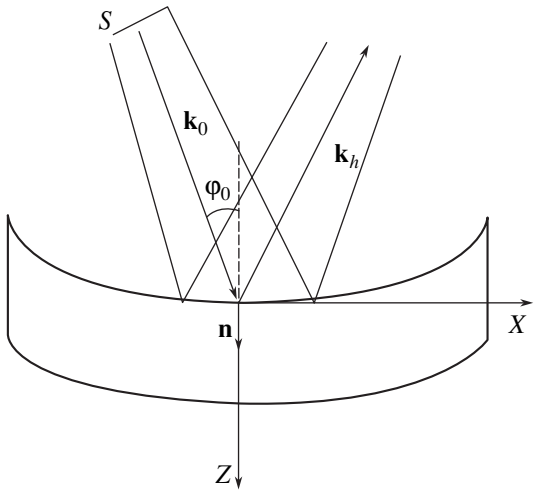

Fig. 1. The geometry of backscattering of a plane monochromatic X-ray wave emitted from source *S*, incident at an angle φ_0 onto a cylindrically bent crystal (**n** is the unit vector of normal to the crystal surface; $\mathbf{k}_0$ and $\mathbf{k}_h$ are the wave vectors of the incident and diffracted waves, respectively).

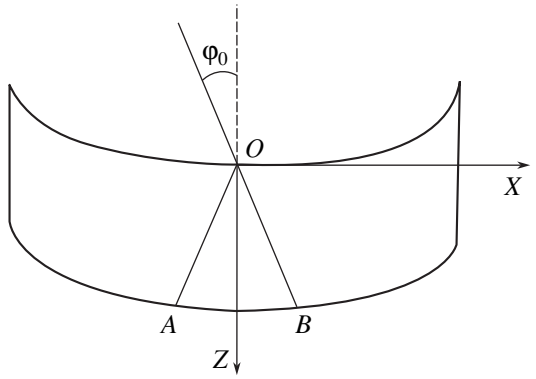

Fig. 2. Schematic diagram illustrating the boundaries of applicability of Eqs. (2) and (10). Lines *OB* and *OA* correspond to the equation $|x| = 10 \tan\varphi_0 z$. Takagi equations in the form (2) and (10) and, hence, the obtained solutions are valid to the left of *OA* and to the right of *OB*.

where

$$G_h(k) = \exp(-ik^2/2A_2 - A_1k/A_2 + B_2k/A_2^2) \times (1 + ikA_2/B_2)_3^{-A}(iB_2)^{-1}, \quad (4)$$

$$A_3 = (A_1A_2B_2 - B_2^2 - B_1A_2^2 - A_2^3)/A_2^3. \quad (5)$$

As can be readily seen, the $G_h(k)$ function for the ideal unbent crystal ($A_2 \longrightarrow 0$, $B_2 \longrightarrow 0$) is proportional to the delta function $\delta(k - \varepsilon_{1,2})$, where $\varepsilon_{1,2}$ are the excitation errors for the ideal crystal:

$$\varepsilon_{1,2} = \{iA_1 \pm (-A_1^2 + 4B_1)^{1/2}\}/2. \quad (6)$$

The amplitude E_h of the diffracted wave can be presented both in the integral form (3) and in the form of an infinite Laurent series. Indeed, expanding the function $(1 + ikA_2/B_2)_3^{-A}$ into series,

$$(1 + ikA_2/B_2)_3^{-A} = 1 + \sum_{n=0}^{\infty} \{\Gamma(n + 1 + A_3)/\Gamma(A_3)(n + 1)!\}(-ikA_2/B_2)^{n+1}, \quad (7)$$

where $\Gamma(x)$ is the gamma function, the integral in solution (3) can be written as

$$E_h(z) = (i\pi B_2)^{-1}\left\{\int_0^{+\infty} dk \exp(-k^2/2|A_2|) \times \cos(A_1k/A_2 - B_2k/A_2^2 + kz) + \sum_{n=0}^{\infty} \{\Gamma(n + 1 + A_3)/\Gamma(A_3)(n + 1)!\}(-iA_2/B_2)^{n+1} \times \int_0^{+\infty} dk \exp(-k^2/2|A_2|)\cos(A_1k/A_2 - B_2k/A_2^2 + kz)k^{n+1}\right\}. \quad (8)$$

Taking in to account that $\cos x = (\pi x/2)^{1/2}J_{-1/2}(x)$, where $J_{-1/2}(x)$ is the (–1/2)-order Bessel function of the real argument and using the Weber–Sonin formula [9] for the calculation of integrals in relation (8), we obtain an expression for the diffracted wave amplitude,

$$E_h(z) = (i\pi B_2)^{-1}\{(2\pi A_2)^{1/2}\exp(-a^2A_2) + \sum(\Gamma(n + 1 + A_3)\Gamma(1 + n/2)/\Gamma(A_3)(n + 1)!) \times (2^{-1-n/2}A_2^{-1-n/2})(-iA_2/B_2)^{n+1}{}_1F_1(1 + n/2; 1/2; -a^2A_2)\}, \quad (9)$$

where $a = A_1/A_2 - B_2/A_2^2 + z > 0$ and ${}_1F_1(\alpha; \beta; z)$ is the degenerate hypergeometric function. The total diffracted wave amplitude is $E_h(\mathbf{r}) = E_h(z)E_h(x)$, where $E_h(x) = \exp(-i\kappa x^2/R_x)$.

For the transmitted wave amplitude $E_0(z)$ under the same assumptions as those used in deriving Eq. (2), we obtain a differential equation of the second order,

$$d^2E_0/dz^2 - A(z)dE_0(z)/dz + C(z)E_0(z) = 0, \quad (10)$$

where

$$C(z) = C_1 + C_2z, \quad C_1 = B_1, \quad C_2 = -\kappa^2\chi_0/R_z.$$

The final expression for $E_0(z)$ is given by formula (8) upon substitutions $A_1 \longrightarrow -A_1$, $A_2 \longrightarrow -A_2$, and $B_2 \longrightarrow C_2$.

The interval of angles φ_0 in which Eqs. (2) and (10) are valid is determined by the condition

$$\sin\varphi_0 E_h(z)dE_h(x)/dx \ll \cos\varphi_0 E_h(x)dE_h(z)/dz.$$

Substituting the explicit form of $E_h(x)$, we obtain

$$\tan\varphi_0 \ll R_x(2\kappa x)^{-1}\left|d\ln E_h(z)/dz\right|. \quad (11)$$

This inequality is satisfied, in particular, in the case of diffraction in the reverse direction (strict backscattering), whereby $\varphi_0 \equiv 0$. For $\varphi_0 \neq 0$, condition (11) is reliably fulfilled for $\tan\varphi_0 \ll x/z$. In the case of a slightly bent crystal with a large curvature radius R_x, whereby the reflection coefficient is close to that of the flat (unbent) ideal crystal, inequality (11) reduces to $\tan\varphi_0 \ll R_x\varepsilon(2\kappa x)^{-1}$, where ε is the excitation errors for the ideal crystal. For the ideal crystal, this angular interval is very broad and extends beyond the total reflection region.

In conclusion, it should be recalled that Eqs. (2) and (10) and, hence, the obtained solutions were derived for a nearly normal incidence of the X-ray wave on the crystal, so that $\gamma_0 = -\gamma_h \cong (1 - \varphi_0^2)^{1/2} \cong 1$. In the case of backscattering with directing cosines $\gamma_0 = -\gamma_h \ll 1 - |\chi_{hr}|/2$ (i.e., far outside the total reflection region), the "usual" dynamical theory of X-ray diffraction is applicable.

REFERENCES

1. F. N. Chukhovskiĭ, K. T. Gabrielyan, and P. V. Petrashen', Dokl. Akad. Nauk SSSR **238**, 81 (1978) [Sov. Phys. Dokl. **23**, 52 (1978)].
2. F. N. Chukhovskii, K. T. Gabrielyan, and P. V. Petrashen', Acta Crystallogr., Sect. A **34**, 610 (1978).
3. K. T. Gabrielyan, F. N. Chukhovskiĭ, and Z. G. Pinsker, Zh. Tekh. Fiz. **50**, 3 (1980) [Sov. Phys. Tech. Phys. **25**, 1 (1980)].
4. K. T. Gabrielyan, F. N. Chukhovskiĭ, and D. I. Piskunov, Zh. Éksp. Teor. Fiz. **96**, 834 (1989) [Sov. Phys. JETP **69**, 474 (1989)].
5. F. N. Chukhovskii, W. Z. Chang, and E. Foerster, J. Appl. Crystallogr. **27**, 971 (1994).
6. T. Tchen, Pis'ma Zh. Tekh. Fiz. **29** (7), 38 (2003) [Tech. Phys. Lett. **29**, 282 (2003)].
7. S. Takagi, Acta Crystallogr. **15**, 1311 (1962).
8. S. Takagi, J. Phys. Soc. Jpn. **26**, 1239 (1969).
9. *Encyclopedic Dictionary of Mathematics*, Ed. by S. Iyamaga and Y. Kawada (MIT Press, Cambridge, 1980), p. 1474.

Translated by P. Pozdeev

Technical Physics Letters, Vol. 30, No. 4, 2004, pp. 322–324. Translated from Pis'ma v Zhurnal Tekhnicheskoĭ Fiziki, Vol. 30, No. 8, 2004, pp. 40–45.

Surface States at the Nanoparticle–Polymer Matrix Interface

E. I. Grigor'ev*, S. A. Zav'yalov, and S. N. Chvalun

Karpov Institute of Physical Chemistry, State Scientific Center of the Russian Federation, Moscow, 103064 Russia

** e-mail: evg@cc.nifhi.ac.ru*

Received October 14, 2003

Abstract—The energy barriers for hole injection in polymeric nanocomposites representing a poly(*p*-xylylene) (PPX) matrix containing dispersed lead or iron nanoparticles were determined by means of photoconductivity spectroscopy. The barriers for hole injection from metal particles in nanocomposites measured in vacuum are 3.6 eV for iron and 3.0 eV for lead; upon oxygen admission, these values decrease to ~3.2 and ~2.75 eV, respectively. A shift between the vacuum energy levels of PPX and metal nanoparticles amounts to 1.0 and 0.1 eV for iron and lead, respectively. The greater value for iron suggests the formation of a surface electric dipole, probably as a result of the chemical interaction at the metal nanoparticle–matrix interface. © *2004 MAIK "Nauka/Interperiodica".*

The transport of charge carriers via the interphase boundary between a metal (or semiconductor) and an organic substance is a basic process determining the efficiency of organic field-effect transistors, organic light-emitting diodes, and organic photoelectric converters [1], the conductivity of molecular wires [2], and the functioning of single-electron transistors [3, 4]. In recent years, much attention has been devoted to metal(semiconductor)–polymer nanocomposites [5]. Because of the very large area of the interphase boundaries between nanoparticles and the polymer matrix in such materials, the electron properties of this interface determine the conductivity of polymeric nanocomposites. Examples are offered by the photoconductivity of systems such as CdSe–polymer [6], CdS–poly(*N*-vinylcarbazole) [7], and CdS–polystyrene [8] and by the sensor properties of metal(semiconductor)–poly(*para*-xylylene) nanocomposites [9].

The electron structure of an interphase boundary is determined by chemical interactions at the interface and strongly depends on the chemical nature of this contact, the technological conditions of its formation, and the gas atmosphere. Numerous investigations (see, e.g., [10]) showed that the condition of equal vacuum energy levels in the contact of an organic solid matrix and a metal (semiconductor) accepted in the Mott–Schottky model [11] is usually not satisfied. A shift between the vacuum energy levels is evidence of the formation of a surface electric dipole. The presence of such surface dipoles must influence the magnitude of the energy barrier for charge carrier injection. If the surface dipole is oriented with its negative pole toward the organic solid, the barrier φ_h for hole injection will decrease as compared to the value corresponding to the Mott–Schottky model,

$$\varphi_h = I_{org} - W_M - \Delta, \quad (1)$$

where I_{org} is the ionization potential of the organic compound, W_M is the electron work function of the metal (semiconductor), and Δ is the shift between energy levels related to the surface electric dipole formation. The opposite orientation of the surface dipole will increase the barrier for hole injection. Factors favoring the formation of surface dipoles (leading to significant shifts between the vacuum energy levels, amounting up to $\Delta \sim 1$ eV) as a result of adsorption of various organic substances and polymers on metals were considered in [10, 12, 13].

This Letter reports on the results of investigation of the electron structure of the metal nanoparticle–polymer matrix interface in nanocomposites representing a poly(*p*-xylylene) (PPX) matrix containing dispersed lead or iron nanoparticles. For this purpose, we have measured the photocurrent in nanocomposites as a function of the wavelength and determined the magnitude of the energy barrier for hole injection at the interface.

The samples were synthesized by co-deposition of the monomers (*p*-xylylene) and metal vapors onto a cooled (77 K) substrate in vacuum. The monomer vapor was obtained by pyrolysis of paracyclophane at 600°C. Metal vapors were produced by thermal (for lead) or electron-beam (for iron) evaporation of bulk substances. Subsequent heating of the co-deposited mixture to room temperature led to polymerization of *p*-xylylene molecules and aggregation of metal atoms,

resulting in the formation of a PPX film containing dispersed metal nanoparticles. The average size of metal nanoparticles estimated by means of wide- and small-angle X-ray scattering was ~10 nm. The preparation and structural characterization of nanocomposites were described in more detail elsewhere [14]. The conductivity and photoconductivity of nanocomposites were measured as described in [15].

It was found that the dependence of the relative magnitude of photocurrent J on the photon energy E in the exciting light beam ($\lambda > 300$ nm) obeys the Fowler law $J \sim (E - \varphi_h)^2$ (Fig. 1) [16]. The energy barrier for hole injection from metal nanoparticles was ~3.6 eV for iron and ~3.0 eV for lead when the measurements were performed in vacuum; upon oxygen admission, these values decrease to ~3.2 and ~2.75 eV, respectively. The value of the barrier for hole injection from lead agrees well with the published data [16]. Assuming the ionization threshold of PPX to be 6.9 eV [16] and setting the electron work function from both iron and lead equal to 4.3 eV [17], we estimate the shifts between the vacuum energy levels of PPX and the metal as $\Delta = -1.0$ and -0.1 eV for iron and lead, respectively.

The chemical potential of PPX calculated according to [18] is –4.2 eV, which is greater than the chemical potential of iron. In this case, there should be a partial transfer of electron density from PPX to iron, in agreement with the observed direction of a chemical dipole. No such agreement is observed for lead, but the value of the shift between vacuum energy levels for this metal is small and falls within the error limits (±0.1 eV) of determination of the barrier for hole injection.

One possible factor accounting for the surface dipole formation is the chemical interaction (e.g., via chemisorption or bond formation) between the organic compound and the metal surface [10]. In our case, the interaction between PPX and the surface of metal nanoparticles may lead to the formation of arene complexes. The possibility of a chemical interaction between PPX and iron surface is also confirmed by the results obtained in [19].

Another possible factor is related to the surface states of polymer. The density of surface states estimated from the shift of the vacuum energy levels as described in [20] amounts to $N_s \sim 1.1 \times 10^{13}$ cm^{-2} eV^{-1}. A decrease in the barrier for hole injection upon oxygen admission can be related to the acceptor surface states. The density of additional charged surface states related to the adsorption of oxygen on the polymer surface is N_s–$O_2 \approx 9 \times 10^{12}$ cm^{-2}. These estimates agree with the published data for PPX [21]. However, we believe that the main factor accounting for the decrease in the energy barrier for hole injection is an increase in the electron work function of the metal nanoparticle upon oxygen adsorption.

Using published data on the electron structure of PPX [16, 22] and the results of measurements of the energy barrier for hole injection in nanocomposites, it is possible to construct a diagram of the electron structure of the interphase boundary between metal nanoparticles and the polymer matrix (Fig. 2).

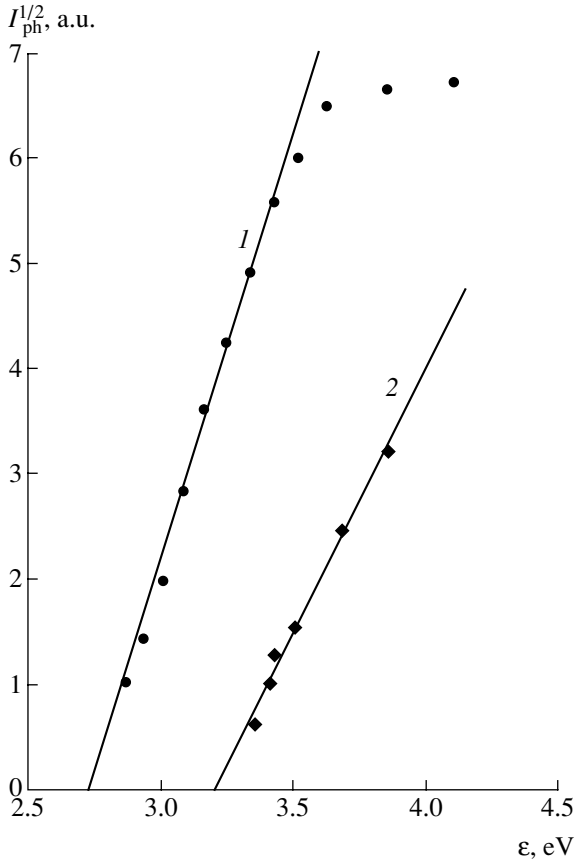

Fig. 1. Plots of the photocurrent versus photon energy of exciting light in PPX nanocomposites with (*1*) lead and (*2*) iron. The energy barrier for hole injection was determined by the Fowler formula.

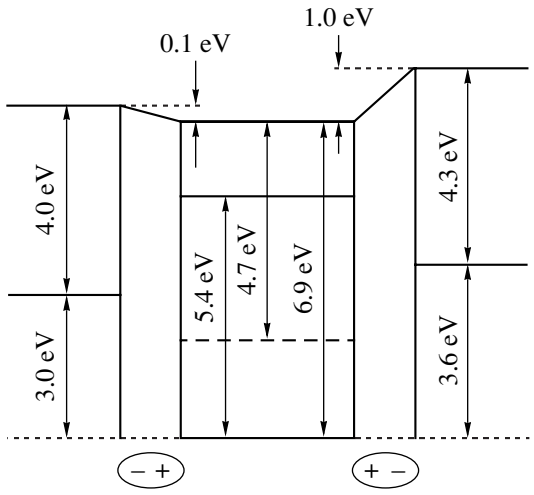

Fig. 2. A schematic diagram of the electron structure of the phase boundary in PPX–metal (iron or lead) nanocomposites.

Thus, we have shown that a chemical interaction (e.g., the formation of arene complexes) at the boundary between PPX matrix and iron nanoparticles leads to the formation of an electric dipole resulting in a shift of the vacuum energy levels between the matrix and metal. The presence of this dipole at the interface has to be taken into account in consideration of the transport properties of polymeric nanocomposites.

Acknowledgments. This study was supported by the Russian Foundation for Basic Research, project no. 01-03-32615.

REFERENCES

1. S. R. Forrest, Chem. Rev. **97**, 1793 (1997).
2. C. Kergueris, J.-P. Bourgoin, S. Palacin, *et al.*, Phys. Rev. B **59**, 12505 (1999).
3. D. V. Averin and K. K. Likharev, *Mesoscopic Phenomena in Solids*, Ed. by B. L. Altshulrs, P. A. Zee, and R. A. Webb (Elsevier, Amsterdam, 1991), p. 173.
4. M. A. Kastner, Rev. Mod. Phys. **64**, 849 (1992).
5. *Nanotechnology Research Directions: Working Group on Nanoscience, Engineering and Technology (IWGN) Workshop Report*, Ed. by M. C. Roco, R. S. Williams, and P. Alivisatos (Kluwer, Dordrecht, 2000).
6. N. C. Greenham, X. Peng, and A. P. Alivisatos, Phys. Rev. B **54**, 17628 (1996).
7. J. C. Winiarz, L. Zhang, M. Lal, *et al.*, Chem. Phys. **245**, 417 (1999).
8. S.-H. Yu, M. Yoshimura, J. M. C. Moreno, *et al.*, Langmuir **17**, 1700 (2001).
9. E. I. Grigor'ev, P. S. Vorontsov, S. A. Zav'yalov, and S. N. Chvalun, Pis'ma Zh. Tekh. Fiz. **28** (20), 15 (2002) [Tech. Phys. Lett. **28**, 845 (2002)].
10. H. Ishii, K. Sugiyama, E. Ito, and K. Seki, Adv. Mater. **11**, 605 (1999).
11. R. Monch, Surf. Sci. **299**–**300**, 928 (1994).
12. I. G. Hill, J. Schwartz, and A. Kahn, Org. Electron. **1**, 5 (2000).
13. G. Greczynski, T. Kugler, and W. R. Salanek, Curr. Appl. Phys. **1**, 98 (2001).
14. E. N. Nikolaeva, S. A. Ozerin, E. I. Grigoriev, *et al.*, Mater. Sci. Eng. C **8**–**9**, 217 (1999).
15. G. N. Gerasimov, A. E. Grigor'ev, and E. I. Grigor'ev, Khim. Fiz. **17** (6), 180 (1998).
16. Y. Takai, A. Kurachi, T. Mizutani, *et al.*, J. Phys. D **15**, 917 (1982).
17. *Physical Quantities. Handbook*, Ed. by I. S. Grigor'ev and E. Z. Meĭlikhov (Énergoatomizdat, Moscow, 1991).
18. X. Crispin, V. Geskin, A. Crispin, *et al.*, J. Am. Chem. Soc. **124**, 8131 (2002).
19. K. M. Vaeth and K. F. Jensen, Chem. Mater. **12**, 1305 (2000).
20. T. Mizutani, Y. Takai, T. Osawa, *et al.*, J. Phys. D **9**, 2253 (1976).
21. Y. Takai, K. Ishii, T. Mizutani, *et al.*, J. Phys. D **12**, 601 (1979).
22. Y. Takai, M. Kobayashi, T. Mizutani, *et al.*, J. Phys. D **21**, 1151 (1988).

Translated by P. Pozdeev

Technical Physics Letters, Vol. 30, No. 4, 2004, pp. 325–327. Translated from Pis'ma v Zhurnal Tekhnicheskoĭ Fiziki, Vol. 30, No. 8, 2004, pp. 46–52.

Luminescence Quenching in Erbium-Doped Phosphate Glass Films Irradiated with Hydrogen Ions

O. N. Gorshkov*, A. V. Dmitryuk, V. A. Kamin, A. P. Kasatkin, M. D. Mikhaĭlov, V. A. Novikov, A. B. Chigineva, and Yu. I. Chigirinskiĭ

Physicotechnical Research Institute, Nizhni Novgorod State University, Nizhni Novgorod, Russia
SENSIS Company, St. Petersburg, Russia
HOLOGRATE Corporation, St. Petersburg, Russia
** e-mail: gorshkov@nifti.unn.ru; lab10@phys.unn.ru*
Received October 6, 2003

Abstract—We have studied the effect of irradiation with hydrogen and helium ions on the photoluminescence (PL) of phosphate films doped with ytterbium and erbium. The irradiation with hydrogen ions leads to more effective quenching of the PL from erbium ions and, for the ion doses $\Phi \geq 5 \times 10^{16}$ cm^{-2}, to a more significant decrease in the PL lifetime as compared to that in the films irradiated with helium ions. The results are interpreted within the framework of a model assuming the formation of OH groups in ion-irradiated glasses, which offer an effective channel of nonradiative recombination of the electron excitations in the material studied. © *2004 MAIK "Nauka/Interperiodica".*

Introduction. Highly concentrated phosphate glasses doped with ytterbium and erbium are promising materials for planar amplifiers operating in a wavelength range of 1.5–1.6 μm, which is most important for optical communications. In order to provide for a maximum use of the pump radiation at a small length of the active element and a relatively low erbium concentration (about 1–2 wt %), the crystal is pumped by a semiconductor laser at 0.96–0.98 μm in the absorption band of ytterbium, after which erbium is excited due to a nonradiative energy transfer from ytterbium. One of the main problems encountered in the development of such media is to ensure the maximum quantum yield of luminescence from the activator (erbium), because glasses with maximum quantum yields possess minimum lasing thresholds.

As is known, the luminescent properties of erbium ions depend to a considerable degree both on the matrix type and on the presence of defects (nonstoichiometry, broken bonds) and technological impurities (in particular, OH groups [1]) effectively quenching the luminescence of erbium as a result of the nonradiative energy transfer via the induced resonance mechanism. Experiments on the samples irradiated with electrons and γ quanta [2] showed that the role of impurity centers producing effective luminescence quenching can be played by the radiation-induced color centers, especially in the case of activators emitting in the short-wavelength range. However, the influence of radiation defects and impurities incorporated by means of ion implantation into glasses activated by ytterbium and erbium, as well as in planar structures based on such glasses, is still almost unstudied.

This Letter presents experimental data on the influence of irradiation with hydrogen and helium ions on the photoluminescence (PL) of films of highly concentrated phosphate glasses doped with ytterbium and erbium.

Experimental. The sample films were prepared on fused quartz and soda-ash glass substrates by RF magnetron sputtering [3] of the target made of a phosphate glass containing 6.5 mol % Yb_2O_3 and 1 mol % Er_2O_3. The structure of deposited films before and after annealing was studied by X-ray diffraction on a DRON-3 diffractometer. All as-deposited films and those annealed in a temperature range below 650°C were X-ray amorphous.

The thicknesses and refractive indices of the films were determined by ellipsometry on an LEF-3M instrument with a He–Ne laser source (λ = 632.8 nm). The PL spectra were measured using a setup based on a single-grating monochromator MDR-23 (LOMO Company, St. Petersburg). The emission was detected by an InGaAs detector (DILAS Company). The PL was excited by a 1-W semiconductor laser operating at 0.98 μm. The PL lifetime τ of erbium, defined as the time for which the maximum PL peak intensity decreases by one order of magnitude, was determined using a conventional method employing pulsed pumping.

In order to increase the quantum yield of luminescence from erbium, the films were annealed in dry oxygen in a temperature interval from 400 to 650°C. The

1063-7850/04/3004-0325$26.00 © 2004 MAIK "Nauka/Interperiodica"

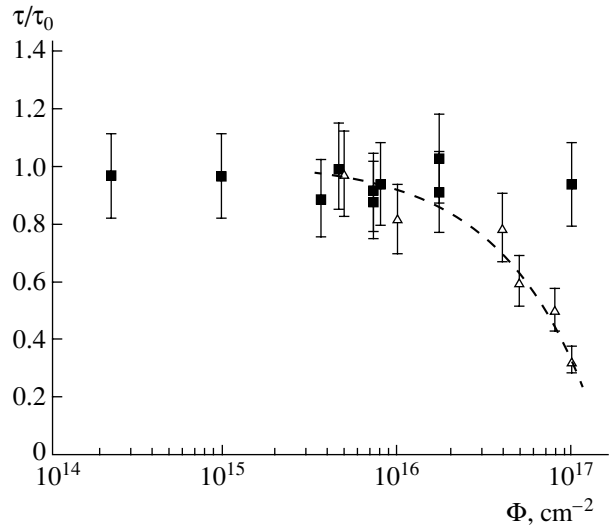

Fig. 1. A plot of the ratio τ/τ_0 versus irradiation dose for phosphate films irradiated with (■) helium and (△) hydrogen ions (τ_0 and τ are the PL lifetimes in the initial and irradiated films, respectively). Dashed line shows the character of decrease in the PL lifetime with increasing dose of hydrogen ions.

samples annealed at low temperatures (400–450°C) had a lower lifetime of the excited state of erbium compared to that in the initial glass and exhibited nonexponential decay of the PL intensity, which was characteristic of the static mechanism of quenching described by the Furster–Dexter–Galanin theory [2]. After the annealing at 500–650°C, the luminescence lifetime increased 5–10 times to reach $\tau_0 \cong 5$ ms, which was close to the value in the initial glass used as the target for the sample film deposition. The PL intensity (I) per unit volume of these films was also close to that for bulk glasses of the corresponding composition, which was evidence of completed synthesis of the given compound.

The samples of phosphate glass films were irradiated with helium and hydrogen ions. The irradiation doses ranged from $\Phi_{He^+} = 2 \times 10^{14}$ to 1×10^{17} cm^{-2} for helium ions and from $\Phi_{H^+} = 5 \times 10^{15}$ to 3×10^{17} cm^{-2} for hydrogen ions. The ion energies were $E(He^+)$ = 100 keV (projected ion range, R_p = 645.8 nm; ΔR_p = 148.1 nm) and $E(H^+)$ = 70 keV (R_p = 642.5 nm; ΔR_p = 98.4 nm). The incident ion beam energies were selected so as to provide that the projected ion range would be approximately equal and not exceeding the film thickness. The ion irradiation regimes were selected based on the results of calculations using the TRIM-91 computer program package. These conditions allowed us to compare changes in the PL parameters of samples with equal (i) elastic energy losses of the incident ions, (ii) inelastic energy losses, and (iii) total energy losses for helium and hydrogen. Equal total amounts of vacancies produced in the matrix as a result of elastic collisions with incident helium and hydrogen ions were observed for the ion dose ratio Φ_H/Φ_{He} = 17 : 1; equal inelastic losses correspond to Φ_H/Φ_{He} = 1.35 : 1; and equal total losses, to Φ_H/Φ_{He} = 1.43 : 1.

Results and discussion. The PL spectra of the initial films measured in a wavelength interval from 1.2 to 1.65 μm had the shape characteristic of the emission from erbium centers in an oxygen environment and exhibited no significant differences from the PL spectra of the initial glasses. The PL intensity maximum at λ = 1.534 μm corresponds to the transition $^4I_{13/2} \longrightarrow {}^4I_{15/2}$ in Er^{3+} ions [1, 4].

The results of our experiments showed that the PL intensity I of samples irradiated with helium ions monotonically decreased with increasing ion dose; for $\Phi_{He^+} = 1 \times 10^{17}$ cm^{-2}, the PL intensity amounted to approximately half of the initial value. In the dose range indicated above, the PL lifetime τ as well as the shape of the PL spectrum remained virtually unchanged (Fig. 1).

It should be noted that the intensity of PL from erbium centers in the glasses doped with ytterbium and erbium is proportional to the initial donor (ytterbium) concentration, the probability of energy transfer from ytterbium to erbium, and the quantum yield of luminescence from erbium. The probability of energy transfer depends on the presence of additional absorption centers, such as the radiation-induced color centers [2]. Since the absorption bands of these centers in phosphate glasses fall within the UV and visible spectral intervals [5] and the energy of the radiative transition in Yb^{3+} ($^2F_{7/2} \longrightarrow {}^2F_{5/2}$) is approximately 1.5 times that of the transition in Er^{3+} ($^4I_{13/2} \longrightarrow {}^4I_{15/2}$), we may expect that the influence of the radiation-induced color centers on the luminescence is more pronounced for ytterbium than for erbium. Thus, a decrease in the PL intensity at a constant PL lifetime observed for erbium-doped glass films irradiated with helium ions can be explained by a decrease in the probability of nonradiative energy transfer from ytterbium to erbium. In addition, there is a direct channel for the quenching of PL from erbium by the radiative breakage of emitting ytterbium and erbium centers, for example, as a result of the displacement of oxygen atoms from equilibrium positions.

The character of variation of the PL parameters in the course of hydrogen bombardment was substantially different from that observed for the irradiation with helium ions. In particular, there was more (about tenfold) effective PL quenching at a hydrogen ion dose of $\Phi_{H^+} = 10^{17}$ cm^{-2} and complete suppression for $\Phi_{H^+} \geq 3 \times 10^{17}$ cm^{-2}. The dose dependence of the PL lifetime in the films irradiated with hydrogen ions to doses below $\Phi_{H^+} = 5 \times 10^{16}$ cm^{-2} was close to the behavior observed for the samples irradiated with helium ions. This fact indicates that the PL lifetime in this dose

range is weakly controlled by the elastic and inelastic radiative processes. However, an increase in the dose above this level led to a rapid decrease in the PL lifetime (Fig. 1), which can be related to switching of an additional channel of the PL quenching. This is confirmed by the experimental data presented in Fig. 2. As can be seen, the PL decay time for $\Phi_{H^+} \geq 5 \times 10^{16}$ cm^{-2} significantly decreases and the PL decay curve exhibits a substantially nonexponential character.

An analysis of the experimental data suggests that the films irradiated with H^+ ions to doses above 5×10^{16} cm^{-2} show evidence of a chemical interaction of the matrix with incorporated hydrogen. Calculations indicated that the ion bombardment leads predominantly to the displacement of oxygen atoms from equilibrium positions. This oxygen can react with hydrogen ions to form OH groups offering an effective channel for the nonradiative relaxation of electron excitations in the material studied [1]. This conclusion agrees with the results of calculations devoted to the influence of hydroxy groups on the PL lifetime in bulk phosphate glasses [4]. For the level of erbium doping $N_{Er} > 5 \times 10^{19}$ cm^{-3}, the presence of OH groups introduced into the matrix under equilibrium conditions is significantly manifested at a concentration of about $N_{OH} = 5.2 \times 10^{19}$ cm^{-3}. In our case, the content of erbium ion irradiated films amounted to $N_{Er} = 2 \times 10^{20}$ cm^{-3} and the average concentration of hydrogen over the implanted layer thickness ($R_p + \Delta R_p$) was 5×10^{20} cm^{-3} (for a hydrogen ion dose of 4×10^{16} cm^{-2}), 1.1×10^{21} cm^{-3} (for an ion dose of 8×10^{16} cm^{-2}), and 4×10^{21} cm^{-3} (for an ion dose of 3×10^{17} cm^{-2}). Thus, all hydrogen ion doses provide for the conditions of OH group formation in a concentration of no less than 5×10^{20} cm^{-3}. However, it was pointed out that the influence of such groups was manifested only beginning with doses above 5×10^{16} cm^{-2}. This circumstance suggests that, under our experimental conditions, only a part (~1%) of incorporated H^+ ions form OH groups in the implanted layers.

The above results show that the irradiation of oxygen-containing phosphate films with hydrogen ions leads to a more effective PL quenching compared to that provided by helium ions. This effect can be related to the formation of OH groups by analogy with the process taking place in bulk phosphate glasses [1].

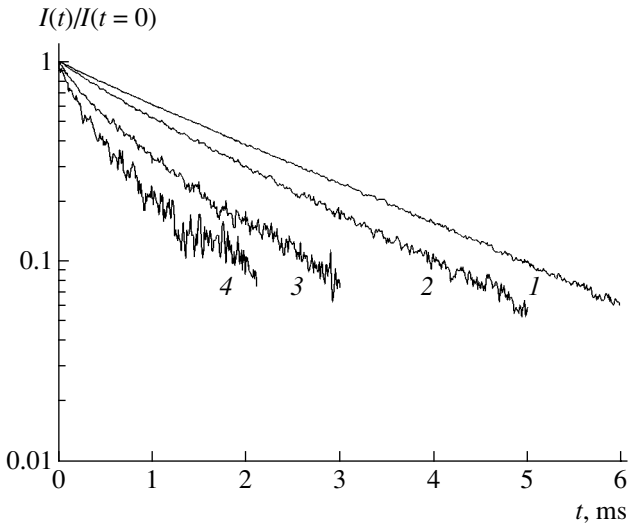

Fig. 2. The PL intensity decay kinetics in phosphate films (*1*) in the initial state and (*2–4*) upon irradiation with 70-keV hydrogen ions to a dose of $\Phi = 1 \times 10^{16}$ (*2*), 5×10^{16} (*3*), and 1×10^{17} cm^{-2} (*4*).

REFERENCES

1. *Laser Phosphate Glasses*, Ed. by M. E. Zhabotinskiĭ (Nauka, Moscow, 1980).
2. V. L. Ermolaev, E. N. Bodunov, E. B. Sveshnikova, and T. A. Shakhverdov, *Nonradiative Transfer of the Electron Excitation Energy* (Nauka, Moscow, 1977).
3. B. S. Danilin, *Application of Low-Temperature Plasma for Thin Films Deposition* (Énergoatomizdat, Moscow, 1989).
4. Y. Yan, PhD Thesis (Technical University of Eindhoven, Eindhoven, 1997).
5. N. N. Vil'chinskaya, A. V. Dmitryuk, E. G. Ignat'ev, *et al.*, Dokl. Akad. Nauk SSSR **274**, 1117 (1984).

Translated by P. Pozdeev

Technical Physics Letters, Vol. 30, No. 4, 2004, pp. 328–331. Translated from Pis'ma v Zhurnal Tekhnicheskoĭ Fiziki, Vol. 30, No. 8, 2004, pp. 53–61.

Fast Neutron Bombardment Induced Semiconductor–Metal Electron Transition in Lead Selenide

A. E. Kar'kin, V. V. Shchennikov, S. V. Ovsyannikov*, E. P. Skipetrov, and B. N. Goshchitskiĭ

Institute of Metal Physics, Ural Division, Russian Academy of Sciences, Yekaterinburg, Russia
Moscow State University, Moscow, 119899 Russia
** e-mail: sergey_v_o@imp.uran.ru*

Received July 21, 2003; in final form, October 23, 2003

Abstract—We have studied the electrical and galvanomagnetic properties of *p*-PbSe single crystals irradiated with fast neutrons. Changes in the temperature dependence of the resistivity and the Hall constant show evidence of the metal–semiconductor electron transition. Subsequent annealing at 350–390 K leads to a partial recovery of the initial properties and the reverse electron transition. © *2004 MAIK "Nauka/Interperiodica".*

The irradiation of semiconductors with high-energy particles (electrons, neutrons, protons) leads to the appearance of new energy levels in the electron spectrum, which are related to the formation of structural defects [1]. The redistribution of electrons between the main energy bands and the levels related to these defects may result in a significant variation of the chemical potential ξ, leading to a change in the density of charge carriers, the type of conductivity, and sometimes to the metal–semiconductor electron transitions [1–3]. In contrast to the case of chemical doping, which may lead to the same manifestations, the effects of irradiation can be eliminated by low-temperature annealing [3]. Thus, the irradiation with high-energy particles offers an effective method of modification and probing of the electron structure of narrow-bandgap semiconductor materials [3, 4].

This paper reports on the results of investigation of the effect of fast neutron bombardment on the electrical properties of lead selenide (*p*-PbSe). Lead chalcogenides are narrow-bandgap direct-band semiconductors widely used in photodetectors, lasers, and light-emitting diodes operating in the middle and far IR spectral range, offering the best thermoelectric properties in the intermediate temperature interval of 600–1000 K [1]. Recent investigations showed that the elements of high-sensitivity far IR (20–200 μm) detectors based on doped lead chalcogenides can successfully compete with the analogues based on the classical materials—germanium and silicon [5]. In advantage to the latter materials, lead chalcogenides possess a much higher radiation resistance, which is related to a high density of states stabilizing the Fermi level [5]. PbSe is characterized by a minimum bandgap width ($E_g \approx 0.27$ eV) in comparison to the other lead chalcogenides [1].

The experiments were performed on *p*-PbSe single crystals with a hole density of $p = 2 \times 10^{18}$ cm^{-3}. The samples were irradiated with fast neutrons possessing energies above 1 MeV to a fluence of $\Phi = 1 \times 10^{19}$ cm^{-2} at a temperature of $T = 320 \pm 5$ K. After irradiation, the electrical contacts were ultrasonically applied to the samples with an indium-based solder. The resistivity ρ and the Hall constant R were measured by the conventional Montgomery technique (representing a modification of the Van der Pauw method) in a broad range of temperatures T = 1.7–390 K and stationary magnetic fields B = 0–13.6 T in a special setup (Oxford Instruments) [3]. The neutron-irradiated samples were subjected to sequential annealings at temperatures up to $T \approx 390$ K. Treatments at higher temperatures were not performed because of the possible diffusion of indium from contacts into the sample bulk.

The irradiation of *p*-PbSe single crystals with fast neutrons led to an increase in ρ and to reversal of the sign of the temperature coefficient of resistance, which is evidence of a transition of the metal–semiconductor type (Fig. 1). The transition was accompanied by a sharp growth of the Hall constant R and a change in its temperature dependence, which acquired a nonmonotonic character (these data are not presented here). Subsequent annealing showed a tendency to restoration of the initial properties (Figs. 1, 2). The temperature dependences of the resistance of two neutron-irradiated samples exhibited a local minimum at $T \approx 80$ K, which shifted toward higher temperatures in the course of annealing (Fig. 1b).

For a qualitative description of the observed kinetic effects, we used simple expressions valid within the

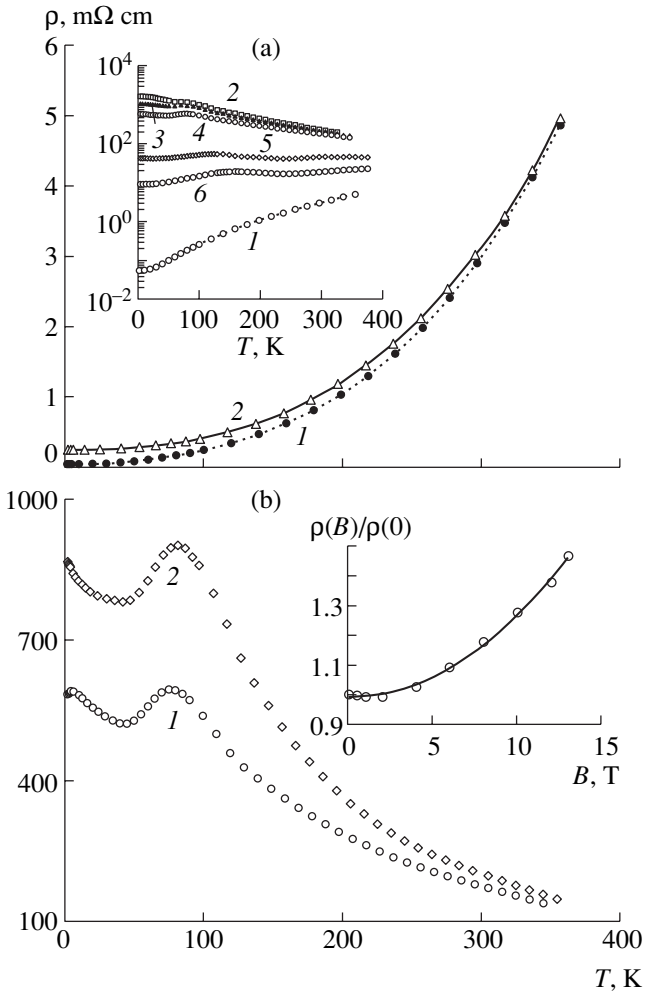

Fig. 1. The temperature dependence of the resistivity of *p*-PbSe (sample N1) (a) before neutron irradiation and (b) after the irradiation and annealing at T = 360 K: (*1*) B = 0; (*2*) B = 13.6 T. The inset to Fig. 1a shows semilogarithmic plots of the resistivity versus temperature after 20-min annealings: (*1*) before irradiation; (*2*) after irradiation with fast neutrons to $\Phi = 1 \times 10^{19}$ cm^{-2}; (*3–6*) after subsequent annealings at T = 350 (*3*), 360 (*4*), 370 (*5*), and 380 K (*6*). The inset to Fig. 1b shows the relative variation of resistivity in a magnetic field at T = 4.2 K.

framework of a single-band model for weak magnetic fields [6, 7],

$$R = \frac{a_r}{ep}; \quad (1)$$

$$\frac{\Delta\rho}{\rho} = (\mu B)^2 A_r, \quad (2)$$

where R is the Hall constant, a_r and A_r are constant quantities depending on the scattering parameter r, $\Delta\rho/\rho$ is the magnetoresistance, p is the hole density, and μ is the hole mobility.

Using formulas (1) and (2), we estimated the hole mobility from the results of measurements of the Hall

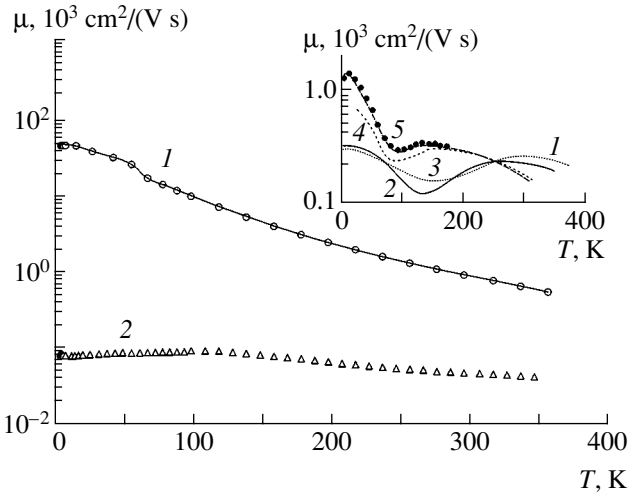

Fig. 2. The temperature dependence of the hole mobility in *p*-PbSe (sample N1) determined from (*1*) the Hall effect and (*2*) the magnetoresistance measurements after irradiation and annealing (see the text): (*1*) before irradiation; (*2*) after irradiation with fast neutrons to $\Phi = 1 \times 10^{19}$ cm^{-2} and subsequent annealing for 20 min at T = 360 K. The inset shows the temperature dependences of the Hall mobility in *p*-PbSe (sample N2): (*1*) after irradiation to $\Phi = 1 \times 10^{19}$ cm^{-2}; (*3–6*) after subsequent annealings for 120 min at T = 340 (*2*), 355 (*3*), 370 (*4*), and 385 K (*5*).

effect $\mu_H = R/\rho$ and the magnetoresistance $\Delta\rho/\rho$ (Fig. 2). In the initial state, holes are degenerate and obey the Fermi–Dirac statistics. For this reason, the Hall factor a_r in formula (2) tends to unity and the coefficient $A_r = (\pi^2/3)(kT/\xi)^2 r^2$ is inversely proportional to the square of the degree of degeneracy ξ/kT, where k is the Boltzmann constant and ξ is the chemical potential [6]. The values of mobility estimated using formula (2) from the temperature dependence of ρ in the magnetic fields B = 0 and 13.6 T (Fig. 1a) were about two orders of magnitude lower than the Hall mobilities μ_H, which is explained by the smallness of the ignored coefficient $A_r \ll 1$. The temperature dependence of μ evaluated from data on the Hall effect (Fig. 2) and the magnetoresistance (not presented) are mutually consistent if the variation of A_r with increasing temperature T is taken into account. In the region of $T \geq 50$ K, the $\mu(T)$ curves (Fig. 2) correspond to the case of scattering on acoustic phonons ($r = -1/2$) [1].

The magnetoresistance of irradiated samples exhibited a quadratic dependence on the magnetic field B (see the inset in Fig. 1b). For this reason, it was possible to determine the hole mobility with sufficiently high accuracy using formula (2) and the $\rho(T)$ curves measured at B = 0 and 13.6 T (Fig. 1b). The mobilities μ evaluated from the magnetoresistance data and the Hall effect (for $A_r = 0.61$ and $a_r = 1.18$ corresponding to the scattering on acoustic phonons) exhibited identical temperature variation at high ($T > 200$ K) temperatures (Fig. 2). At the same time, their behavior in the region

of $T \approx 100$ K significantly differed, which was indicative of the possible contribution due to charge carriers of another type [6] not taken into account by formula (1). We believe that charge carriers of the second type in the irradiated samples are electrons at the defect levels.

After the neutron irradiation, the hole mobility exhibited a decrease (Fig. 2). The temperature dependence of the hole mobility in irradiated samples, estimated from the results of magnetoresistance measurements, can be approximated by a curve calculated with allowance of a mixed mechanism of scattering on acoustic phonons (at high temperatures) and charged centers (at low temperatures) [6]. The hole mobility increased with the annealing temperature (Fig. 2), which reflected a decrease in the density of defects.

The main features of the metal–semiconductor transition in *p*-PbSe revealed by our experiments coincide with those of the analogous transitions observed previously under the action of irradiation or chemical substitution in other narrow-bandgap materials, such as $HgTe_{1-x}S_x$ [7] and Bi_2Te_3 [3], with different crystal and electron structures. The metal–semiconductor transitions in these substances are reversible and the temperature dependence of resistance is displayed by a series of like curves with variable slopes (see the inset in Fig. 1a) [3, 7]. The curves of $R(T)$ and $\rho(T)$ usually exhibit local maxima reflecting the two-band character of the conductivity [3, 7, 8]. Differences between the experimental curves of $R(T)$ for these materials are mostly related to the different values of E_g.

The temperature dependences of the resistance and the Hall constant of *p*-PbSe single crystals can be adequately described, especially in the range of $T > 100$ K, in terms of the model of a two-band semiconductor with impurities, where the densities of electrons (n) and holes (p) are given by the expressions [8, 9]

$$n = \frac{n_0}{2} + \left[\left(\frac{n_0}{2}\right)^2 + (4A_cA_v)^2\exp\left(-\frac{E_g}{kT}\right)\right]^{1/2},$$
$$p = -\frac{n_0}{2} + \left[\left(\frac{n_0}{2}\right)^2 + (4A_cA_v)^2\exp\left(-\frac{E_g}{kT}\right)\right]^{1/2}. \quad (3)$$

Here, n_0 is the difference between the concentrations of donor and acceptor impurities; E_g is the thermal semiconductor bandgap width; and A_c and A_v are the densities of states in the electron (conduction) and hole (valence) bands depending on the temperature as $A_{c,v} \sim T^{3/2}$ for a simple parabolic dispersion law. Relations (3) explain the decrease in ρ and R with increasing temperature even for $E_g = 0$ (zero-bandgap semiconductors [7]). In $HgSe_{1-x}S_x$, where the conduction and valence bands overlap, the irradiation cannot reduce the electron density below the limiting level of $\sim 2 \times 10^{17}$ cm^{-3} [8]. In Bi_2Te_3 possessing a small semiconductor bandgap width $E_g = 0.145$ eV, the irradiation with fast electrons changes the conductivity type from *p* to *n*, whereby the chemical potential level ξ raises from the valence band to the conduction band, and alters the sign of n_0 in formulas (3) [3]. In *p*-PbSe, where the semiconductor bandgap width is twice as large, the chemical potential ξ level remains at the valence band top and the hole conductivity type is retained.

It was established [4, 10–16] that the irradiation of narrow-bandgap semiconductors with high-energy particles (electrons, protons, α particles) allows the charge carrier density to be varied within broad limits and even the conductivity type to be changed (from *p* to *n*). The positions of energy states related to the radiation defects produced by the electron bombardment of PbSe were studied using galvanomagnetic measurements at a high hydrostatic pressure [16]. In lead selenide and lead alloys, the irradiation with electrons, protons, or α particles produces defects related to vacancies in the selenium sublattice and possessing donor properties. For this reason, the irradiation leads to an increase in the electron density and to inversion of the conductivity type [4]. However, the inversion $p \longrightarrow n$ does not take place in materials with a high density of holes ($p \geq 5 \times 10^{17}$ cm^{-3}) [14], which suggests that there exists a limiting density of donors ($n \sim 10^{17}$ cm^{-3}) that can be created by such irradiation [4].

Since our single crystals of *p*-PbSe possessed a higher density of holes (2×10^{18} cm^{-3}), it becomes clear why the neutron irradiation did not change the type of conductivity. The high density of charge carriers in lead chalcogenides is usually related to deviations from stoichiometry [1, 4, 13], which provide for a large value of n_0 in formulas (3). As can be seen from Figs. 1 and 2, the hole density p decreases upon neutron irradiation but still remains positive because the amount of introduced donors is significantly lower than n_0.

The gradual recovery of the initial properties in the course of annealing of the irradiated lead chalcogenide observed in our experiments agrees with the data reported previously by other researchers (see, e.g., [4]) for the same temperature interval (360–400 K). A decrease in the mobility of holes (especially pronounced at low temperature) in *p*-PbSe in the course of the metal–semiconductor transition upon irradiation and during subsequent annealing reflects a high density of radiation defects. A similar decrease in μ was observed for $HgSe_{1-x}S_x$ during a transition from zero-bandgap semiconductor to semimetal with increasing concentration of sulfur atoms playing the role of additional structural defects [7]. Variations (usually not greater than twofold) in the carrier mobility in PbSe crystals were also observed for the other types of radiation (electrons, protons, α particles) [4]. In our experiments, a decrease in μ upon the irradiation was much more pronounced (Fig. 2). This fact indicates that the conductivity of irradiated samples is related to the states in disordered regions of the crystal. However, the absolute values of μ after the neutron irradiation are still high (Fig. 2). Based on the observed $\mu(T)$ curves,

we may suggest that the thermoelectric quality and efficiency of *p*-PbSe in the working temperature range $T > 600$ K will also not be significantly decreased by irradiation.

The results of our experiments model changes in the electron structure and charge carrier parameters taking place in PbSe upon the introduction of various concentrations of impurities and radiation defects (including those for the radiation of other types) [4]. These data can be used for the development of the technology of production of thermoelectric and optoelectronic devices based on this material.

Acknowledgments. This study was supported by the Ministry of Industry, Science, and Technology of the Russian Federation (State Contract no. 40.012.1.1.1166, project no. 06/03, physics), the "Quantum Macrophysics" Program of the Russian Academy of Sciences, the Presidential Grant for Support of the Leading Scientific Schools of Russia (project no. NSh-639.2003.2), and the Russian Foundation for Basic Research (project no. 01-02-17203).

REFERENCES

1. Yu. I. Ravich, B. A. Efimova, and I. A. Smirnov, *Semiconducting Lead Chalcogenides* (Nauka, Moscow, 1968; Plenum Press, New York, 1970).
2. N. B. Brandt and E. P. Skipetrov, Fiz. Nizk. Temp. **22**, 870 (1996) [Low Temp. Phys. **22**, 665 (1996)].
3. A. E. Kar'kin, V. V. Shchennikov, B. N. Goshchitskiĭ, *et al.*, Zh. Éksp. Teor. Fiz. **113**, 1787 (1998) [JETP **86**, 976 (1998)].
4. V. V. Kozlovskiĭ, *Modification of Semiconductors by Proton Beams* (Nauka, St. Petersburg, 2003) [in Russian].
5. B. A. Volkov, L. I. Ryabova, and D. R. Khokhlov, Usp. Fiz. Nauk **172**, 875 (2002).
6. B. M. Askerov, *Kinetic Effects in Semiconductors* (Nauka, Leningrad, 1970).
7. V. V. Shchennikov, A. E. Kar'kin, N. P. Gavaleshko, and V. M. Frasunyak, Fiz. Tverd. Tela (St. Petersburg) **42**, 210 (2000) [Phys. Solid State **42**, 215 (2000)].
8. A. E. Kar'kin, V. V. Shchennikov, S. E. Danilov, *et al.*, Fiz. Tekh. Poluprovodn. (St. Petersburg) **37**, 1316 (2003) [Semiconductors **37**, 1278 (2003)].
9. W. Paul and D. M. Warchawer, *Solids under Pressure* (McGraw-Hill, New York, 1963; Mir, Moscow, 1966).
10. J. P. Donnelly, T. C. Harman, and A. G. Foyt, Appl. Phys. Lett. **18**, 259 (1971).
11. T. F. Tao, C. C. Wang, and J. W. Sunier, Appl. Phys. Lett. **20**, 235 (1972).
12. C. C. Wang, T. F. Tao, and J. W. Sunier, J. Appl. Phys. **45**, 3981 (1974).
13. V. N. Brudnyĭ, A. V. Voĭtsekhovskiĭ, M. A. Krivov, *et al.*, Fiz. Tekh. Poluprovodn. (Leningrad) **12**, 1495 (1978) [Sov. Phys. Semicond. **12**, 885 (1978)].
14. Yu. N. Kazarinov and V. N. Lomasov, Fiz. Tekh. Poluprovodn. (Leningrad) **23**, 177 (1989) [Sov. Phys. Semicond. **23**, 111 (1989)].
15. D. M. Freik, A. G. Mikolaĭchuk, and Ya. V. Ogorodnik, Fiz. Tverd. Tela (Leningrad) **32**, 2742 (1990) [Sov. Phys. Solid State **32**, 1589 (1990)].
16. N. B. Brandt, B. B. Kovalev, and E. P. Skipetrov, Semicond. Sci. Technol. **6**, 487 (1991).

Translated by P. Pozdeev

Technical Physics Letters, Vol. 30, No. 4, 2004, pp. 332–334. Translated from Pis'ma v Zhurnal Tekhnicheskoĭ Fiziki, Vol. 30, No. 8, 2004, pp. 62–67.

A Planar Prism for Detection and Selective Excitation of Modes in a Multimode Channel Waveguide

D. V. Svistunov

Vavilov Optical Institute, State Scientific Center of the Russian Federation, St. Petersburg, 199034 Russia

e-mail: svistunov@mail.ru

Received September 19, 2003

Abstract—A fully planar element for selective excitation and detection of various modes in a multimode channel waveguide has been manufactured and tested. A mode multiplexer/demultiplexer based on this element will provide for the mode data compression in fiber-optic communication lines employing multimode fibers. © *2004 MAIK "Nauka/Interperiodica".*

This paper addresses the problem of increasing informative capacity of the fiber-optic communication lines employing multimode fibers. In recent years, research has been directed to selective excitation of and data transmission via a single mode of a multimode fiber (see, e.g., [1–4]). However, using selective excitation of modes, it is possible to provide for an additional increase in the informative capacity of a communication line. This can be achieved by application of the method of mode data compression, whereby groups of selected modes are used as independent data transmission channels.

Unfortunately, the development of this method is hindered by the lack of effective means of selectively exciting modes in a multimode fiber. The available devices are mostly intended for excitation of the lowest modes, while selective excitation of the other modes leads to significant complication and the loss of efficiency of such systems [1–6]. Moreover, most of the known devices cannot simultaneously and independently excite the modes of various orders. Some devices are rather sophisticated and their implementation is still in the stage of calculation of the design parameters and working characteristics [6, 7].

Recently [8], a new approach to the selective excitation of modes in optical fibers has been proposed based on a passive integrated optics device called the mode multiplexer/demultiplexer. According to this, the selective excitation of modes in a multimode fiber is achieved through the excitation of desired modes in a multimode channel waveguide optically matched with the fiber. The device comprises a multimode channel waveguide, a planar selective coupling element, and a set of single-mode channel waveguides acting as separate input/output data channels. The selective element provides for the optical coupling of each preset mode of the multimode channel waveguide to the corresponding separate single-mode channel waveguide, thus ensuring selective excitation and detection of separate modes of a multimode channel waveguide.

This Letter presents the results of experiments with the first prototypes of the new planar selective coupling element.

Figure 1 presents a schematic diagram of the selective element and shows the ray tracing in the regime of detecting modes of a multimode channel fiber. The selective coupling element is a passive, fully planar device designed as a longitudinal coupling element. The principle of operation is essentially the same as that of an input/output prism widely used in integrated optics. The function of a bulk prism in this device is performed by a single-mode planar waveguide region with a refractive index increased relative to that of the channel waveguide. In this scheme, each mode of the channel waveguide forms a directed beam in the plane of the planar element, the beams of different modes being directed at various angles relative to the channel

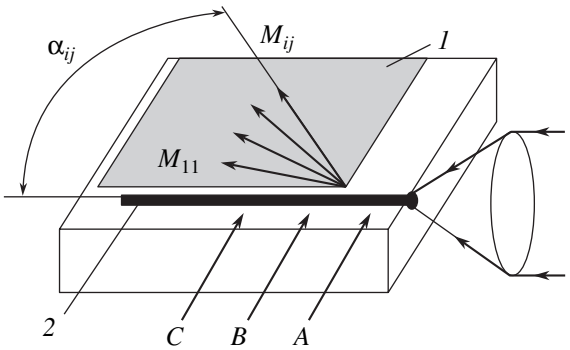

Fig. 1. Schematic diagram illustrating operation of the selective coupling element in the regime of detecting modes of a channel waveguide: (*1*) single-mode planar prism; (*2*) multimode channel waveguide (see the text for explanations).

1063-7850/04/3004-0332$26.00 © 2004 MAIK "Nauka/Interperiodica"

waveguide axis. The angle of deviation α_{ij} for each beam is determined from a simple relation $\cos(\alpha_{ij}) = N_{ij}/N_p$, where N_{ij} and N_p are the effective refractive indices of the given mode M_{ij} of the channel waveguide and the mode propagating in the single-mode planar region, respectively. The higher the mode order of the channel waveguide (i.e., the lower the N_{ij} value), the greater the sloping angle α_{ij}. Thus, the selective coupling element provides for the spatial separation of converted modes of the channel waveguide depending on the mode order. This allows the proposed element to be used as a mode demultiplexer for separating the mode data channels.

Owing to the principle of reversibility of passive optical elements, the proposed selective coupling element can also be used as the mode multiplexer. In this case, the optical excitation in the reverse direction is performed by planar beams propagating at the angles α_{ij} relative to the channel waveguide axis. Arriving at the tunneling region of the planar prism, each beam excites a mode of the corresponding order in the multimode channel waveguide. By independently exciting the modes of various orders, it is possible to obtain several independent mode data channels in the same channel waveguide, thus providing for the mode compression of data.

The samples were prepared by means of ion exchange in the substrates of commercial glass K8. Multimode channel waveguides were formed in a KNO_3 melt. Single-mode planar prisms were obtained using melts containing 0.2–0.5% $AgNO_3$. The prototype operation in the regime of mode detection was studied by focusing a light beam on the edge of a multimode channel waveguide, which simultaneously excited a set of modes of various orders. The mode composition was checked with the aid of a usual input/output coupling prism. The patterns of modes extracted from the waveguide structure were observed on a transverse screen and monitored by photodetector array. By sequentially placing the control prism in various sites (indicated by arrows *A*–*C* in Fig. 1) along the selective element, it was possible to observe gradual passage of the radiation power from modes of the channel waveguide to the corresponding planar beams.

These observations showed that the selective coupling element operates as a longitudinal distributed optical coupling device. Measurements performed at the end of the coupling element confirmed complete conversion of the channel waveguide modes into the corresponding planar beams. Figure 2 shows the typical oscillogram of an output signal of the photodetector array registering a series of spatially separated planar beams outcoupled by the control prism located at site *C* (Fig. 1). Each peak displays the transverse intensity profile of the corresponding planar beam representing a solitary mode of the channel waveguide. As can be seen, the beams are quite well spatially resolved and can be readily selected. The rightmost peak in Fig. 2

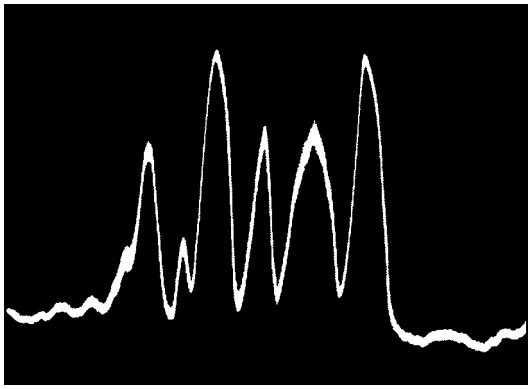

Fig. 2. The typical pattern of intensity distribution for several planar beams separated by the selective coupling element and measured using a photodetector array.

corresponds to the fundamental mode of the channel waveguide. The beam divergence in the planar waveguide was estimated by the results of measurements of the divergence of the beams extracted from the waveguide taking into account the experimentally determined values of N_p. For various samples, the angles of divergence of separate planar beams fell within 5′–10′ at a total angular width of the set of beams (including five to eight beams) reaching 2°. The angular spacing of beams corresponding to the low-order channel modes coupled to the planar waveguide was within 15′–30′.

Thus, the proposed device provides for the effective spatial selection of modes of the channel waveguide with respect to the mode order. Note that, by analogy with traditional prism couplers, the angular width of the set of beams and the angular spacing of beams can be increased by decreasing the difference between N_p and N_{ij}. In practice, the difference $N_p - N_{11}$ for the lowest-order mode should be reduced to a minimum level reliably reproduced by the available technology used for the fabrication of planar elements.

In order to check for operation of the coupling element in the regime of selective mode excitation in the channel waveguide, a planar light beam was fed into the planar prism by means of a usual input/output prism coupler in position *C* (Fig. 1). The pattern of modes excited in the channel waveguide was observed using another control prism located in position *A*. By varying the angle of incidence of the planar beam relative to the channel waveguide axis, it was possible to provide for the conditions of matching (α_{ij}) of the given planar mode and the modes of various orders in the channel waveguide. The planar selective coupling element has proved to be capable of sequentially exciting separate modes in the multimode channel waveguide.

In conclusion, the experimental samples of a new, fully planar selective coupling element based on a planar prism showed performance in the regimes of selec-

tive excitation and detection of modes of a multimode channel waveguide. Using such elements in the scheme of mode multiplexer/demultiplexer will provide for the effective mode data compression in fiber-optic communication lines.

REFERENCES

1. G. Yabre, J. Lightwave Technol. **18**, 668 (2000).
2. Z. Haas and M. A. Santoro, J. Lightwave Technol. **11**, 1125 (1993).
3. L. Ruddatz, I. H. White, D. G. Cunningham, and M. C. Nowell, J. Lightwave Technol. **16**, 324 (1998).
4. C. K. Asawa, J. Lightwave Technol. **20**, 10 (2002).
5. T. Isnigure, M. Kano, and Y. Koike, J. Lightwave Technol. **18**, 959 (2000).
6. L. Vaissie and E. G. Johnson, Opt. Eng. **41**, 1821 (2002).
7. Y. Kawaguchi and K. Tsutsumi, Electron. Lett. **38**, 1701 (2002).
8. D. V. Svistunov, in *Proceedings of the 5th International Conference "Applied Optics," St. Petersburg, 2002*, Vol. 2, pp. 116–118.

Translated by P. Pozdeev

Technical Physics Letters, Vol. 30, No. 4, 2004, pp. 335–337. Translated from Pis'ma v Zhurnal Tekhnicheskoĭ Fiziki, Vol. 30, No. 8, 2004, pp. 68–74.

The Effect of Applied Voltage on the Formation of a Subnanosecond Electron Beam in a Gas-Filled Diode

V. F. Tarasenko[a,*], S. I. Yakovlenko[b,], V. M. Orlovskiĭ[a], and A. N. Tkachev[b]**

[a] *Institute of High-Current Electronics, Siberian Division, Russian Academy of Sciences, Tomsk, Russia*

[b] *Institute of General Physics, Russian Academy of Sciences, Moscow, 117924 Russia*

*e-mail: * VFT@loi.hcei.tsc.ru; ** syakov@kapella.gpi.ru*

Received November 10, 2003

Abstract—We have studied the effect of the magnitude of the voltage applied to a gas-filled diode on the formation of a subnanosecond pulsed electron beam at atmospheric pressure. It is theoretically demonstrated that an increase in the interelectrode voltage leads to a decrease in the charge transferred by the beam. This may result in a decrease in the amplitude of the beam current at a pulse duration below the time resolution of the detection system. © *2004 MAIK "Nauka/Interperiodica".*

Introduction. Recently [1–6], we demonstrated that subnanosecond electron beams with current amplitudes reaching tens and hundreds of amperes and energies of up to several tens or hundreds of kiloelectronvolts can be obtained in gas diodes filled with helium, air, nitrogen, or CO_2–N_2–He mixtures at atmospheric pressure driven by voltage pulses with short leading fronts. It should be noted that the beam current amplitudes obtained previously in gas-filled diodes at atmospheric pressure (see review [9]) did not exceed a fraction of an ampere. It was theoretically shown [7, 8] that the criterion of electron runaway in gas discharge exhibits a substantially nonlocal character and corresponds to a situation when the electron multiplication length (equal to the inverse Townsend coefficient [10]) is comparable with the interelectrode distance. It was established [3] that, as the pulse generator voltage amplitude and the voltage drop across the gap increase, the electron beam current behind the foil first increases but then begins to decrease.

This study was aimed at elucidating the effect of the magnitude of the voltage applied to a gas-filled diode on the beam current amplitude and at establishing factors responsible for a decrease in the beam current with increasing electric field in the discharge gap.

Experimental setup. The experiments were performed with the nanosecond pulse generator RADAN-303 [11] having an output wave impedance of 45 Ω, which produced voltage pulses with an amplitude from 50 to 170 kV in a matched load (in the open circuit regime, the amplitude reached 340 kV). The voltage pulses had a full width at half maximum (FWHM) of ~5 ns and a front width of ~1 ns. With this generator, the voltage applied to the discharge gap could be smoothly controlled by varying the gap width. The gas-filled diode design was similar to that described in detail elsewhere [1–4, 6]. The electron beam was extracted from the diode via a ~40-μm-thick AlBe foil or via a grid with a geometric transparency of ~20%. The cathode–anode spacing in this system could be set within 13–20 mm. The diode was filled with air at atmospheric pressure. Signals from a capacitive voltage divider, the electron beam collectors, and shunts were measured using a digital oscillograph of the TDS-684B type with a bandwidth of 1 GHz and a sensitivity of 5 G/s (which corresponds to 5 points/ns). The discharge was photographed using a digital camera.

Experimental results. Similar to what was reported in [1–6], an electron beam with a current amplitude of several tens of amperes was obtained at atmospheric pressure within a short front of a voltage pulse generating an inhomogeneous electric field in the air-filled diode with small-size cathode. The discharge in the gap had the form of volume columns based on bright cathode spots. The discharge current amplitude reached several kiloamperes and was dependent on the drive generator voltage. The electron beam arose at the voltage pulse front and had an FWHM not exceeding 0.3 ns (Fig. 1).

We have thoroughly studied the dependence of the beam current on the generator voltage for the diodes with foil and grid anodes. In both series of measurements, the beam current exhibited a decrease when the generator voltage exceeded 210 kV. Figure 2 shows plots of the beam current behind the foil or grid versus open-circuit voltage of the generator. Under the conditions studied in this work (as well as in the experiments described in [3]), both the voltage drop on the discharge gap and the discharge current initially increased in proportion to the open-circuit voltage of the generator. Photographs of the discharge gap showed that the shape of discharge did not significantly change when the generator voltage was varied. Thus, for a given interelectrode distance and the same cathode, the electron beam

1063-7850/04/3004-0335$26.00 © 2004 MAIK "Nauka/Interperiodica"

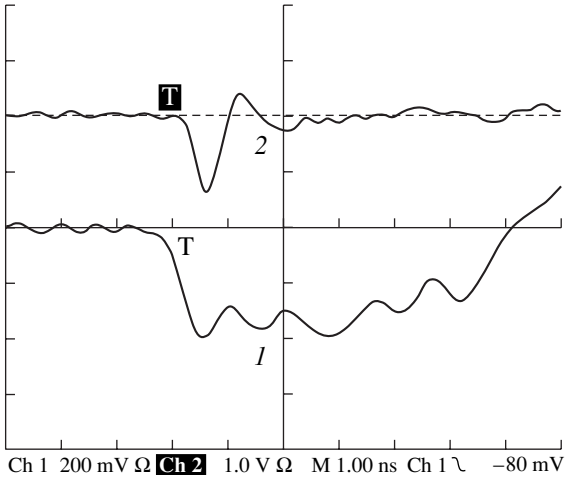

Fig. 1. Oscillograms of (*1*) the voltage and (*2*) the electron beam current in a gas-filled diode (voltage amplitude scale, 45 kV/div; current amplitude scale, 20 A/div; time scale, 1 ns/div).

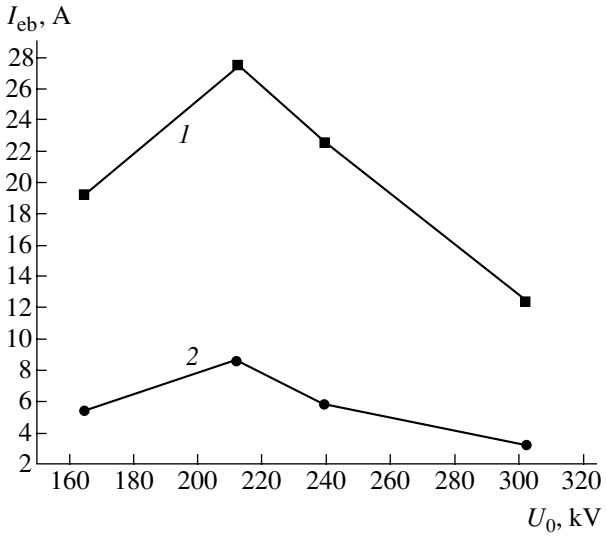

Fig. 2. Plots of the electron beam current I_{eb} behind (*1*) a 40-μm-thick AlBe foil and (*2*) a grid with a geometric transparency of 20% versus the open-circuit voltage U_0 of the generator.

current started decreasing when the voltage applied to the discharge gap exceeded a certain threshold.

It should be noted that, when the beam current reached the maximum, the voltage drop on the gas diode ceased to change significantly and the beam current rapidly vanished. This fact indicates that the optimum conditions for the electron beam formation are retained only during a very short period time, within fractions of a nanosecond.

Theoretical model and results. According to the experimental data reported previously [3], ionization in the discharge gap is inhomogeneous, whereby the ionization regions appears as jets. Such a jet can be modeled by a circular sector of the cylindrical geometry. In order to elucidate the mechanism of breakdown in the discharge gap, we used a one-dimensional diffusion–drift model described in detail in [12]. According to this model, ionization takes place between coaxial cylindrical electrodes with $r_0 < r < r_1$, where r_0 and r_1 are the radii of the internal and external electrodes, respectively. The plasma formation and the electric field screening were described in terms of the equations of momentum transfer, the equations of continuity for electrons and ions, and the Poisson equation for the electric field strength. The field dependences of various quantities entering into the model equations (ionization frequencies, drift velocities, diffusion coefficients) were described using approximated relations obtained in [13].

The results of calculations showed that, in the case of almost flat electrodes ($d = r_1 - r_0 \ll r_1$), the ionization wave propagation is possible only for sufficiently low voltages and, hence, small Townsend multiplication coefficients α_i ($\alpha_i d < 1$). For such electrodes, propagation of the ionization wave from cathode to anode appears only when an initial excess ionization takes place in a certain region near the cathode. Indeed, bright plasma formations were experimentally observed near the cathode in all regimes. The condition of appearance of the ionization wave corresponds to a situation when electrons leave the discharge gap without significant multiplication. Otherwise ($\alpha_i d \gg 1$), the rate of bulk ionization exceeds the rate of electron drift and the wave does not travel over a significant distance during the ionization period.

In the case of electrodes having the shape of coaxial cylinders with a small radius of the cathode ($d = r_1 - r_0 \gg r_0$), the ionization wave is formed for both small and large voltages and propagates due to the field inhomogeneity rather than the electron drift: the greater the field strength, the higher the ionization rate. In such regions, the plasma density rapidly grows to a level corresponding to the field screening, after which the ionization rate ceases to increase.

The wave of ionization in an inhomogeneous field is illustrated in Fig. 3. Note that the wave of increasing plasma density is preceded by the wave of increased electric field strength at the anode. An analogous calculation was carried out for the same conditions and the voltage $U(t)$ doubled for the times $t > 1$ ns. The results were qualitatively similar to those presented in Fig. 3 for the lower voltage. Despite a twofold increase in the voltage, the field strength near the anode at the time of arrival of the ionization wave did not change substantially. However, the time of the ionization wave travel to anode significantly decreased.

The results of model calculations allow the mechanism of the electron beam formation to be outlined as follows. Following [3], we assume that electrons involved in the beam are formed within a near-anode layer with a thickness of $\sim 1/\alpha_i$. This take place when

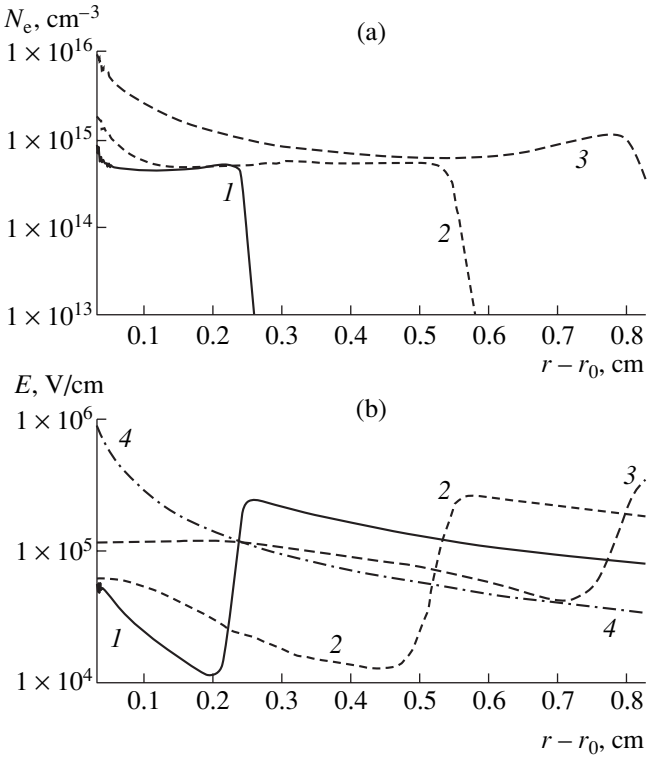

Fig. 3. Radial profiles of (a) the electron density N_e and (b) electric field strength E at the moments of time when the ionization wave approaches the anode: t = 1.3 (*1*), 1.4 (*2*) and 1.5 ns (*3*); curve (*4*) shows the field strength profile in the empty space calculated by the formula $E(r) = -U/(r\ln(r_0/r_1))$ for U = 100 kV, r_0 = 0.25 mm, and r_1 = 8 mm. The voltage applied to electrodes $U(t)$ varies with time as depicted in Fig. 1.

the ionization wave reaches the anode and the field strength in this layer increases. However, arrival of the ionization wave to the anode leads to a sharp drop in the field strength in this region, although the voltage between electrodes remains unchanged. Obviously, this breaks the conditions of beam generation.

As for a decrease in the beam current with increasing peak voltage applied to the electrodes (Fig. 2), it would apparently be more correct to speak of a decrease in the amount of charge transferred by the beam rather than in the current as such. Indeed, it was experimentally impossible to determine current pulse durations below 0.3 ns. Therefore, even if the beam current is greater, while the transferred charge is smaller because of a short pulse duration (below 0.3 ns), the result will appear as a decrease in the beam current because of the finite time resolution of the detection system. A decrease in the charge transferred by the beam with an increase in the applied voltage can be explained by a decrease in the time required for the ionization wave to travel over the region of electron beam generation within a near-anode layer having a thickness of ~$1/\alpha_i$. This possibility is qualitatively confirmed by the results of model calculations.

Conclusions. The results of our experiments confirmed that, as the electric field strength in the discharge gap grows, the electron beam current in the gas-filled diode initially increases, reaches a maximum, and begins to decrease. An analysis of the theoretical model adopted shows that an increase in the voltage applied to the electrodes leads to a decrease in the charge transferred by the beam. This may appear as a decrease in the current amplitude if the current pulse duration is smaller than the time resolution of the detection system (0.3 ns in this study). Thus, by varying the voltage applied to a gas diode, it is possible in principle to control the duration of subnanosecond current pulses.

Acknowledgments. The authors are grateful to V.G. Shpak for kindly providing the RADAN-303 generator and to S.A. Shunailov for his help in conducting this study.

REFERENCES

1. V. F. Tarasenko, V. M. Orlovskiĭ, and S. A. Shunailov, Izv. Vyssh. Uchebn. Zaved., Fiz. **46** (3), 94 (2003).
2. S. B. Alekseev, V. M. Orlovskiĭ, and V. F. Tarasenko, Pis'ma Zh. Tekh. Fiz. **29** (10), 29 (2003) [Tech. Phys. Lett. **29**, 411 (2003)].
3. V. F. Tarasenko, S. I. Yakovlenko, V. M. Orlovskiĭ, *et al.*, Pis'ma Zh. Éksp. Teor. Fiz. **77**, 737 (2003) [JETP Lett. **77**, 611 (2003)].
4. S. B. Alekseev, V. P. Gubanov, V. M. Orlovskiĭ, *et al.*, Prib. Tekh. Éksp., No. 4, 81 (2003).
5. S. B. Alekseev, V. M. Orlovskiĭ, V. F. Tarasenko, *et al.*, Pis'ma Zh. Tekh. Fiz. **29** (16), 29 (2003) [Tech. Phys. Lett. **29**, 679 (2003)].
6. V. F. Tarasenko, V. G. Shpak, S. A. Shunailov, *et al.*, Pis'ma Zh. Tekh. Fiz. **29** (21), 1 (2003) [Tech. Phys. Lett. **29**, 879 (2003)].
7. A. N. Tkachev and S. I. Yakovlenko, Pis'ma Zh. Éksp. Teor. Fiz. **77**, 264 (2003) [JETP Lett. **77**, 221 (2003)].
8. A. N. Tkachev and S. I. Yakovlenko, Pis'ma Zh. Tekh. Fiz. **29** (16), 54 (2003) [Tech. Phys. Lett. **29**, 683 (2003)].
9. L. P. Babich, T. V. Loĭko, and V. A. Tsukerman, Usp. Fiz. Nauk **160** (7), 49 (1990) [Sov. Phys. Usp. **33**, 521 (1990)].
10. Yu. P. Raizer, *Gas Discharge Physics* (Nauka, Moscow, 1992; Springer-Verlag, Berlin, 1991).
11. M. I. Yalandin and V. G. Shpak, Prib. Tekh. Éksp., No. 3, 5 (2001).
12. A. N. Tkachev and S. I. Yakovlenko, Laser Phys. **12**, 1221 (2002).
13. A. N. Tkachev and S. I. Yakovlenko, Laser Phys. **12**, 1022 (2002).

Translated by P. Pozdeev

Technical Physics Letters, Vol. 30, No. 4, 2004, pp. 338–340. Translated from Pis'ma v Zhurnal Tekhnicheskoĭ Fiziki, Vol. 30, No. 8, 2004, pp. 75–80.

Dispersion of the Plastic Strain Localization Waves

S. A. Barannikova

Institute of Strength Physics and Materials Science, Siberian Division, Russian Academy of Sciences, Tomsk, 634055 Russia

e-mail: bsa@ms.tsc.ru

Received July 28, 2003; in final form, October 20, 2003

Abstract—The main laws of the macroscopic localization of plastic straining in a bcc alloy Fe–3% Si on the stage of linear strain hardening are considered. It is established that the strain localization exhibits a wave character and the velocity of propagation of the strain localization wave is determined. The law of dispersion of the waves of localized plastic straining is found for polycrystalline aluminum and for iron-based alloys in both single crystal and polycrystalline states. © *2004 MAIK "Nauka/Interperiodica".*

As is known [1], the process of plastic straining in metals and alloys exhibits a localized character in all stages of plastic flow. In recent years, it was established that different forms of the macroscopic inhomogeneity of plastic straining are sequentially manifested on the passage along the $\sigma(\varepsilon)$ (stress–strain) curve [2, 3]. Experiments performed for a sufficiently broad class of pure metals and alloys in both single crystal and polycrystalline states showed that there exists a unique relationship between the character of plastic strain localization and the law of strain hardening $\theta = d\sigma/d\varepsilon = \theta(\varepsilon)$. According to this, each stage of plastic flow corresponds to a definite pattern of strain localization. A change in the law of strain hardening leads to the appearance of a new form of localized straining. The above findings indicate that the development of plastic flow is accompanied by a spontaneous localization of straining, the form of which is closely related to the law of plastic flow operative in the corresponding stage of strain hardening. The observed forms of strain localization spontaneously appear in the course of tension at a constant rate, that is, result from self-organization of the plastic flow process [4].

A very interesting pattern of strain localization is observed in the stage of linear strain hardening, where θ = const. In this case, the spatiotemporal pattern of inhomogeneous plastic flow acquires the form of an autowave propagating along the sample characterized by the velocity V_{aw} and by the wavelength λ. These values were previously measured in the experiments performed on single crystals of γ-Fe [5–7], single crystals of Cu and Ni [8], and polycrystalline samples of Al [9] and Zr [10]. The results of these experiments showed that the wave propagation velocity in the linear hardening stage is inversely proportional to the coefficient of strain hardening,

$$V_{aw} = \frac{G}{\theta}, \qquad (1)$$

with the proportionality factor $G = 6.3 \times 10^{-7}$ m/s.

The aforementioned materials do not include metals or alloys with body-centered cubic (bcc) crystal lattices. For this reason, the main attention in this study was concentrated on the laws of wave processes accompanying the plastic flow in a bcc Fe–3% Si alloy in single crystal and polycrystalline states.

The samples were tensile tested in an Instron 1185 machine at 300 K and a constant straining rate of $\dot{\varepsilon} = 1.2 \times 10^{-4}$ s^{-1}. The strain localization was analyzed by methods described in [11, 12]. According to this, the field of displacement vectors $\mathbf{r}(x, y)$ on the front surface of a sample was monitored by the method of two-exposure speckle interferometry [11] with a 15-s step (0.2% of the overall strain) beginning with a yield point and up to the sample breakage. Then, the distributions of longitudinal, transverse, shear, and rotation components of the plastic distortion tensor β_{ij} at all points of the sample surface were determined by numerical differentiation with respect to coordinates. Finally, the local strain distributions over the whole sample or along the axial line were constructed for various moments of time or various levels of deformation. The most convenient component of the β_{ij} tensor was the local elongation in the direction of tension (x axis), $\varepsilon_{xx} = du/dx$, where u is the $\mathbf{r}$ vector component along the x axis. By constructing and analyzing the spatial $\varepsilon(x, y)$ and spatiotemporal $\varepsilon_{xx}(x, t)$ patterns, it is possible to determine positions of the strain localization zones, trace their evolution with time, and compare this behavior to the sequence of stages in the plastic flow curve $\sigma(\varepsilon)$.

In both single crystal and polycrystalline samples of the Fe–3% Si alloy studied, the plastic flow was localized in certain active zones (plastic strain foci) occupying regular positions along the sample, while virtually no straining was developed in the regions between such foci. In the stage of linear strain hardening, the active zones move along the axis of the sample. By monitor-

1063-7850/04/3004-0338$26.00 © 2004 MAIK "Nauka/Interperiodica"

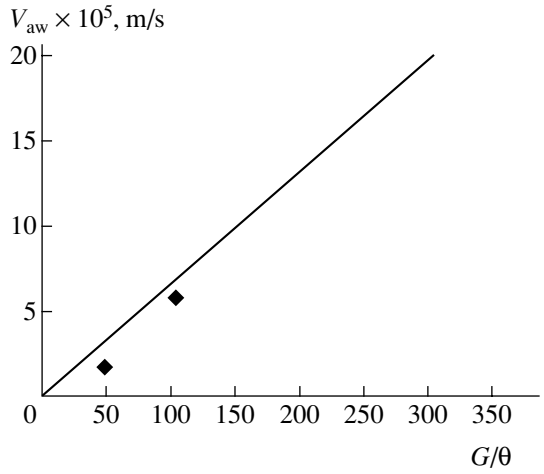

Fig. 1. The general relationship (1) between the autowave velocity and strain hardening coefficient in the stage of linear strain hardening [5–8] and the experimental points for single crystal and polycrystalline samples of a bcc alloy Fe–3% Si.

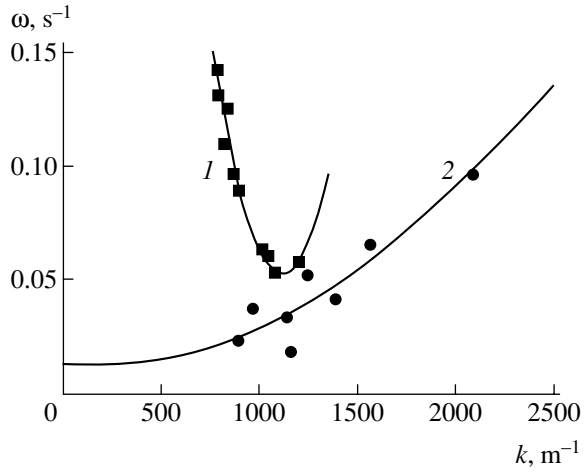

Fig. 2. Experimental points and generalized dispersion relations for strain localization waves in the stage of linear strain hardening (*1*) polycrystalline Al; (*2*) Fe–18% Cr–13% Ni single crystals (containing 0.35 and 0.5% N), Fe–13% Mn (containing 0.93 and 1.03% C), and Fe–3% Si.

ing the spatial positions X of the local peaks of ε_{xx} on the axis of tension at various times t, the autowave propagation velocity V_{aw} can be determined as the slope of the $X(t)$ plot [6, 8].

It was found that the experimental points for booth single crystal and polycrystalline bcc Fe–3% Si samples fall rather close to the general relation $V_{aw}(\theta)$, as shown in Fig. 1. This provides additional evidence for the validity of Eq. (1). The possible origin of the $V_{aw} \sim \theta^{-1}$ relation in the stage of linear strain hardening was described in [6, 8]. Considering the nature of wave processes involved in the plastic straining of solids, it is natural to compare this behavior to the thoroughly studied phenomenon of plasticity waves [13]. However, the shape of the $V_{aw}(\theta)$ relation is indicative of the basic difference between the two wave processes, since the plastic wave velocity behaves as $V_{pw} \approx \sqrt{\theta/\rho_0} \sim \theta^{1/2}$, where ρ_0 is the material density [13]. The difference between the laws $V_{aw} \sim \theta^{-1}$ and $V_{pw} \sim \theta^{1/2}$ suggests that our experiments have revealed a new type of wave processes involved in the plastic straining, which are referred to as the plastic strain localization waves.

The experimental method used for determining the velocity of motion of the plastic strain foci allows both the wavelength λ (or the wavenumber $k = 2\pi/\lambda$) and the time period T (or the frequency $\omega = 2\pi/T$) of the wave process to be simultaneously determined [6]. For the materials under consideration, a dispersion relation between the wavenumber k and the circular frequency ω (see Fig. 2) has the following form,

$$\omega = ak^2 + bk + c, \qquad (2)$$

where a, b, and c are constants characteristic of the particular groups of materials (see table). Relation (2) describes the dispersion law for the wave process accompanying localized plastic flow in the stage of linear strain hardening, which can be reduced to the canonical form $\omega = 1 + k^2$ [14]. The quadratic form of relation (2) is characteristic of the so-called nonlinear Schrödinger equation [15] frequently used for the description of self-organization processes in nonlinear systems.

The above laws allow the observed spatiotemporal regularities of inhomogeneous plastic flow to be identified neither with elastic waves nor with plasticity waves. Therefore, it is most probable that the observed behavior is related to the autowave phenomena in the form of self-organization or self-ordering spontaneously arising in a deformed medium [16].

Description of the spontaneous generation of structures (including deformation structures) in open systems featuring propagation of an energy flow is among the central problems in modern physics. The localization of plastic straining can be (and has to be) considered as an autowave process of the new type spontaneously arising in a strained medium featuring an energy flow. The laws of self-organization processes of such type have been studied in physical, chemical, and biological systems. A comparison shows that the auto-

Parameters of the dispersion relation (2) for the bcc materials studied

Metal/alloy	Lattice type	a, m^2/s	b, m/s	c, s^{-1}
Polycrystalline Al (Fig. 2, curve *1*)	fcc	7.9×10^{-7}	-1.7×10^{-3}	1.05
Fe-based alloys (Fig. 2, curve *2*)	bcc/fcc	2.2×10^{-8}	-5.6×10^{-6}	0.01

waves of localized straining are generally analogous to the dissipative structures—the basic concept of synergetics introduced by Nicolis and Prigogine [4].

In the course of continuous stretching of a sample at a constant rate, several types of such wave processes can take place one after another, with a unique relation between the character of a wave pattern and the law of strain hardening operative in each particular stage of this process. The change in the macroscopic patterns of plastic strain localization can be considered as a result of transformation of the autowave pattern. This transformation is based on processes occurring on a lower-scale (dislocation) structural level of a strained material.

REFERENCES

1. J. J. Gilman, Mech. Mater. **17**, 83 (1994).
2. L. B. Zuev, Ann. Phys. **10**, 965 (2001).
3. L. B. Zuev, V. I. Danilov, and B. S. Semukhin, Usp. Fiz. Met. **3**, 237 (2002).
4. G. Nicolis and I. Prigogine, *Exploring Complexity* (Freeman, New York, 1989; Mir, Moscow, 1990).
5. S. A. Barannikova, Zh. Tekh. Fiz. **70** (10), 138 (2000) [Tech. Phys. **45**, 1368 (2000)].
6. L. B. Zuev, S. A. Barannikova, N. V. Zarikovskaya, and I. Yu. Zykov, Fiz. Tverd. Tela (St. Petersburg) **43**, 1423 (2001) [Phys. Solid State **43**, 1483 (2001)].
7. L. B. Zuev, V. I. Danilov, and S. A. Barannikova, Int. J. Plast. **17**, 47 (2001).
8. V. I. Danilov, S. A. Barannikova, K. V. Gonchikov, and L. B. Zuev, Kristallografiya **47**, 730 (2002) [Crystallogr. Rep. **47**, 672 (2002)].
9. L. B. Zuev, B. S. Semukhin, and N. V. Zarikovskaya, Zh. Tekh. Fiz. **71** (5), 57 (2001) [Tech. Phys. **46**, 563 (2001)].
10. V. I. Danilov, S. Yu. Zavodchikov, S. A. Barannikova, *et al.*, Pis'ma Zh. Tekh. Fiz. **24** (1), 26 (1998) [Tech. Phys. Lett. **24**, 12 (1998)].
11. R. Jones and C. M. Wykes, *Holographic and Speckle Interferometry* (Cambridge Univ. Press, Cambridge, 1983; Mir, Moscow, 1986).
12. L. B. Zuev, S. N. Polyakov, and V. V. Gorbatenko, Proc. SPIE **4900**, 1197 (2002).
13. H. Kolsky, *Stress Waves in Solids* (Pergamon, Oxford, 1953; Inostrannaya Literatura, Moscow, 1955).
14. A. M. Kosevich and A. S. Kovalev, *Introduction in Nonlinear Physical Mechanics* (Naukova Dumka, Kiev, 1989).
15. R. K. Dodd, J. C. Eilbeck, J. Gibbon, and H. C. Morris, *Solitons and Nonlinear Wave Equations* (Academic Press, New York, 1982; Mir, Moscow, 1988).
16. V. A. Vasil'ev, Yu. M. Romanovskiĭ, and V. G. Yakhno, *Autowave Processes* (Nauka, Moscow, 1987).

Translated by P. Pozdeev

Technical Physics Letters, Vol. 30, No. 4, 2004, pp. 341–344. Translated from Pis'ma v Zhurnal Tekhnicheskoĭ Fiziki, Vol. 30, No. 8, 2004, pp. 81–87.

Maxwell–Wagner Relaxation in Magnetoelectric Composites

V. M. Petrov[a,*], M. I. Bichurin[a], and G. Srinivasan[b]

[a] *Novgorod State University, Novgorod, Russia*

[b] *Physics Department, Oakland University, Rochester, Michigan 48309, USA*

* *e-mail: deptptr@novsu.ac.ru*

Received October 27, 2003

Abstract—Giant Maxwell–Wagner relaxation of the magnetoelectric susceptibility and the magnetoelectric voltage coefficient was observed in a ferrite–piezoelectric composite. The relaxation frequency of the magnetoelectric susceptibility of this material can be controlled within broad limits by varying the volume fractions of the components and by modifying their properties. The maximum value of the magnetoelectric susceptibility of the composite studied exceeds the values known in other materials. © *2004 MAIK "Nauka/Interperiodica".*

Ferrite–piezoelectric composites are capable of exhibiting properties that are absent in the initial components—in particular, the magnetoelectric (ME) effect caused by the interaction of magnetic and electric subsystems via elastic deformations [1, 2]. When such a material is exposed to a magnetic field, magnetostriction of the magnetic phase gives rise to the induced polarization via piezoelectric effect in the electric subsystem, while exposure to an external electric field leads to induced magnetization. The accumulation of free charges at the interfaces between components gives rise to dielectric dispersion and losses in alternating electric fields, which is known as Maxwell–Wagner relaxation. Recently, Rodchenko and Turik [3] considered the dielectric and piezoelectric relaxations in layered composites of the ferroelectric–polymer type, while relaxation of the elastic constants in layered polar dielectrics was analyzed in [4].

This paper is devoted to the Maxwell–Wagner relaxation of parameters of the ME effects in ferrite–piezoelectric composites. We will consider this relaxation process in a multilayer composite of connectivity type 2–2 [5] comprising magnetostrictive and piezoelectric components.

Deformation, electric polarization, and magnetic induction in the magnetostrictive and piezoelectric phases can be described by the following system of equations,

$$\begin{aligned}
{}^pS_i &= {}^ps_{ij}{}^pT_j + {}^pd_{ki}{}^pE_k,\\
{}^mS_i &= {}^ms_{ij}{}^mT_j + {}^mq_{ki}{}^mH_k,\\
{}^pD_k &= {}^pd_{ki}{}^pT_i + {}^p\varepsilon_{kn}{}^pE_n,\\
{}^mD_k &= {}^m\varepsilon_{kn}{}^mE_n,\\
{}^pB_k &= {}^p\mu_{kn}{}^pH_n,\\
{}^mB_k &= {}^mq_{ki}{}^mT_i + {}^m\mu_{kn}{}^mH_n,
\end{aligned} \tag{1}$$

where ${}^pS_i$, ${}^pT_j$, ${}^pE_k$, ${}^pD_k$, ${}^pH_k$, ${}^pB_k$ and ${}^mS_i$, ${}^mT_j$, ${}^mE_k$, ${}^mD_k$, ${}^pH_k$, ${}^mB_k$ are the components of strain, stress, electric field, electric induction, magnetic field, and magnetic induction in the piezoelectric and magnetostrictive phases, respectively; ${}^ps_{ij}$, ${}^pd_{ki}$, ${}^p\varepsilon_{kn}$, ${}^p\mu_{kn}$ are the compliance coefficients, piezoelectric moduli, dielectric permittivities, and magnetic permeabilities of the piezoelectric phase; and ${}^ms_{ij}$, ${}^mq_{ki}$, ${}^m\varepsilon_{kn}$, ${}^m\mu_{kn}$ are the compliance coefficients, piezomagnetic moduli, dielectric permittivities, and magnetic permeabilities of the magnetostrictive phase. Taking into account the finite electric conductivity of both components, ${}^p\varepsilon_{33} = {}^p\varepsilon - i{}^p\gamma/\omega$ and ${}^m\varepsilon_{33} = {}^m\varepsilon - i{}^m\gamma/\omega$, where ${}^p\gamma$ and ${}^m\gamma$ are the conductivities of piezoelectric and magnetostrictive phases, respectively, and ω is a circular frequency of the electric field, which is much smaller than the electromechanical resonance frequency.

General formulas for determining the effective parameters of a composite can be obtained by averaging expressions for the components of strain and the electric and magnetic induction. In the absence of applied mechanical stresses, we obtain

$$\begin{aligned}
S_i &= d_{ki}E_k + q_{ki}H_k,\\
D_k &= \varepsilon_{kn}E_n + \alpha_{kn}H_n,\\
B_k &= \mu_{kn}H_n + \alpha_{kn}E_n,
\end{aligned} \tag{2}$$

where $E_n = v{}^pE_n + (1 - v){}^mE_n$, $H_n = v{}^pH_n + (1 - v){}^mH_n$, $S_i = v{}^pS_i + (1 - v){}^mS_i$, $D_k = v{}^pD_k + (1 - v){}^mD_k$, $B_k =$

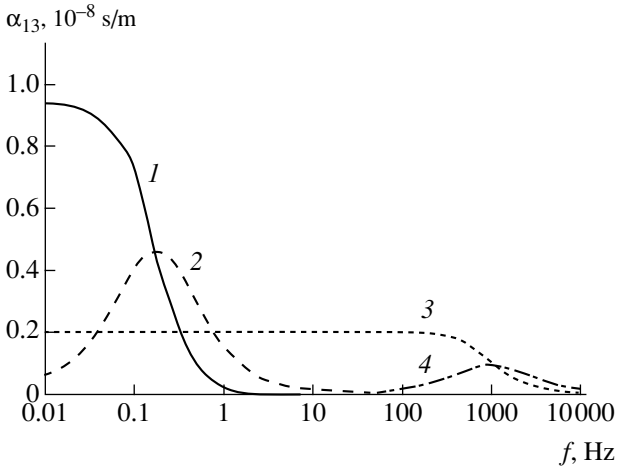

Fig. 1. The frequency dependence of the (*1*, *3*) real and (*2*, *4*) imaginary parts of the ME susceptibility of the NFO–PZT composites with $v = 0.001$ (*1*, *2*) and 0.9 (*3*, *4*).

$v\,{}^{p}B_k + (1 - v)\,{}^{m}B_k$; v is the volume fraction of the piezoelectric component; d_{ki} and q_{ki} are the effective piezoelectric and piezomagnetic moduli, respectively; ε_{kn} and μ_{kn} are the effective dielectric permittivities and magnetic permeabilities, respectively; and α_{kn} is the ME susceptibility of the composite.

We assume that the composite consists of thin piezoelectric and magnetostrictive layers parallel to the OX_1X_2 plane. The piezoelectric phase is polarized along the OX_3 axis, which is parallel to the direction of the alternating electric field with the circular frequency ω. The biasing and alternating magnetic fields are oriented along the OX_1 axis. The boundary conditions are as follows [2]:

$$\begin{gathered} {}^{p}D_3 = {}^{m}D_3, \quad {}^{p}B_3 = {}^{m}B_3, \quad {}^{p}S_1 = {}^{m}S_1, \quad {}^{p}S_2 = {}^{m}S_2, \\ v\,{}^{p}T_1 = (1 - v)\,{}^{m}T_1, \quad v\,{}^{p}T_2 = (1 - v)\,{}^{m}T_2. \end{gathered} \tag{3}$$

The general character of the frequency dependence of the ME susceptibility is determined by the Debye formulas

$$\begin{gathered} \alpha_{13} = \alpha'_{13} - i\alpha''_{13}, \\ \alpha'_{13} = \alpha_{13\infty} + \Delta\alpha_{13}/(1 + \omega^2\tau_\alpha^2); \\ \alpha''_{13} = \Delta\alpha_{13}\omega\tau_\alpha/(1 + \omega^2\tau_\alpha^2), \end{gathered} \tag{4}$$

where $\Delta\alpha_{13} = \alpha_{130} - \alpha_{13\infty}$ is the relaxation strength; α_{130} and $\alpha_{13\infty}$ are the static (for $\omega\tau_\alpha \ll 1$) and high-frequency (for $\omega\tau_\alpha \gg 1$) ME susceptibilities, respectively; and τ_α is the relaxation time.

The static and high-frequency ME susceptibilities and the relaxation time can be determined by solving Eqs. (1) and (2) with the boundary conditions (3). Assuming that the piezoelectric phase possesses the symmetry ∞m, while the magnetostrictive phase possesses a cubic symmetry, we obtain the following final expressions:

$$\begin{gathered} \alpha_{130} = -\frac{{}^{m}\gamma\, v(1 - v)({}^{m}q_{12} + {}^{m}q_{11})\,{}^{p}d_{31}}{\{[{}^{p}\gamma(1 - v) + {}^{m}\gamma\, v][({}^{m}s_{12} + {}^{m}s_{11})v + ({}^{p}s_{12} + {}^{p}s_{11})(1 - v)]\}}, \\ \alpha_{13\infty} = -\frac{{}^{m}\varepsilon\, v\,{}^{p}d_{31}(1 - v)({}^{m}q_{12} + {}^{m}q_{11})}{[v\,{}^{m}\varepsilon + {}^{p}\varepsilon(1 - v)][({}^{m}s_{12} + {}^{m}s_{11})v + ({}^{p}s_{12} + {}^{p}s_{11})(1 - v)] - 2\,{}^{p}d_{31}^2(1 - v)^2}, \\ \tau_\alpha = \frac{{}^{m}\varepsilon\, v + {}^{p}\varepsilon(1 - v)}{{}^{m}\gamma\, v + {}^{p}\gamma(1 - v)} - \frac{2(1 - v)^2\,{}^{p}d_{31}^2}{[v({}^{m}s_{12} + {}^{m}s_{11}) + ({}^{p}s_{12} + {}^{p}s_{11})(1 - v)][{}^{m}\gamma\, v + {}^{p}\gamma(1 - v)]}. \end{gathered} \tag{5}$$

For example, let us consider a composite consisting of polarized ferroelectric ceramic based on lead zirconate titanate (PZT) and a nickel ferrospinel (NFO). The values of parameters of the material components are as follows: ${}^{p}s_{11} = 15.3 \times 10^{-12}$ m^2/N, ${}^{p}s_{12} = -5 \times 10^{-12}$ m^2/N, ${}^{p}s_{13} = -7.22 \times 10^{-12}$ m^2/N, ${}^{p}s_{33} = 17.3 \times 10^{-12}$ m^2/N, ${}^{m}s_{11} = 15.3 \times 10^{-12}$ m^2/N, ${}^{m}s_{12} = -5 \times 10^{-12}$ m^2/N, ${}^{m}q_{33} = -1880 \times 10^{-12}$ m/A, ${}^{m}q_{31} = 556 \times 10^{-12}$ m/A, ${}^{p}d_{31} = -175 \times 10^{-12}$ m/V, ${}^{p}d_{33} = -400 \times 10^{-12}$ m/V, ${}^{m}\mu_{33}/\mu_0 = 3$, ${}^{p}\varepsilon/\varepsilon_0 = 1750$, ${}^{m}\varepsilon/\varepsilon_0 = 10$, ${}^{m}\gamma = 10^{-5}$ $(\Omega\ \text{m})^{-1}$, and ${}^{p}\gamma = 10^{-13}$ $(\Omega\ \text{m})^{-1}$.

Figure 1 illustrates the giant relaxation of the ME susceptibility. The large relaxation depth is typical of a composite with the piezoelectric component characterized by a high permittivity and the magnetostrictive component possessing a high conductivity. In the case of ${}^{m}\varepsilon/{}^{p}\varepsilon \ll 1$ and ${}^{p}\gamma/{}^{m}\gamma \ll 1$, the maximum relaxation depth is observed for a volume fraction of the piezoelectric phase $v_1 \approx [({}^{p}s_{11} + {}^{p}s_{12})/({}^{m}s_{11} + {}^{m}s_{12})]^{1/2}({}^{p}\gamma/{}^{m}\gamma)^{1/2}$. Assuming that the components possess equal compliances, we obtain $v_1 \approx ({}^{p}\gamma/{}^{m}\gamma)^{1/2}$. For ${}^{p}\gamma/{}^{m}\gamma \ll v \ll 1$, the static ME susceptibility approaches the maximum pos-

sible value equal to $({}^{m}q_{12} + {}^{m}q_{11}){}^{p}d_{31}/({}^{p}s_{11} + {}^{p}s_{12})$. For a composite with the given volume fraction $v_1 = ({}^{p}h/{}^{m}h)^{1/2} \approx 10^{-4}$ (where ${}^{p}h$ and ${}^{m}h$ are the thicknesses of the piezoelectric and ferrite components) and the limiting ME susceptibility is 0.94×10^{-8} s/m. The large value of the static ME susceptibility is related to the high electric field strength in the piezoelectric component at a small thickness of PZT layers, to the considerable conductivity of the ferrite layer, and to high internal mechanical stresses ${}^{p}T_j$ and ${}^{m}T_j$ ($j = 1, 2$). These stresses are induced by the electric field in the piezoelectric component. The maximum ME susceptibility for the composite under consideration exceeds the values known for other materials (for example, the ME susceptibility of chromium oxide is 1.1×10^{-11} s/m).

In the case of a weak piezoelectric effect $({}^{p}d_{31}^2/[({}^{p}s_{11} + {}^{p}s_{12}){}^{p}\varepsilon] \ll 1)$, the relaxation time according to (5) for ${}^{p}\gamma/{}^{m}\gamma \ll v/(1 - v)$ is determined primarily by the time required for charging the capacitance of the piezoelectric layer via the resistance of the ferrite layer: $\tau_\alpha \approx ({}^{p}\varepsilon/{}^{m}\gamma)(1 - v)/v$. As the volume fraction of the piezoelectric phase increases, the relaxation time rapidly decreases. An increase in the piezoelectric effect gives rise to the second term in the expression for τ in Eqs. (5) describing the contribution of the piezoelectric component. The mechanical stresses ${}^{p}T_1$ and ${}^{p}T_2$ lead to the appearance of an additional charge on the capacitance of the PZT layer due to the transverse piezoelectric effect. This results in a decrease in the time required for charging this capacitance and, hence, in the ME susceptibility relaxation time. According to formulas (5), the relaxation time and the relaxation frequency $\omega_r = 1/\tau_\alpha$ corresponding to the maximum value of the imaginary part of the ME susceptibility can be controlled within broad limits by varying the volume fractions of the material components and by modifying their properties.

The frequency dependence of the ME voltage coefficient $\alpha_{E,T} = E_3/H_1$ is determined by the Debye formulas analogous to expressions (4),

$$\begin{aligned} \alpha_{E,T} &= \alpha'_{E,T} - i\alpha''_{E,T}, \\ \alpha'_{E,T} &= \alpha_{E,T\infty} + \Delta\alpha_{E,T}/(1 + \omega^2\tau_{\alpha T}^2); \\ \alpha''_{E,T} &= \Delta\alpha_{E,T}\omega\tau_{\alpha T}/(1 + \omega^2\tau_{\alpha T}^2), \end{aligned} \qquad (6)$$

where

$$\Delta\varepsilon_{E,T} = \alpha_{E,T\infty} = \frac{v\,{}^{p}d_{31}(1 - v)({}^{m}q_{12} + {}^{m}q_{11})}{[({}^{m}s_{12} + {}^{m}s_{11})v + ({}^{p}s_{12} + {}^{p}s_{11})(1 - v)] - 2\,{}^{p}d_{31}^2(1 - v)},$$

$$\tau_{aT} = \frac{{}^{p}\varepsilon}{{}^{p}\gamma} - \frac{2(1 - v)\,{}^{p}d_{31}^2}{{}^{p}\gamma[v({}^{m}s_{12} + {}^{m}s_{11}) + ({}^{p}s_{12} + {}^{p}s_{11})(1 - v)]}.$$

In contrast to the case of ME susceptibility, the real part of the ME voltage coefficient increases with the frequency, which corresponds to the inverse relaxation (Fig. 2). The relaxation depth is maximum for $v \approx 0.5$. In the case of a weak piezoelectric effect $(d_{31}^2/[({}^{p}s_{11} + {}^{p}s_{11} + {}^{p}s_{12}){}^{p}\varepsilon] \ll 1)$, the relaxation time is determined primarily by the time required for discharge of the capacitance of the piezoelectric layer via its own resistance, $\tau_{\alpha T} \approx {}^{p}\varepsilon/{}^{p}\gamma$ ($\tau_{\alpha T} \gg \tau_\alpha$), and is independent of the volume fraction of components. As the piezoelectric effect grows, the relaxation time according to (6) drops. This is favored by a decrease in charging of the capacitance of the piezoelectric layer under the action of mechanical stresses ${}^{p}T_1$ and ${}^{p}T_2$ arising due to the applied magnetic field. As the conductivity of the piezoelectric layer increases to 10^{-5} $(\Omega\ \mathrm{m})^{-1}$, the relaxation frequency grows up to 100 Hz.

Thus, the layered ferrite–piezoelectric composite exhibits giant relaxation of the ME susceptibility and the ME voltage coefficient, which is normal in the former case and inverse in the latter case. The relaxation time and the relaxation frequency of the ME susceptibility can be controlled within broad limits by varying the volume fractions of the material components and by modifying their properties. The maximum value of the magnetoelectric susceptibility of the composite studied exceeds the values known in other materials. The obtained results can be used for selecting the working frequency range in which the ME susceptibility and the ME voltage coefficient reach maximum values.

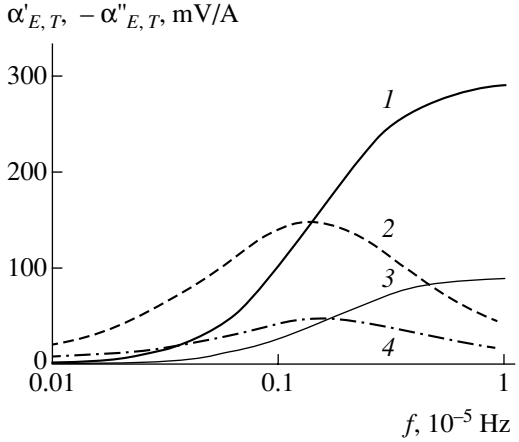

Fig. 2. The frequency dependence of the (*1*, *3*) real and (*2*, *4*) imaginary parts of the ME voltage coefficient of the NFO–PZT composites with $v = 0.1$ (*1*, *2*) and 0.5 (*3*, *4*).

Acknowledgments. This study was supported in part by the Ministry of Education of the Russian Federation (project no. E02-3.4-278), the "Universities of Russia" Program (project no. UR 01.01.007), and the US National Science Foundation (grant DMR-0322254).

REFERENCES

1. M. I. Bichurin, V. M. Petrov, and G. Srinivasan, J. Appl. Phys. **92**, 7681 (2002).
2. M. I. Bichurin, V. M. Petrov, and G. Srinivasan, Phys. Rev. B **68**, 054402 (2003).
3. G. S. Radchenko and A. V. Turik, Fiz. Tverd. Tela (St. Petersburg) **45**, 1676 (2003) [Phys. Solid State **45**, 1759 (2003)].
4. G. S. Radchenko and A. V. Turik, Fiz. Tverd. Tela (St. Petersburg) **45**, 1013 (2003) [Phys. Solid State **45**, 1060 (2003)].
5. R. E. Newnham, D. P. Skinner, and L. E. Cross, Mater. Res. Bull. **13**, 525 (1978).

Translated by P. Pozdeev

Technical Physics Letters, Vol. 30, No. 4, 2004, pp. 345–347. Translated from Pis'ma v Zhurnal Tekhnicheskoĭ Fiziki, Vol. 30, No. 8, 2004, pp. 88–94.

The Formation and Characterization of Freon 22 Cluster Beams

V. N. Lokhman, E. A. Ryabov*, and D. D. Ogurok

Institute of Spectroscopy, Russian Academy of Sciences, Troitsk, Moscow oblast, Russia

** e-mail: ryabov@isan.troitsk.ru*

Received September 26, 2003

Abstract—Freon 22 (CF_2HCl) clusters have been found upon gasdynamic cooling of these molecules in a pulsed supersonic beam. A method for diagnostics of the cluster beams of freon 22 has been developed based on the phenomenon of UV multiphoton ionization in combination with the time-of-flight mass spectrometry and the IR photodissociation of clusters. The velocities of directed motion and the longitudinal and transverse velocity components of the thermal motion of $(CF_2HCl)_n$ clusters in a beam of freon 22 were measured for various stagnation pressures P_0. The degree of beam clusterization was estimated. © *2004 MAIK "Nauka/Interperiodica".*

The method of carbon isotope separation ($^{13}C/^{12}C$) based on the IR multiphoton dissociation of freon 22 (chlorodifluoromethane, CF_2HCl) under the action of a CO_2 laser has been implemented in practice [1]. Investigations aimed at increasing the efficiency and selectivity of the laser isotope separation technology are continued. One possible way to higher selectivity is via narrowing of the IR absorption spectra of molecules upon their gasdynamic cooling in a pulsed supersonic beam [2–5]. However, deep cooling may give rise to clusterization accompanied by a significant change in parameters of the molecular beam [6], which results in the loss of isotopic selectivity of the laser isotope separation process.

In connection with this, it is important to develop methods for determining the parameters of supersonic beams of freon 22 molecules and studying their characteristics under the conditions of possible clusterization. This paper presents one of the possible methods employing photoionization time-of-flight (TOF) mass spectrometry.

The measurements were performed using a setup described in detail elsewhere [7]. The geometry of measurements is illustrated in Fig. 1a. A supersonic beam was generated by a pulsed electromagnetic nozzle PN (General Valve) with an orifice diameter of $d = 0.8$ mm and a pulse width (FWHM) $\Delta T = 200$ μs. The beam was passed via a skimmer with a diameter of $d_S = 0.66$ mm (situated at a distance of $\Delta Z_{NS} = 38.5$ mm from the nozzle output) and directed to the ionization chamber of the mass spectrometer. At a distance of $\Delta Z_{SD} = 96.5$ mm from the skimmer input cross section, the beam intersected with the mutually perpendicular axes of the mass spectrometer ($0Y$) and the beam of focused ($f = 12$ cm) pulsed (7 ns) UV laser radiation ($\lambda \approx 232$ nm) used for the photoionization. The vibrational excitation of molecules was produced by IR radiation of a pulsed (150 ns) CO_2 laser. By changing the delay between the nozzle triggering and the UV laser pulse, it was possible to measure the TOF spectrum $S(t, y = 0)$ of the molecular beam (i.e., the density of particles in the beam passing through the detection zone). By shifting the detection zone along the $0Y$ axis at a fixed delay time, it was possible to measure the particle density profile $S(y)$ in the transverse direction (across the beam).

The presence of clusters in the molecular beam was manifested by their dissociation under the action of IR radiation at an energy flux density much lower than the IR multiphoton dissociation (MPD) threshold for freon 22 (see below). In addition, the experiments showed that the main products of UV multiphonon ionization (MPI) are ions with the mass-to-charge ratios $M/e = 31$ (CF^+) and 51 (CF_2H^+). While the former signal $S(31)$ may contain contributions from both monomers and clusters, the latter signal $S(51)$ at $E_{UV} \approx 100$–270 μJ ($\Phi_{UV} \approx$ 10–27 J/cm^2) for $\lambda \approx 232$ nm is entirely due to the monomers. This fact allows the behavior of monomers and clusters in the beam to be traced separately.

The velocity U of directed motion of clusters in the beam was determined by measuring the delay between the time (t_D) of appearance of the front of a step perturbation "mark" in the detection zone Z_D and the moment (t_{IR}) of this perturbation induction at the skimmer input (Z_S): $U = \Delta Z_{SD}/(t_D - t_{IR})$ (Figs. 1b and 1c). The perturbation mark was produced by IR photodissociation of clusters under the action of CO_2 laser radiation in a stationary beam flow in the skimmer region. The IR radiation energy density ($\Phi_{IR} \approx 0.4$ J/cm^2) was much lower

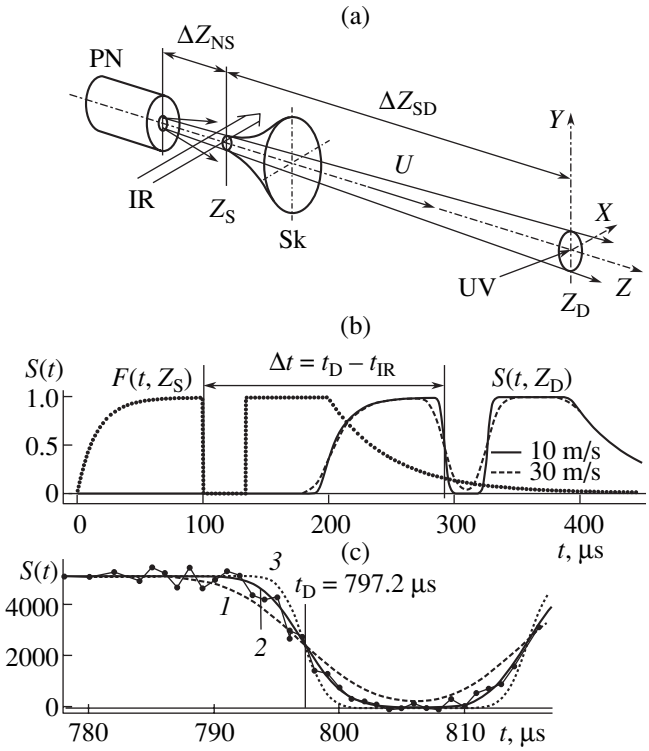

Fig. 1. (a) Schematic diagram of the experimental arrangement: PN, pulsed nozzle; Sk, skimmer; IR and UV, pulsed infrared and ultraviolet laser beams, respectively; 0*Y*, the axis of TOF mass spectrometer; (b) TOF spectrum simulation: $F(t, Z_S)$ source function at the skimmer input pulse-modulated at $t = t_{IR}$; $S(t, Z_D)$, TOF signals in the detection zone calculated for two values $V_{\parallel}$ = 10 and 30 m/s of the longitudinal thermal velocity component; (c) experimental TOF signal (black points) measured for P_0 = 245 kPa, E_{UV} = 340 μJ, λ_{UV} = 231.5 nm, Φ_{IR} = 0.4 J/cm^2, ν_{IR} = 1037.4 cm^{-1}, and t_{IR} = 604 μs (t_D = 797.2 μs corresponds to $U = 500 \pm 1.5$ m/s) in comparison to the results of model calculations for $V_{\parallel}$ = 17 (*1*), 9.8 (*2*), and 5.4 m/s (*3*).

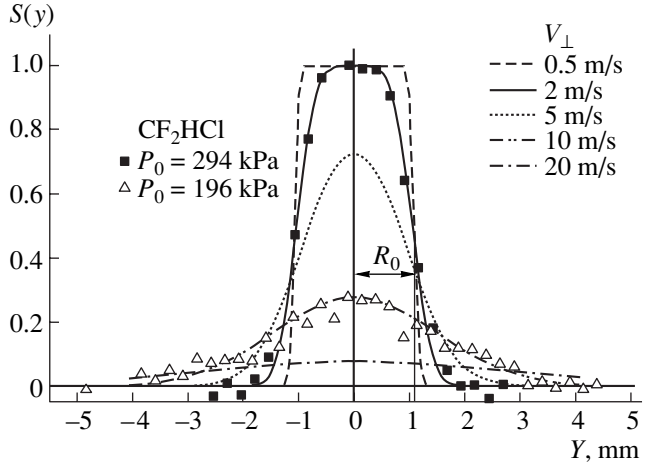

Fig. 2. Particle density profiles across the beam in the detection zone: experimental distributions of the cluster signal component intensity (in relative units) for two values of the stagnant pressure P_0 (symbols) and the results of model calculations for various values of the transverse thermal velocity components $V_\perp$ (curves).

than the threshold of dissociation of CF_2HCl molecules (≈3 J/cm^2) [5].

The longitudinal ($V_{\parallel}$) and transverse ($V_\perp$) components of the thermal velocity of clusters in a beam of freon 22 were determined by comparing experimental data to the results of numerical simulations: $V_{\parallel}$ was evaluated from smearing of the $S(t, y = 0)$ step along the 0*Z* axis (Fig. 1b) and $V_\perp$, from the shape of the beam density profiles $S(y)$ in the transverse direction (Fig. 2). The calculations were performed assuming that the distribution of particle drift velocities in front of the skimmer was described by an elliptical Maxwell distribution [6]. For description of the transverse profile, the beam was considered as expanding (with the radius R_0 in the detection zone determined from the experimental geometry) and additionally broadened by the transverse thermal motion (Fig. 2).

Figure 1c shows the experimental (P_0 = 245 kPa) and calculated TOF spectra of clusters. As can be seen, the experimental spectrum is described quite well by a model curve with $V_{\parallel}$ = 9.8 m/s. Figure 2 presents experimental transverse distributions of the cluster signal component measured for two values of the stagnation pressure, P_0 = 196 and 294 kPa, in comparison to the profiles calculated for various $V_\perp$ values. As can be seen, the experimental curves are well described by the model distributions with $V_\perp$ = 10 and 2 m/s, respectively.

The results of measurements performed for the beams obtained using various stagnation pressures are presented in the table. In addition to the values of cluster velocities (U, $V_{\parallel}V_\perp$), the table gives data on the gas consumption per pulse (ΔQ), the cluster signal intensity (S_C) and its ratio to the monomer signal intensity $(S_C/S_M)_D$ at the beam center (paraxial region) in the detection zone, and the fraction of condensed molecules at the skimmer input (the degree of clusterization) estimated as $k_S = (S_C/(S_C + S_M))_S$.

As can be seen from data in the table, the average drift velocity in a beam formed under the conditions of developed clusterization ($P_0 \geq 190$ kPa) falls within $U = 501 \pm 5$ m/s and rather weakly depends on the stagnation pressure varied in the interval of P_0 = 190–380 kPa. A weak dependence on P_0 is also observed for $V_{\parallel}$ (the average value being about 10 m/s). In contrast, the transverse velocity component $V_\perp$ of the thermal motion in this pressure interval exhibits a more than tenfold variation. The $V_\perp$ value determines the drop in the particle density at the beam center in the detection zone caused by the thermal transverse beam blurring (blurring factor). According to the results of calculations, the influence of this factor in the experimental geometry adopted becomes significant for $V_\perp > 2$ m/s and is negligibly small for lower transverse velocities. It is this factor that accounts for the rapid growth in the cluster signal component intensity S_C (see table) with

Table

P_0, kPa	ΔQ, Pa m^3	S_C, a.u.	U, m/s	$V_{\parallel}$, m/s	$V_{\perp}$, m/s	$(S_C/S_M)_D$	k_S
392	130.26×10^{-6}	9300				14.5	
343	114.66×10^{-6}	7300	505	10	≤1	13.8	0.22
294	99.99×10^{-6}	6000	506	10	2	10.7	
245	97.33×10^{-6}	3700	500	9.8	5.5	9.3	
196	85.33×10^{-6}	1500	497	14	10	4.4	
147	73.33×10^{-6}	550				2.0	

the pressure up to P_0 = 290 kPa (the latter corresponding to $V_{\perp C}$ = 2 m/s). At P_0 = 343 kPa, the clusters have $V_{\perp C} \approx 1$ m/s and the blurring factor is insignificant.

In contrast, monomers at the same pressure exhibit a broad transverse profile (not depicted in Fig. 2), from which their average transverse velocity can be estimated as $V_{\perp M} \geq 30$ m/s. With this transverse velocity component, the blurring of monomers results approximately in a 50-fold decrease in their density at the beam center in the detection zone. This factor accounts for the measured value of $(S_C/S_M)_D$. Taking this into account, it is possible to estimate the degree of beam clusterization at the skimmer input. For example, at P_0 = 343 kPa, the central part of the beam at the skimmer input contains 22% cluster molecules. Because of the difference between $V_{\perp C}$ and $V_{\perp M}$ (and, hence, between the corresponding blurring factors), these molecules provide for a 14-fold greater contribution than monomers in the detection zone. One of the factors responsible for the difference between $V_{\perp C}$ and $V_{\perp M}$ is the difference in masses of the monomers and clusters. Assuming that the transverse temperatures of both components in front of the skimmer are the same, we can roughly estimate the average number of molecules in a cluster as $n_C = (V_{\perp M}/V_{\perp C})^2$. As the stagnation pressure is varied in the range from 190 to 340 kPa, n_C changes approximately from 10 to 90.

Thus, using the proposed method based on the UV MPI and IR photodissociation in combination with TOF mass spectrometry, we revealed clusterization of a molecular beam of freon 22 and determined the main parameters of the cluster beam.

Acknowledgments. The authors are grateful to G.N. Makarov for fruitful discussions.

This study was supported by the Russian Foundation for Basic Research, project no. 03-02-17080.

REFERENCES

1. V. Yu. Baranov, A. P. Dyad'kin, D. D. Malyuta, *et al.*, Proc. SPIE **4165**, 314 (2000).
2. S. S. Alimpiev, G. S. Baronov, S. M. Karavaev, *et al.*, Kvantovaya Élektron. (Moscow) **10**, 376 (1983).
3. G. N. Makarov, D. E. Malinovskiĭ, and D. D. Ogurok, Zh. Tekh. Fiz. **69** (1), 35 (1999) [Tech. Phys. **44**, 31 (1999)].
4. G. N. Makarov, V. N. Lokhman, D. E. Malinovskiĭ, *et al.*, Khim. Fiz. **18** (3), 71 (1999).
5. V. N. Lokhman, D. D. Ogurok, and E. A. Ryabov, Chem. Phys. **271**, 357 (2001).
6. *Atomic and Molecular Beam Methods*, Ed. by G. Scoles (Oxford Univ. Press, New York, 1988), Vol. 1; *Atomic and Molecular Beam Methods*, Ed. by G. Scoles (Oxford Univ. Press, 1992), Vol. 2.
7. A. V. Dem'yanenko, V. N. Lokhman, D. D. Ogurok, *et al.*, Chem. Phys. Lett. **320**, 594 (2000).

Translated by P. Pozdeev